PACS: 61.43.Gt; 68.03.-g; 68.43.-h; 81.40.Ef *DOI:10.15407/Surface.2025.17.169*

INTERFACIAL PHENOMENA AFFECTED BY MORPHOLOGY AND TEXTURE OF CARBONS AND THEIR COMPOSITES

V. M. Gun'ko[1], V. V. Turov[1], L. S. Andriyko[1,2], I. A. Tagayev[2]

[1]Chuiko Institute of Surface Chemistry of the NAS of Ukraine,
17 Oleg Mudrak Street, 03164 Kyiv, Ukraine, e-mail: vlad_gunko@ukr.net
[2]Navoi Innovation University, 39 Tashkent Street, Navoi 210100, Uzbekistan,
e-mail: andriykolyuda@gmail.com

Carbon materials (CM) and their composites (CMC) are characterized by various particulate morphologies, textures, surface structures (e.g., oxidation/reduction degree), and other characteristics. Therefore, a search for regularities for numerous CM/CMC concerning interfacial phenomena, including sorption from different phases, could be a complex task. To elucidate essential aspects of the phenomena, various experimental (e.g., electron microscopy, sorption of probes, spectroscopy, X-ray diffraction, thermogravimetry, etc.) and theoretical (e.g., quantum chemistry) methods could be used with maximum detailed analyses using well-developed computation methods (such as simple and self-consistent regularization procedures). Dozens of CM/CMC have been analyzed here with respect to (i) particulate morphology, textural and surface characteristics; (ii) sorption of organic and inorganic compounds as solutes/eluates in different media; and (iii) confined space and cryoscopic effects for individual and mixed solvents vs. temperature (at $T < T_{freezing}$) and concentrations. The obtained results could be of interest from both theoretical and practical points of view because they show different aspects of the interfacial phenomena occurring in confined pore space of various carbons and composites characterized by different morphology, texture, and surface structure. This is important for optimization of the CM/CMC characteristics for effective use of them in practical applications.

Keywords: *3D-0D carbons; activated carbons; graphitized carbons; textural characteristics; sorption; solutions; interfacial phenomena; confined space effect; cryoscopic effect.*

INTRODUCTION

Various carbon materials (CM) and their composites (CMC) with metal, metal oxides, polymers, etc. are frequently used for purification of water [1–5] from metal ions [6–20], organics [21–34], toxins [35–41], *etc.* CM/CMC could possess various particulate morphologies, texture, surface chemistry, and other characteristics and properties that affect their application pathways and efficiency [42–48]. High variability, flexibility, and easy modification of the CM/CMC characteristics [1–5, 49–60], especially by attachment of various surface functionalities, provide wide use of CM/CMC for effective sorption of various organics (dyes, toxins, organic wastewater pollutants, *etc.*) and inorganics (metal ions, acids, bases, *etc.*). To improve or change the CM characteristics, different modifications (thermal treatment, oxidation, reduction, surface deposition, and functionalization) of CM, as well as preparation of various CMC, could be used [1–11, 61–64]. Not only activated carbons (AC) but also carbon nanotubes (CNT) [65–67], coal-based sorbents [34, 68], and 2D systems with graphene and graphene oxides [8] are used for water purification. Despite these aspects are well described in the literature, features and regularities in the interfacial phenomena upon sorption/desorption of various compounds on different CM/CMC located in different media (aqueous or non-aqueous) need additional investigations for a deeper

insight into confined space effects (CSE), colligative properties (CP) of mixtures and cryoscopic effects (CE) under CSE, temperature and interfacial behaviors of liquids and fluids bound to CM [69–72], competitive sorption, equilibrium and kinetic sorption, breakthrough dynamics, selectivity of sorption, *etc.* [1–8, 49–67].

There are several factors strongly affecting the interfacial phenomena at CM/CMC surfaces including sorption: (i) morphological, textural, and structural characteristics of sorbents; (ii) sorbate characteristics and contents; (iii) media (liquid, fluid, gaseous) characteristics (molecular weight, size, and shape, polarity of solvents); and (iv) conditions, *e.g.*, equilibrium (static) and non-equilibrium (dynamic) sorption, flow speed, temperature, pressure, *etc.* [1–6, 42–45, 67–80]. The particulate morphology (particle shape, size distribution, aggregation, particulate hierarchy), porosity (pore volume, length, shape, connectivity, size distribution, specific surface area), surface nature (oxidized or reduced CM, metal/metalloid oxides/CM, metals/CM, polymers/CM) and structure (polarity, charging, content and structure of surface functionalities) determine the interfacial and temperature behaviors of sorbates upon equilibrium or dynamic sorption. The characteristics of sorbates (molecular structure, weight, shape, polarity, charging) determine the sorption (interfacial) layer structure affected by confined space effects (CSE) strongly dependent on the pore sizes and temperature [67–80]. The dispersion media characteristics, such as polarity, molecular size, shape, and weight, boiling and freezing temperatures, affect the mentioned phenomena because the dispersion media molecules could compete against sorbate molecules for active surface sites, block entrances into narrow pores, displace sorbate molecules from surface and pores, *etc.* Additionally, these factors could differently affect the static (equilibrium) and dynamic (*e.g.*, breakthrough) sorption depending on the pore sizes. Thus, there are a lot of factors varied for each sorbent/sorbate pair under certain conditions, and some of them could play a more important role concerning, *e.g.*, sorption efficiency. The pore sizes could be one of the most important factors on the sorption because the behavior of solvents, co-solvents, sorbates, solutes, eluates, and media is very sensitive to the confined space effects [67–72]. For example, the solvent activity, molecular mobility, and diffusivity strongly decrease in nanopores (pore radius R or half-width $x < 1$ nm) and narrow mesopores (1 nm $< x <$ 3 nm) in comparison to those in macropores ($x > 25$ nm). The polarity and charging of molecules of sorbates and dispersion media strongly affect the intermolecular interactions due to increasing electrostatic components, as well as the colligative properties of mixtures, their temperature behavior and distribution in pores of different sizes, equilibration time, *etc.* [67–72]. Therefore, compounds well soluble in bulk solvents could be insoluble or poorly soluble in the same solvents confined in nanopores and the colligative properties of the mixtures strongly change there, and typically, cryoscopic effects decrease [69, 70]. CM/CMC sorbents, which are most effective ones than many others composed of natural and synthetic metal/metalloid oxides, polymers, *etc.*, could be divided into (i) 3D systems such as chars, activated carbons, carbon blacks, fullerite, and related composites (*e.g.*, with metal/metalloid oxides, polymers, metal nanoparticles); (ii) 2D (graphene-based reduced or oxidized); (iii) 1D (nanotubes, nanofibers); and (iv) 0D (fullerene) ones [1–11, 69–80]. CMC and other materials could have mixed complex particulate morphologies and pore topologies (due to the difference of CMC components) that could lead to more complex interfacial phenomena [67, 69, 70, 81].

From both practical and theoretical points of view, it is of interest to elucidate important regularities and features of the interfacial and temperature behaviors of solutes/solvents/eluates under various CSE at a pore surface of CM/CMC characterized by different particulate morphologies, textures, and surface structures. Several different situations could be considered concerning the interfacial phenomena, affected by CSE, including sorption of low- and high-molecular weight organics, inorganic co-solvents, extraction of trace amounts of solutes and their recovery, competitive sorption of solutes, solvents, and co-solvents upon interaction with different CM/CMC depending on concentrations and temperature.

MATERIALS AND METHODS

A set of CM (Tables 1–3) including activated carbons (AC) prepared using various natural and synthetic precursors, carbon blacks, cokes, graphitized carbons, multiwalled carbon nanotubes (MWCNT), fullerite, and graphene oxide, as well as some CMC with polymer/CM and metal/metalloid oxide/CM have been used to study features of the interfacial phenomena under different CSE.

Commercial activated carbon A2PS (HPSD, Hajnówka, Poland) prepared from plum stones (as well as some other AC) carbonized at 550–600°C, activated at 900-1000°C, and demineralized (deashed) with a mixture of HCl and methanol was utilized as the initial material with a granule fraction of 0.045–0.063 mm. A2PS was oxidized by H_2O_2 (A2PS–O4 and A2PS–O8) and reduced by H_2 (giving a lower amount of oxygen–containing surface functionalities removed by reaction with hydrogen, A2PS–H). To prepare oxidized AC, 5 g of A2PS in a quartz thimble was placed into an autoclave with 20 mL of 30% H_2O_2 and treated in the steam phase at 250°C (A2PS–O4) or 350°C (A2PS–O8) for 6 h. A reduced AC A2PS–H was prepared on heating of A2PS in a H_2 stream in a quartz flow reactor at 800°C for 8 h. Catalytic activation of A2PS was carried out using impregnation of AC by solution of 0.25% Ca(II) salt ($Ca(CH_3COO)_2 \cdot H_2O$) and subsequent activation at 800°C (label A2PSM). Then pyrocarbon was deposited onto A2PS and A2PSM by carbonization of methylene chloride and n–amyl alcohol (pentanol–1). Methylene chloride was pyrolyzed in a rotary reactor with a nitrogen flow at 450°C for 15 min (A2PS→A2PSC at the pyrocarbon amount C_C = 22 wt.%) and 30 min (A2PSM→A2PSMC at C_C = 40 wt.%). Additional pyrocarbon was deposited on A2PSC (A2PSCA) and A2PSMC (A2PSMCA) by pyrolysis of n–amyl alcohol (5 cm^3 per 1.5 g of a carbon sorbent) in an autoclave at 450 °C for 6 h. Samples cooled to room temperature were washed with dimethylformamide (DMFA) then with acetone and finally were dried at 150°C. A2PSCA and A2PSMCA contained 11 and 21 wt.% of pyrocarbon deposits, respectively; *i.e.*, total C_C was 33 wt.% (A2PSCA) and 61 wt.% (A2PSMCA) (some details see in [67, 82–88]).

Coke (granules of irregular shapes and 0.20–0.32 mm in size) (WDDW, Hajnówka, Poland) of natural origin, washed with HCl and methanol, was used as the initial material. The first coke series was prepared by water steam gasification for 2, 3, 6, and 8 h (burn–off was 9, 14, 32, and 38% respectively) and labeled Coke–2h, 3h, 6h, and 8h. The second series with deposited Ca(II) (3%) on the initial coke was activated by water vapor for 1, 4, and 8 h (burn off was 53, 63, and 74% respectively) labeled Coke–1h/Ca, 4h/Ca, and 8h/Ca. The third coke series was prepared by modification of the latter samples by pyrocarbon (pyrolysis of CH_2Cl_2 for 15 min) at C_C = 16, 17, and 29 wt.% (labeled Coke–1h/Ca/C, 4h/Ca/C, and 8h/Ca/C).

Commercial sorbents, such as porous graphitized carbons Hypercarb (ThermoHypersil, UK, particle diameter of 0.03–0.04 mm), Envicarb (Supelco, USA, particles of 0.04–0.06 mm), and Carboprep (Restek, USA), as well as polymeric LiChrolut EN (Merck), were used in comparison investigations.

AC W was prepared from sawdust using phosphoric acid activation at ca. 800°C, and then it was oxidized with ammonium persulfate (AC WO).

Commercial resins Zerolite 225×8, Wofatite, and Dowex (used in ion–exchange process) were utilized as precursors carbonized using a fluid–bed quartz reactor with N_2 + H_2 (1 : 1) flow at 800°C. Then three chairs were activated in the fluid–bed quartz reactor at 800ºC for 1 h. Chars prepared from Zerolite and Wofatite resins were oxidized by 30% of the H_2O_2 solution before the next activation. Then chars were impregnated by a solution of $Ca(CH_3COO)_2 \cdot H_2O$ (POCh Gliwice, Poland) at a Ca(II) concentration of 1 wt.%. Then carbons were eluted with 6% solution of HCl and washed with distilled water. Thus, carbon ACR1 (with Zerolite resin as a precursor) was prepared using carbonization, oxidation, impregnation, and activation. Samples ACR2 (Wofatite resin) were prepared by using the same technique. Sample ACR3 (Dowex resin) was

prepared using carbonization and activation processes. The burn–off of ACR1, ACR2, and ACR3 carbons was 50, 40, and 20 wt.%, respectively. Sample ACR4 was prepared by graphitization of ACR3 in an argon atmosphere at 2400°C for 3 h.

Preparation of granular bentonite–carbon samples was with grinding of initial bentonite and brown coal (1 : 2 w/w), sifting them through a sieve with a slot size of 1 mm in diameter, granulating, and drying. Sulfuric acid was used for activation in a muffle furnace without oxygen at 950°C for 45 min. Bentonite–carbon samples BC/NaCl and BC/KCl were prepared with the addition of NaCl and KCl (10 g each per 600 g of BC); BC/KCl + 20 g wood sawdust; and BC/NaCl with the addition of 10 g of straw [79, 80]. Bentonite/lignite charcoal (1:2 w/w) (BC) was grinded and activated using sulfuric acid and then heated in a muffle furnace without oxygen at 950°C for 45 min (weight loss was 19%) and cooled. Similarly, samples with addition of NaCl or KCl (10 g per 600 g of BC), sawdust to BC/KCl and straw to BC/NaCl (both raw organics of 20 g per 600 g of BC) were prepared and the weight loss was 20–26% [79, 80]. Various AC (initial, oxidized, reduced, catalytically activated), as well as graphitized carbons and carbon blacks, used on solid phase extraction (SPE) of trace amounts of different organics [82–87] were analyzed concerning CSE influence on the interfacial phenomena.

Fullerite C_{60}/C_{70} (weight ratio 0.85/0.15) was synthesized using the electric arc (200 A, 24 V) method (Frantsevich Institute for Problems of Materials Science, Kyiv, Ukraine) with evaporating a graphitic rod in a helium atmosphere at a pressure of 100 Torr [89]. The fullerene separation from the soot was performed in a Soxlet–type continuous extractor using toluene as a solvent. Toluene evaporation was carried out in a rotary evaporator at 40°C. After crystallization of fullerite, it was washed with diethyl ether and dried. A small amount (~1 wt.%) of organic solvents could remain in the material because of the relatively low temperatures of heating of fullerite [89].

Multi–walled carbon nanotubes (MWCNT) of 20–50 nm in diameter and 10–15 layers were synthesized using chemical vapor deposition (CVD) process in a flow rotary reactor in an inert (Ar) atmosphere at 700°C (Chuiko Institute of Surface Chemistry (CISC) of National Academy of Sciences of Ukraine, Kyiv, Ukraine). A catalyst was prepared using a mixture of precursors $Al(NO_3)_3 \cdot 9H_2O$, $NiCl_2 \cdot 6H_2O$, and $(NH_4)_6Mo_7O_{24} \cdot 4H_2O$ calcined and mixed with inert nanosilica A–300 (ratio 1 : 1.5 w/w) to prevent strong agglomeration of CNT. A mixture of propane and butane (flow 400 cm^3/min) and hydrogen (flow 200 cm^3/min) was blown through the catalyst layer at 700°C for 60–90 min. To purify MWCNT from mineral components, they were treated with a mixture of ammonium bifluoride and hydrochloric acid. The final amount of ash was lower than 1 wt.% [90–97].

Single (SLGO) and multi (MLGO) layer graphene oxides (both produced by CheapTubes Inc or MLGO by CISC) were used in comparative investigation of sorption of water alone and in mixtures with CH_4, C_6H_6, C_6D_6, $CHCl_3$, $CDCl_3$, $(CH_3)_2SO$, $(CD_3)_2SO$, CCl_4, or HCl (all compounds were of NMR spectroscopy grade). All graphene materials were washed in alkali solution, followed by spin centrifugation, followed by an acidic solution to regenerate the surface acidic groups, and finally with deionized water till a neutral pH was achieved, before NMR measurements [97].

On forensic related studies, sixteen psychotropic substances (Table 1) divided into three groups: (I) amphetamine and hydroxyamphetamine, (II) metoxyamphetamines, and (III) methylenedioxyamphetamines were studied. Amphetamine sulfate and hydrochlorides of 3,4–methylenedioxyamphetamine, 3,4–methylenedioxymethamphetamine and 3,4–methylenedioxy-ethylamphetamine were analytical standards (Sigma, USA), whereas other methoxyamphetamines were synthesized at the forensic laboratory of Internal Security Agency (Warsaw, Poland). 5–Bromo–3,4–dimetoxyamphetamine and 5–bromo–3,4–methylenedioxyamphetamine were prepared using 3,4–dimetoxyamphetamine and 3,4–methylenedioxyamphetamine reacting with bromine in acetic acid. The molecular structure and the purity of prepared compounds in the form

of hydrochlorides or free bases were confirmed by spectroscopic (^{1}H NMR, TPD–MS, FTIR) and chromatographic (GC, HPLC) methods [82–87].

Table 1. The S_{BET} and V_p values and other characteristics of CM calculated using the DFT (NLDFT, QSDFT, DFT) methods with the model of slit-shaped/cylindrical (carbons) or cylindrical (LiChrolut EN) pores

No	Adsorbent	S_{BET} (m^2/g)	S_{NLDFT} (m^2/g)	S_{QSDFT} (m^2/g)	S_{nano} (m^2/g)	$S_{meso(macro)}$ (m^2/g)
1	A2PS	1130	1132	1056	960	94
2	A2PS-O4	1142	1165	1064	1037	105
3	A2PS-O8	1122	1078	1034	1053	109
4	A2PS-H	1157	1205	1094	1093	108
5	A2PSC	46	54	48	38	8
6	A2PSCA	3	2	2	1	1
7	A2PSM	1457	1352	1338	1207	242(2)
8	A2PSMC	416	406	385	346	67(2)
9	A2PSMCA	48	44	43	26	21(1)
10	A2PSG	17	22	22	8	9
11	A2PSCa	992	1011	957	827	184(8)
12	A2PSCaG	40	50	49	11	24(5)
13	Coke	654	763	755	622	32
14	Coke-2h	708	834	815	675	34
15	Coke-3h	872	979	950	806	49
16	Coke-6h	1119	1096	1009	1056	63
17	Coke-8h	1223	1129	1036	1161	62
18	Coke-1h/Ca	577	620	631	489	77(3)
19	Coke-4h/Ca	630	673	719	547	79(5)
20	Coke-8h/Ca	880	861	851	682	194(4)
21	Coke-1h/Ca/C	265	317	343	225	35(2)
22	Coke-4h/Ca/C	352	387	404	298	50(4)
23	Coke-8h/Ca/C	432	453	479	360	61(6)
24	Carboprep	135	138	133	58	72
25	Envicarb	97	99	103	42	48
26	Hypercarb	95	102	100	37	55
27	LiChrolut EN	1423	1401	1275	272	1240
28	Norit R 0.8 Extra initial	1443	1374	1297	1223	221
29	Deashed	1360	1290	1219	1161	200
30	Air-frozen	1362	1290	1212	1143	220
31	Suspended	1489	1586	1515	1242	247
32	Suspended, frozen	1449	1555	1412	1196	254
33	Suspended, frozen, deashed	1397	1464	1427	1172	226
34	Deashed, H_2 reduced at 800ºC	1446	1545	1505	1201	246
35	Deashed, oxidized at 250ºC	1539	1532	1442	1247	292
36	Deashed, oxidized at 350ºC	1520	1547	1430	1194	327
37	W	2452	2008	2263	1929	445
38	WO	2091	1784	2002	1647	382
39	ACR1 (Zerolite resin precursor)	1222	1090	1049	715	484
40	ACR2 (Wofatite)	637	702	641	504	167
41	ACR3 (Dowex)	766	861	847	577	242
42	ACR3g (Dowex)	45	45	43	20	24
43	Char/clay (BC/NaCl)	40	37	36	4	16(21)
44	Char/clay (BC/KCl)	71	56	53	45	26(1)
45	Char/clay (BC/NaCl/straw)	135	138	126	107	27(1)
46	Char/clay (BC/KCl/sawdust)	59	53	50	7	29(23)

Continued Table 1

No	Adsorbent	V_p (cm^3/g)	V_{NLDFT} (cm^3/g)	V_{QSDFT} (cm^3/g)	V_{nano} (cm^3/g)	V_{meso} (cm^3/g)	V_{macro} (cm^3/g)
1	A2PS	0.72	0.67	0.66	0.51	0.20	0.01
2	A2PS-O4	0.73	0.68	0.67	0.51	020	0.02
3	A2PS-O8	0.71	0.67	0.66	0.50	0.20	0.01
4	A2PS-H	0.73	0.69	0.67	0.52	0.20	0.01
5	A2PSC	0.08	0.07	0.07	0.03	0.04	0.01
6	A2PSCA	0.01	0.01	0.01	0	0.01	0
7	A2PSM	1.36	1.26	1.25	0.62	0.70	0.05
8	A2PSMC	0.51	0.47	0.47	0.18	0.29	0.05
9	A2PSMCA	0.14	0.12	0.12	0.02	0.10	0.02
10	A2PSG	0.18	0.08	0.08	0.01	0.11	0.06
11	A2PSCa	1.58	1.06	1.07	0.46	0.67	0.45
12	A2PSCaG	0.34	0.19	0.20	0.01	0.09	0.25
13	Coke	0.40	0.37	0.37	0.31	0.09	0.01
14	Coke-2h	0.42	0.40	0.39	0.33	0.09	0.01
15	Coke-3h	0.52	0.48	0.47	0.40	0.11	0.01
16	Coke-6h	0.62	0.59	0.57	0.49	0.13	0.01
17	Coke-8h	0.69	0.65	0.63	0.54	0.14	0.01
18	Coke-1h/Ca	0.62	0.55	0.55	0.22	0.32	0.09
19	Coke-4h/Ca	0.69	0.60	0.61	0.22	0.34	0.12
20	Coke-8h/Ca	1.06	0.90	0.91	0.37	0.60	0.09
21	Coke-1h/Ca/C	0.33	0.29	0.29	0.11	0.17	0.06
22	Coke-4h/Ca/C	0.47	0.40	0.40	0.13	0.23	0.11
23	Coke-8h/Ca/C	0.55	0.46	0.47	0.15	0.26	0.14
24	Carboprep	0.49	0.48	0.47	0.05	0.43	0.01
25	Envicarb	0.75	0.45	0.54	0.03	0.50	0.22
26	Hypercarb	0.62	0.56	0.56	0.04	0.55	0.03
27	LiChrolut EN	0.83	0.78	0.76	0.07	0.76	0
28	Norit R 0.8 Extra initial	0.81	0.76	0.74	0.56	0.24	0.01
29	Deashed	0.75	0.71	0.69	0.54	0.21	0.01
30	Air-frozen	0.76	0.71	0.70	0.52	0.23	0.01
31	Suspended	0.84	0.79	0.77	0.55	0.27	0.01
32	Suspended, frozen	0.81	0.77	0.75	0.52	0.28	0.01
33	Suspended, frozen, deashed	0.78	0.74	0.72	0.52	0.26	0.01
34	Deashed, H_2 reduced at 800	0.81	0.76	075	0.53	0.27	0.01
35	Deashed, oxidized at 250ºC	0.87	0.82	0.80	0.55	0.31	0.01
36	Deashed, oxidized at 350ºC	0.86	0.81	0.79	0.51	0.34	0.01
37	W	1.24	1.11	1.14	0.79	0.43	0.02
38	WO	1.07	0.97	0.99	0.70	0.37	0.01
39	ACR1 (Zerolite resin	2.56	2.46	2.46	0.51	2.07	0.04
40	ACR2 (Wofatite)	0.62	0.58	0.58	0.27	0.34	0.01
41	ACR3 (Dowex)	0.79	0.69	0.70	0.31	0.46	0.02
42	ACR3g (Dowex)	0.19	0.16	0.17	0.02	0.16	0.02
43	Char/clay (BC/NaCl)	0.12	0.08	0.08	0	0.03	0.09
44	Char/clay (BC/KCl)	0.12	0.10	0.10	0.03	0.09	0
45	Char/clay (BC/NaCl/straw)	0.19	0.14	0.14	0.05	0.10	0.03
46	Char/clay (BC/KCl/sawdust)	0.27	0.10	0.10	0	0.06	0.12

Note. SSA of macropores is not shown for carbons if it is smaller than 1 m^2/g.

Three sets of explosives were used as SPE probes to study concentration and recovery processes using various carbons (AC, carbon blacks, cokes): (i) nitrate esters: nitroglycerine (glycerol trinitrate, label NG), nitroglycol (ethylene glycol dinitrate, EGDN), and pentaerythritol tetranitrate (PETN); (ii) cyclic nitroamines: hexogen (1,3,5–trinitro–1,3,5–triazacyclohexane,

RDX) and octogen (1,3,5,7–tetranitro–1,3,5,7–tetrazacyclooctane, HMX); and (iii) nitroaromatics: 2,4,6–trinitrotoluene (TNT), 1,3,5–trinitrobenzene (TNB), tetryl (2,4,6,N–tetranitro–N–methylaniline, TNMA), hexyl (2,2', 4,4', 6,6'–hexanitrodiphenylamine, HNDPA), and 2,2', 4,4', 6,6'–hexanitrodibenzyl (HNDB) (Promochem and Institute of Organic Chemistry, Warsaw) [82-87]. Solvents (HPLC grade): water, acetonitrile, methanol, dimethylformamide (DMFA), tert–butyl–methyl ether, dimethyl sulfoxide (DMSO, Lab–Scan, Ireland), isopropyl alcohol, tetrahydrofuran, ethyl acetate, and chloroform (Merck) were used.

The studied CM represent a large set of various systems of different particulate morphology and texture. Atomic Force Microscopic (AFM) images (Fig. 1) have been recorded using a NanoScope III (Digital Instruments, USA) apparatus using a Tapping Mode AFM measurement technique or using Nanoscope Multimode IIIa (Veeco, Santa Barbara, CA, USA) [88]. Before AFM scanning, powder samples of fumed oxides were slightly smoothed by hand pressing using a glass plate that does not affect the structure of primary and secondary particles, changing only the structure of visible flocks.

Scanning electron microscopy (SEM) images (Figs. 2 and 3) of dried samples have been recorded using a FE–SEM (Hitachi S–4700, Japan) or a Quanta 3D FEG (FEI, Japan) at an operating voltage of 5 or 15 kV at the magnification range of 5000–100000.

High resolution transmission electron microscopy (HRTEM) images (Figs. 4–7) have been recorded for various carbons using a JEM–2100F (Japan), a JEOL 2010FX TEM operated at 200 kV or a TECNAI G2 F30 microscope (FEI–Philips) at an operating voltage of 300 kV. TEM images were treated using ImageJ and Fiji software.

Table 2. The textural characteristics of char (C–0) and AC (carbonized phenol formaldehyde resin beads, C–0 then activated by CO or water) *vs*. the burn–off degree corresponding to the numbers in sample labels (Figs. 1 and 2)

Sample	S_{BET} m^2/g	S_{nano} m^2/g	S_{meso} m^2/g	S_{macro} m^2/g	V_p cm^3/g	V_{nano} cm^3/g	V_{meso} cm^3/g	V_{macro} cm^3/g
C–0	549	493	45	11	0.98	0.26	0.25	0.47
C–25	1082	1011	65	6	1.01	0.51	0.31	0.19
C–45	1615	1510	101	4	1.32	0.75	0.41	0.16
C–62	2270	2090	175	4	1.68	1.00	0.51	0.18
C–75	3047	2626	413	6	2.35	1.22	0.90	0.22
C–86	3463	2181	1279	3	2.32	1.31	0.89	0.12
Wf–24	963	894	67	3	0.91	0.46	0.35	0.10
Wf–45	1194	1199	91	5	1.21	0.62	0.43	0.16
Wf–66	1780	1606	171	5	1.61	0.81	0.63	0.17
Wf–77	2080	1826	253	3	1.83	0.89	0.56	0.12
W–43	1189	1118	62	9	1.24	0.58	0.27	0.39
W–59	1677	1553	118	5	1.44	0.79	0.45	0.21
W–73	2069	1855	208	6	1.83	0.92	0.67	0.24
W–88	2793	2288	500	6	2.35	1.11	1.11	0.23

Note. C–*i* is activated by CO, Wf–*i* and W–*i* are activated by water vapor in fixed bed and fluidized bed reactors, respectively. Pore ranges: nanopores < 1 nm, mesopores 1 nm – 25 nm, and macropores > 25 nm in pore radius (R) or half-width (x).

Low-temperature nitrogen adsorption–desorption isotherms were recorded at 77.4 K using a Micromeritics ASAP 2010 or 2405N adsorption analyzer. The specific surface area (SSA) of sorbents (Table 1, S_{BET}) was calculated according to the standard BET method [41]. Additionally, the SSA values were computed using nonlocal (NLDFT, Table 1, S_{NLDFT}) and quenched solid (QSDFT, S_{QSDFT}) DFT methods. The total pore volume (V_p) was evaluated by converting the volume of nitrogen adsorbed at $p/p_0 \approx 0.98–0.99$ (p and p_0 denote the equilibrium pressure and the saturation pressure of nitrogen at 77.4 K, respectively) to the volume of liquid nitrogen per gram of the adsorbent [42]. The pore size distribution (PSD) functions $f(x)$ (differential $f_V(x) \sim dV_p/dx$ and $f_S(x) \sim dS/dx$, where x is the pore half-width or radius) were calculated using Density Functional Theory (DFT) [88].

Table 3. Textural characteristics of chars (carbonized phenol formaldehyde resin) and AC

Sample	S_{BET} m^2/g	S_{SAXS} m^2/g	S_{nano} m^2/g	S_{meso} m^2/g	S_{macro} m^2/g	V_p cm^3/g	V_{nano} cm^3/g	V_{meso} cm^3/g	V_{macro} cm^3/g	Δw	Pore model	Method
C–0	568	611	486	81	1	0.65	0.25	0.34	0.07	0.075	Slit	DFT
C–30	993	1081	884	108	2	1.08	0.45	0.54	0.09	0.079	Slit	DFT
C–45	1351	1631	1205	144	3	1.44	0.59	0.69	0.16	0.138	Slit	DFT
C–60	1999	2211	1729	250	19	1.97	0.66	0.64	0.67	0.561	Slit	DFT
			1772	202	19	1.97	0.57	0.96	0.44	0.065	Cyl	DFT
			1125	860	13	1.97	0.42	1.22	0.33	0.051	Cyl	MND
			1400	590	9	1.97	0.59	1.18	0.20	0.264	S/C/V*	MND
NC–0	585	699	507	78	0	0.65	0.29	0.37	0	–0.029	Slit	DFT
NC–36	1158	1346	1046	112	0	1.03	0.56	0.47	0	0.014	Slit	DFT
NC–36A	1173	1268	1055	119	0	1.05	0.56	0.49	0	0.040	Slit	DFT
C–5A	747	904	702	45	0	0.49	0.37	0.12	0	0.028	Slit	DFT
			610	137	0	0.49	0.27	0.21	0.003	–0.189	Cyl	MND
C–5B	756	826	735	22	0	0.41	0.37	0.04	0.001	0.059	Slit	DFT
Norit RBX	1029	1120	996	31	2	0.51	0.40	0.04	0.07	0.417	Slit	DFT
			793	235	0	0.51	0.31	0.19	0.01	–0.037	Cyl	MND

Note. Δw is the relative deviation of the pore shape from the model (slitshaped – slit, cylindrical – cyl, slitshaped and cylindrical pores and voids between spherical particles – SCV). The S_{nano}, S_{meso}, and S_{macro} values have been normalized that $S_{nano} + S_{meso} + S_{macro} = S_{BET}$. *Relative contributions of slit–shaped and cylindrical pores and voids between nanoparticles are 0.616, 0.302 and 0.082, respectively, for C–60.

Table 4. Structures, labels, molecular weight (M*W*), and dipole moment (μ, HF/6–31G(d, p)) of amphetamine derivatives

1	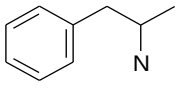 $C_9H_{13}N$, Amphetamine (label A), M*W* = 135.21, μ = 1.86 D	9	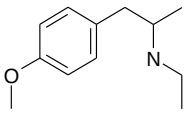 $C_{12}H_{19}NO$, 4–metoxy–N–ethylamphetamine, (4–MEA), MW = 193.29, μ = 1.69 D
2	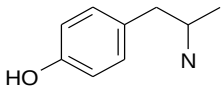 $C_9H_{13}NO$ p–hydroxyamphetamine (4–OHA), M*W* = 151.21, μ = 2.41 D	10	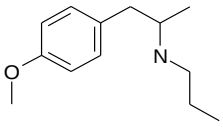 $C_{13}H_{21}NO$, 4–metoxy–N–propylamphetamine, (4–MPA), MW = 207.32, μ = 1.66 D
3	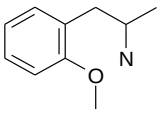 $C_{10}H_{15}NO$ 2–metoxyamphetamine (2–MA), MW = 165.24, μ = 1.68 D	11	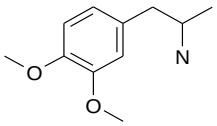 $C_{11}H_{17}NO_2$ 3,4–dimetoxyamphetamine (3,4–DMA), MW = 195.26, μ = 2.48 D
4	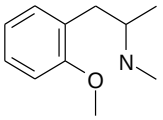 $C_{11}H_{17}NO$ 2–metoxy–N–methylamphetamine (2–MMA), MW = 179.26, μ = 1.44 D	12	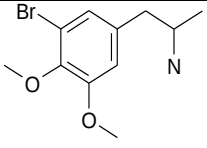 $C_{11}H_{16}BrNO_2$ 5–bromo–3,4–dimetoxyamphetamine (5–Br,3,4–DMA), MW = 274.16, μ = 5.35 D
5	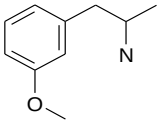 $C_{10}H_{15}NO$ 3–metoxyamphetamine (3–MA), MW = 165.24, μ = 1.35 D	13	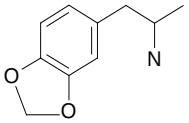 $C_{10}H_{13}NO_2$ 3,4–methylenedioxyamphetamine (MDA), MW = 179.22, μ = 6.16 D

Continued Table 4

6	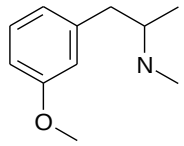 $C_{11}H_{17}NO$ 3–metoxy–N–methylamphetamine (3–MMA), MW = 179.26, μ = 2.67 D	14	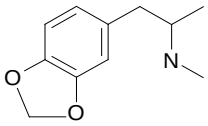 $C_{11}H_{15}NO_2$ 3,4–methylenedioxymethamphetamine (MDMA), MW = 193.25, μ = 5.81 D
7	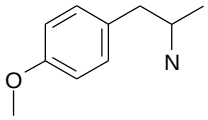 $C_{10}H_{15}NO$ 4–metoxyamphetamine (4–MA), MW = 165.24, μ = 1.79 D	15	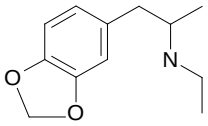 $C_{12}H_{17}NO_2$ 3,4–methylenedioxyethylamphetamine (MDEA), MW = 207.27, μ = 5.77 D
8	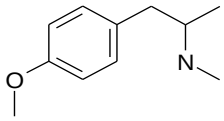 $C_{11}H_{17}NO$ 4–metoxy–N–methylamphetamine (4–MMA), MW = 179.26, μ = 1.67 D	16	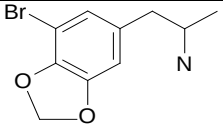 $C_{10}H_{12}BrNO_2$ 5–bromo–3,4–methylenedioxyamphetamine (5–BrMDA), MW = 258.11, μ =6.60 D

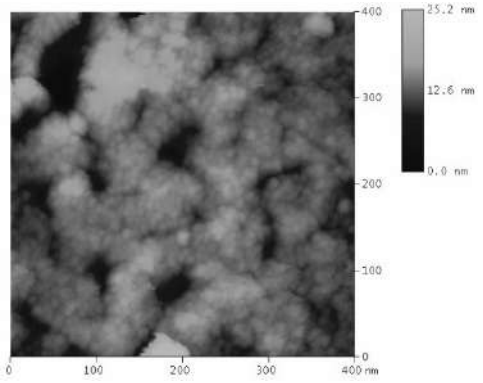

Fig. 1. AFM image of AC sample sowing nanoparticles and their tight aggregates

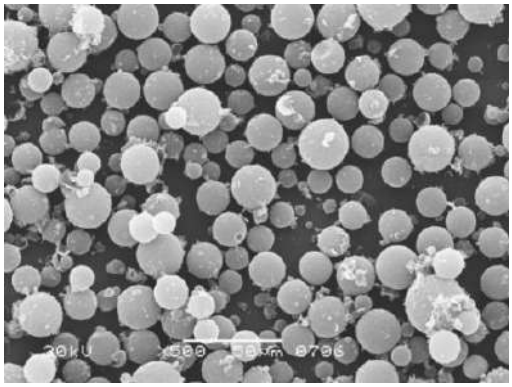

Fig. 2. SEM image of a char with spherical microparticles, composed of nanoparticles and their aggregates (carbonized phenol formaldehyde resin)

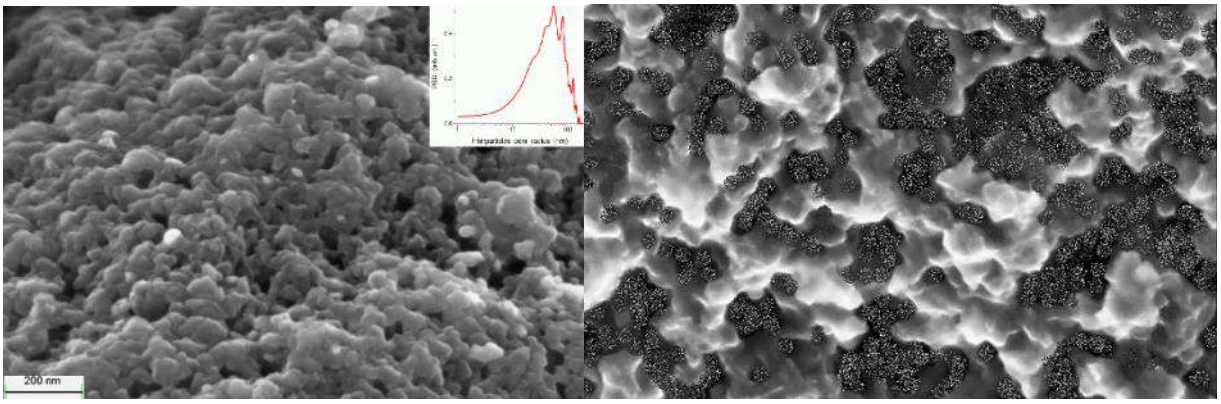

Fig. 3. SEM image of nanoparticles and their aggregates of AC (insert shows interparticle PSD mainly in the 10-120 nm range in radius) and a model of partial coverage of a surface upon probe clustered sorption

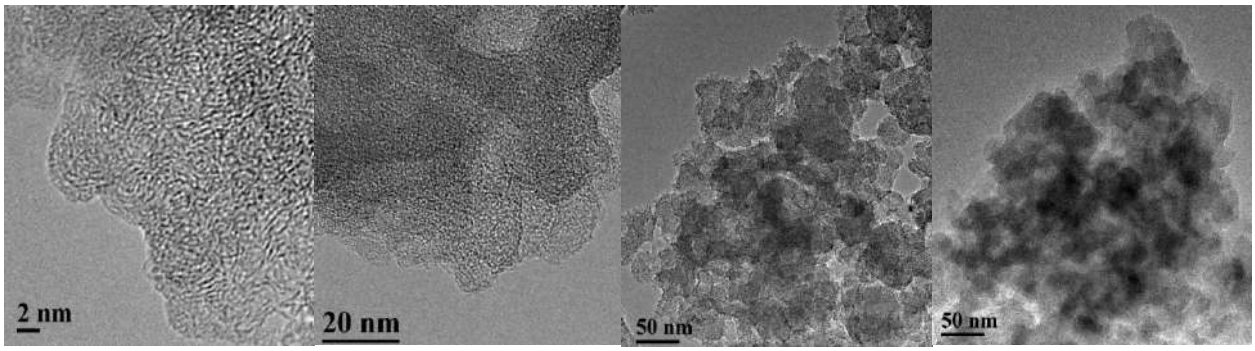

(*a*) (*b*) (*c*) (*d*)

Fig. 4. TEM images of nanoparticles and their aggregates of chars (carbonized phenol formaldehyde resin) at scale bars (*a*) 2 nm, (*b*) 20 nm, and (*c*, *d*) 50 nm

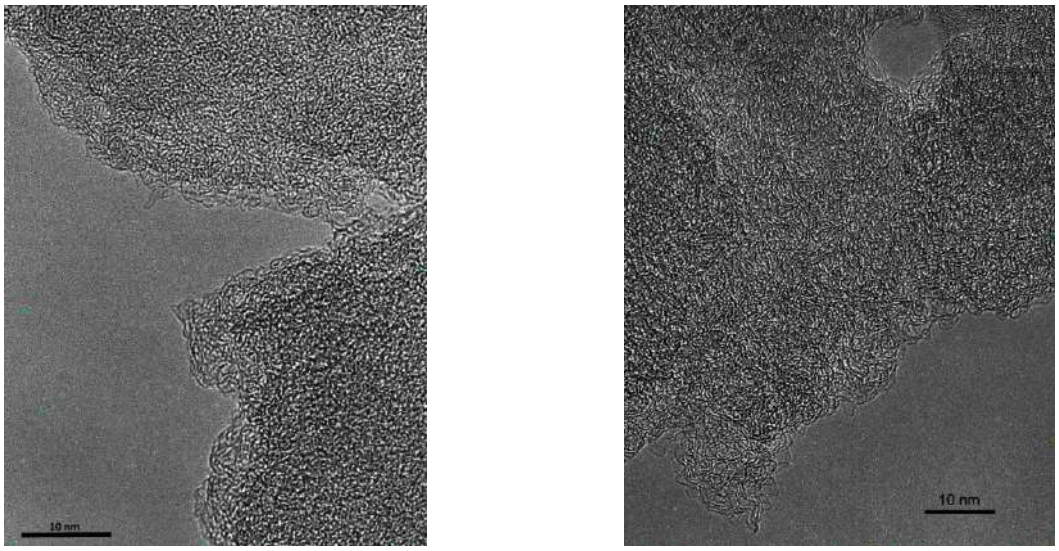

(*a*) (*b*)

Fig. 5. TEM images of nanoporous nanoparticles of (*a*) char C–0 (carbonized phenol formaldehyde resin, S_{BET} = 590 m^2/g, V_p = 0.95 cm^3/g) and (*b*) related AC C–50 with 50% burn–off degree (1664 m^2/g, 1.49 cm^3/g)

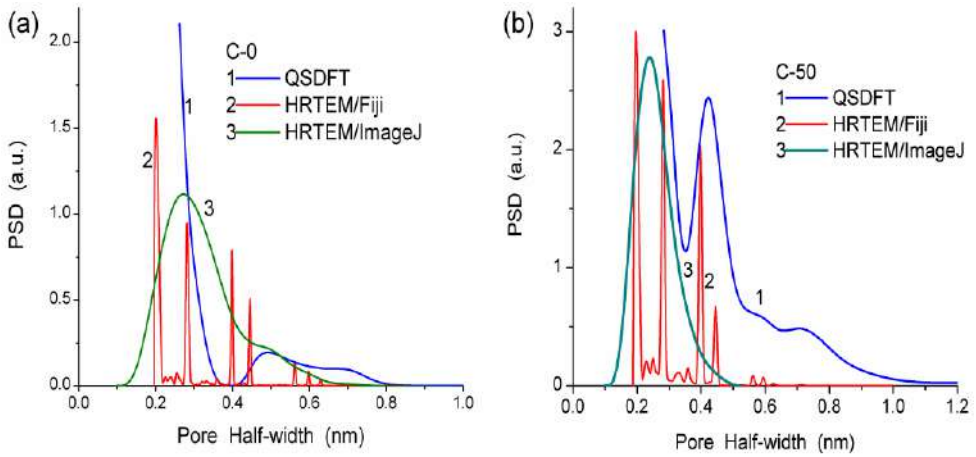

Fig. 6. Pore size distributions in nanoparticles (in the nanopore range) of (*a*) C–0 and (*b*) C–50 calculated using three methods

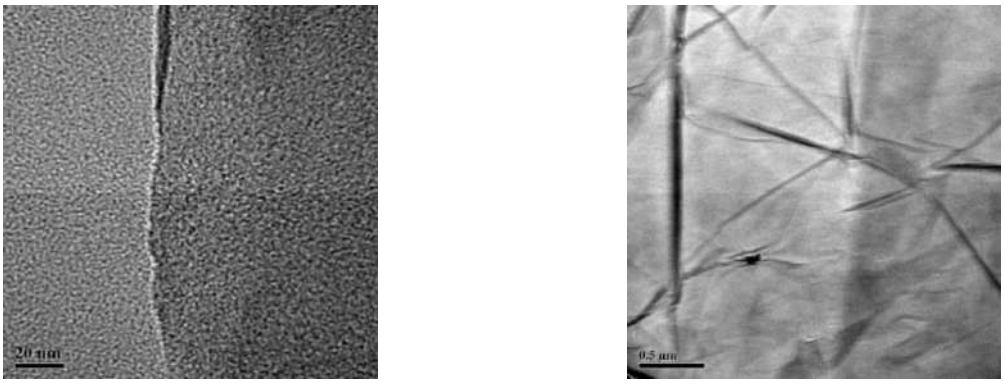

Fig. 7. TEM images of MLGO of different magnification

To calculate the density of a gaseous adsorbate (nitrogen) at a given pressure p, the generalized Bender equation [98] was applied. The nitrogen desorption data were utilized to compute the $f(x)$ functions using slit-shaped (for carbons with narrow PSD related to nanopores and narrow mesopores) or slit-shaped/cylindrical (carbons with broad PSD) pores in carbons and modified (transformed into a self-consistent procedure [81]) regularization procedure CONTIN [99] under nonnegativity condition ($f(x) \geq 0$ at any x) with a fixed regularization parameter $\alpha = 0.01$. The PSD functions were recalculated into incremental PSD functions (IPSD)

$$\Phi_{V,S}(x_i) = 0.5(f_{V,S}(x_i) + f_{V,S}(x_i))(x_i - x_{i-1})V_p / \int_{x_{\min}}^{x_{\max}} f_{V,S}(x)dx \,. \tag{1}$$

The NLDFT [100] and QSDFT [101] methods were used with models of slit-shaped or slit-shaped/cylindrical pores in carbons.

The pore size distribution (PSD) functions can be calculated using overall equation (with the framework of Density Functional Theory, DFT) [102-105]

$$W(p) = v_M \left[\int_{\sigma_{ss}/2}^{r_k(p)} \rho_f(R) f(R) dR + \int_{r_k(p)}^{R_{\max}} \frac{t}{R - \sigma_{ss}/2} \rho_M(R) f(R) dR \right], \tag{2}$$

where W is the sorption, where v_M the liquid molar volume, ρ_f the fluid density in occupied pores, ρ_m the density of the multi–layered adsorbate in pores, r_k the radius of pores occupied at the pressure p, σ_{ss} is the collision diameter of the surface atoms, R is the pore radius or half-width. To calculate the density of a gaseous adsorbate (nitrogen) at a given pressure p, the Bender equation [98] may be used

$$p = \rho T[R_g + B\rho + C\rho^2 + D\rho^3 + E\rho^4 + F\rho^5 + (G + H\rho^2)\rho^2 \exp(-a_{20}\rho^2)], \tag{3}$$

where $B = a_1 - a_2/T - a_3/T^2 - a_4/T^3 - a_5/T^4$; $C = a_6 + a_7/T + a_8/T^2$; $D = a_9 + a_{10}/T$; $E = a_{11} + a_{12}/T$; $F = a_{13}/T$; $G = a_{14}/T^3 + a_{15}/T^4 + a_{16}/T^5$; $H = a_{17}/T^3 + a_{18}/T^4 + a_{19}/T^5$; $a_{20} = \rho_c^{-2}$; a_i are constants, and R_g is the gas constant. Transition from gas (subscript g) to liquid (l) or fluid in the form of multi–layered adsorbate in pores (m) can be linked to the corresponding fugacity f

$$\ln \frac{f(T,\rho)}{R_g T\rho} = \frac{p(T,\rho)}{R_g T\rho} - 1 + \frac{1}{R_g T} \int_0^{\rho} [p(T,\rho) - R_g T\rho] \frac{d\rho}{\rho^2} \tag{4}$$

and

$$f_{l,m} = f_g \exp(\frac{E_{i,m}}{RT}), \tag{5}$$

where E is the interaction energy of an adsorbate molecule with the pore walls and neighboring molecules, calculated with the LD potentials. Certain PSD have also been calculated using nonlocal DFT, NLDFT method (with the model of slitshaped, siltshaped/cylindrical or cylindrical pores in carbons) [100], quenched solid DFT (QSDFT) [101, 106], and modified Nguyen–Do (MND) method [102,103].

The specific surface area determined under the complex pore model (S_{sum}) can be calculated from the differential pore size distributions $f_{S,j}(R)$ as follows

$$S_{sum} = \sum_j c_j \int_{R_{min}}^{R_{max}} f_{S,j}(R)dR = \sum_j c_j \int_{R_{min}}^{R_{max}} \frac{w_j}{R}\left(f_{V,j}(R) - \frac{V_j}{R}\right)dR, \tag{6}$$

where R_{min} and R_{max} are the minimal and maximal values of pore radius (in this paper, R_{min} = 0.35 nm and R_{max} = 100 nm), w_j = 1 for ideal slitshaped pores, w_j = 2 and 3 for cylindrical and spherical pores, respectively, and $w_j \approx 1.36$ for a cubic lattice with nonporous spherical particles. The effective w_{ef} value for random aggregates with nonporous spherical particles under the SCR procedure can be estimated as follows

$$w_{ef} = \int R f_S(R)dR \Big/ \int f_V(R)dR. \tag{7}$$

For evaluation of deviation (Δw) of the pore shape from the model, a parameter

$$\Delta w = S_{BET} \Big/ \int_{R_{min}}^{R_{max}} f_S(R)dR - 1, \tag{8}$$

where R_{max} and R_{min} are the maximal and minimal pore radii, respectively, may be used as a criterion of the reliability of the pore model, since S_{BET} is a conventional parameter independent of the pore shape and material type.

To calculate the adsorption energy distribution functions, the Fowler–Guggenheim (FG) equation was used to describe localized monolayer adsorption with lateral interactions:

$$\theta_i(p,E) = \frac{Kp\exp(zw\Theta/k_BT)}{1 + Kp\exp(zw\Theta/k_BT)}, \tag{9}$$

where $K = K_0(T)\exp(E/k_BT)$ is the Langmuir constant for adsorption on energetically uniformed sites and the pre–exponential factor $K_0(T)$ is expressed in terms of the partition functions for isolated gas and surface phases, z is the number of nearest neighbors of an adsorbate molecule (assuming z = 4), w is the interaction energy between a pair of nearest neighbors, k_B is the Boltzmann constant, *e.g.*, zw/k_B = 380 K for nitrogen. The right term of Eq. (9) was used as the kernel in the overall adsorption isotherm equation to calculate the distribution function $f(E)$ of the nitrogen adsorption energy. The Langmuir eq. was also used as a kernel to compute the distribution functions of changes in the Gibbs free energy of adsorption.

The differential PSD functions $f(r)$ based on the small–angle X–ray scattering (SAXS) data could be calculated using the Fredholm integral equation of the first kind for scattering intensity $I(q)$ [107–109]

$$I(q) = C\int_{r_{min}}^{r_{max}} \frac{\left(\sin qr - qr\cos qr\right)^2}{(qr)^2} V(r)f(r)dr, \tag{10}$$

where C is a constant, $q = 4\pi\sin(\theta)/\lambda$ the scattering vector value, 2θ is the scattering angle, λ is the wavelength of incident X–ray, $V(r)$ is the volume of a pore with radius r (proportional to r^3), and $f(r)dr$ represents the probability of having pores with radius from r to $r + dr$. The values of r_{min} (= π/q_{max}) and r_{max} (= π/q_{min}) correspond to the lower and upper limits of the resolvable real

space due to instrument resolution. Equation (10) was solved using the modified CONTIN algorithm [99]. The $f(r)$ function could be converted into incremental PSD (IPSD) $\Phi(r_i) = (f(r_{i+1}) + f_V(r_i))(r_{i+1} - r_i)/2$ for a better view of the PSD at larger r values.

To calculate the particle size distribution (PaSD) functions based on the SAXS data, several models of particles (*e.g.*, spherical, cylindrical, lamellar ones, and various blends of them) could be used. For spherical particles, an integral equation similar to Eq. (10) could be written as follows

$$I(q) = C \int_{R_{min}}^{R_{max}} P(q,R) f(R) dR , \tag{11}$$

where C is a constant, R is the radius of particles, $f(R)$ is the distribution function (differential PaSD), and $P(R)$ is the form factor for spherical particles (the kernel of the integral equation): $P(q,R) = (4\pi R^3/3)^2[\Phi(q)]^2$ and $\Phi(q,R) = (3/(qR)^3)[\sin(qR) - qR\cos(qR)]$.

The PaSD concerning the volume of particles (as abundance in vol%) could be calculated as follows

$$\text{abundance(vol\%)} = R^3 f(R) / \int R^3 f(R) dR . \tag{12}$$

For cylindrical particles, there are two variable parameters, such as the radius (R) and length (H) of cylinders

$$I(q) = C \int_{H_{min}}^{H_{max}} \int_{R_{min}}^{R_{max}} f(H) f(R) P(q,H,R) dH dR , \tag{13}$$

where the kernel $P(q,H,R) = CV \int_0^{\pi/2} \frac{2J_1(qR\sin\theta)}{qR\sin\theta} \frac{\sin(0.5qH\cos\theta)}{0.5qH\cos\theta} \sin\theta d\theta$, $J_1(x)$ is the first–order Bessel function, $V = \pi R^2 H$ is the cylinder volume, and C is a constant.

For lamellar particles

$$I(q) = C \int_{L_{min}}^{L_{max}} P(q,L) f(L) dL , \tag{14}$$

where the kernel $P(q,L) = (L/q)^2 \left[\frac{\sin(qL/2)}{(qL/2)} \right]^2$, L is the lamellar thickness, and the prefactor $(1/q^2)$ is the so–called Lorentz factor required to randomize the orientation of the lamellar particle in samples. In the case of complex systems, several models with various blends of spherical, cylindrical, and lamellar particles could be used with certain weight coefficients c_{sph}, c_{cyl}, and c_{lam}, respectively. For example, in the case of a complex model of particles, the integral equation may include three terms

$$I(q) = c_{sph} \int_{R_{min}}^{R_{max}} \left(\frac{4\pi R^3}{3} \right)^2 \left[\frac{3}{(qR)^3} (\sin(qR) - qr\cos(qR)) \right]^2 f(R) dR + c_{lam} \int_{L_{min}}^{L_{max}} (L/q)^2 \left[\frac{\sin(qL/2)}{(qL/2)} \right]^2 f(L) dL + c_{cyl} \int_{H_{min}}^{H_{max}} f(H) \int_{R_{min}}^{R_{max}} \frac{\pi R^2}{H} f(R) \int_0^{\pi/2} \sin\theta \frac{2J_1(qR\sin\theta)}{qR\sin\theta} \frac{\sin(0.5qH\cos\theta)}{0.5qH\cos\theta} d\theta dR dH , \tag{15}$$

where R is the radius of particles, H and R are the length and radius of cylinders, L is the lamellar thickness, $f(R)$, $f(L)$, and $f(H)$ are the distribution functions, $J_1(x)$ is the first–order Bessel function, c_x are the weight coefficients calculated, as well $f(x)$ functions, using a self–consistent regularization procedure. Equation (15) could be solved using a self–consistent regularization procedure [110].

The chord size distribution, $G(r)$, as a geometrical statistic description of a multiphase medium, can be calculated from the SAXS data [111, 112]

$$G(r) = C\int_0^\infty \left[K - q^4 I(q)\right] \frac{d^2}{dr^2}\left(-4\frac{\sin qr}{qr}\right) dq, \tag{16}$$

where K is the Porod constant corresponding to scattering intensity $I(q) \sim Kq^{-4}$ in the Porod range.

The specific surface area from the SAXS data can be calculated (in m^2/g) using the equation

$$S_{\text{SAXS}} = 10^4 \pi\phi(1-\phi)\frac{K}{Q\rho_a}, \tag{17}$$

where $\phi = \rho_a/\rho_0$ is the solid fraction of sorbent, and Q is the invariant

$$Q = \int_0^\infty q^2 I(q) dq. \tag{18}$$

The Q value is sensitive to the range used on integration of Eq. (18) (since experimental q values are measured between the $q_{\min}$ and $q_{\max}$ values, different from 0 and ∞). Therefore, the invariant value Q can be calculated using the equation

$$Q = \sum_{q_{\min}}^{q_{\max}} (I(q_i) - b) q_i^2 \Delta q_i + K / q_{\max}. \tag{19}$$

where b is a constant determined using the equation

$$I(q)q^4 = K + bq^4. \tag{20}$$

valid in the Porod range.

Note that the SAXS data treatments described above have been successfully used for carbon, silica, and polymeric materials in comparison with the adsorption results differently treated (DFT, NLDFT, QSDFT, *etc.*).

High-performance liquid chromatography (HPLC) analysis was performed using a LC–51 (Bruker) ternary gradient system with UV detection at 220 nm. The separation of analytes was carried out using an analytical BDS–Elite 5μm 150×4 mm column (ThermoHypersil, UK) and 10×4.6 mm precolumn slurry packed with LiChrospher RP–select B (Merck), all thermostated at 323 K. The injection volumes for eluates and standard solutions were 50 μl [82–87].

A linear binary gradient elution with isopropyl alcohol containing 5% (v/v) of acetonitrile and water was used for the separation of the studied explosives. The elution started from 5% (v/v) of isopropyl alcohol with the flow rate of 1.5 ml/min and reached 50% (v/v) of organic solvent in 8 min. The SPE recovery rates η were calculated by an external standard method from the peak heights. The calibration curves were obtained by linear regression in the range 0.25–30 μg/10 ml for nitroamines and nitroaromatics, but 1.25–150 μg/10 ml for nitrate esters. The correlation coefficients for the studied explosives obtained from 5 points were from 0.97 to 0.99. The mean values of the recovery rates were evaluated from six SPE measurements and the mean errors were less ±5% [82–87].

Low-temperature ^{1}H NMR spectra of static samples were recorded using a Varian 400 Mercury spectrometer (magnetic field 9.4 T) utilizing 60–90° pulses of 1–3 μs duration. Each spectrum was recorded by co-addition of eight scans with a 1-3 s delay between each scan. Relative mean errors were less than ±10% for signal intensity for significantly overlapped signals, and ±5% for separated single signals. Temperature control was within ±1 K. To prevent supercooling of water and solutions, the spectra were recorded from 180–200 K for initially precooled and then

heated samples to 280–290 K at a rate of 5 K/min, steps ΔT = 2–15 K, and maintained for 5–7 min for data acquisition at each temperature. Signals of frozen molecules and solids were not registered for static samples due to a narrow bandwidth (20 kHz) and large difference (at least, by three orders of magnitude) in transverse relaxation time (T_2) of mobile (liquid with longer T_2) and immobile (frozen or solid with shorter T_2) phases. Water (as well as other liquid sorbates) can be frozen in narrower pores at lower temperatures ($T < T_f$ = 273.15 K for water) according to the Gibbs–Thomson relation for the freezing point depression (FPD) for liquids in cylindrical pores at radius R [67, 113–115]

$$\Delta T_m = T_{m,\infty} - T_m(R) = -\frac{2\sigma_{sl}T_{m,\infty}}{\Delta H_f \rho R} = \frac{k_{GT}}{R}, \qquad (21)$$

where $T_m(R)$ is the melting temperature of ice *vs*. R, $T_{m,\infty}$ the bulk melting temperature, ΔH_f the bulk enthalpy of fusion, ρ the solid density, σ_{sl} the energy of solid–liquid interaction, and k_{GT} is the constant. Equation (21) is the base of NMR cryoporometry, giving information on unfrozen liquid (water, *etc.*) location in different pores that can be used for estimation of the PSD based on the cryoporometry. Under certain conditions, the cryoporometry and nitrogen (argon, CO_2, *etc.*) adsorption methods could give similar PSD. There are several kinds of bound water: (i) weakly (WBW, frozen at 265–273 K) and strongly (SBW, frozen at T < 265 K) bound waters; (ii) weakly (WAW, chemical shift of proton resonance δ_H = 0.5–2.0 ppm) and strongly (SAW, δ_H > 3 ppm) associated waters; and (iii) unbound water (UBW) similar to bulk water [67]. Deuterated $CDCl_3$, $(CD_3)_2SO$, *etc.* (H/D ≈ 1/1000) solvents were used to avoid their signals in the ^{1}H NMR spectra studied [67]. Applications of solid phase extraction (SPE) in analyses of trace amounts of drugs, explosives, toxins, *etc.* were described in detail elsewhere [82–87, 116–120]. Organic solutes/eluates were extracted on disk cartridges containing mixed-mode modified silica and on monolithic C–18 silica disk-packed spin column. Another type of the SPE column is a pipette tip in which C–18 monolithic silica bed is fixed. The recovery rate in SPE depends on many factors; therefore, simple correlations between adsorbate/adsorbent structures and the SPE effectiveness could be absent.

Relative mean errors in low-temperature ^{1}H NMR spectra are less than ±10% for signal intensity and ±1 K for temperature. The amounts of unfrozen interfacial water (C_{uw}) adsorbed on carbons frozen at 180 K < T < 273 K were estimated by comparison of integral intensity (I_{uw}) of ^{1}H NMR signal of unfrozen water with that (I_c) of water bound to carbon (in air) using a calibrated function $I_c = f(C^c)$, assuming $C_{uw} = \frac{C^c I_{uw}}{f(C^c)}$. The function $f(C^c)$ was obtained from the measurements of integral intensity for given amounts of water (C^c) sorbed in carbon pores. The signals of surface proton–containing groups and water molecules from ice were not detected due to features of the measurement technique and the short time T_2 of transverse relaxation of protons in solids (shorter than that of mobile phases by ca. three orders of magnitude). Changes in the Gibbs free energy (ΔG) of unfrozen adsorbed water were calculated (with relative mean error ±5%) using the known dependence of changes in the Gibbs free energy of ice on temperature [67]

$$\Delta G_{ice} = 0.0295 - 0.0413\Delta T + 6.64369\times10^{-5}(\Delta T)^2 + 2.27708\times10^{-8}(\Delta T)^3, \text{ (kJ/mol)}, \qquad (22)$$

where ΔT = 273.16 – T at $T \le$ 273.15 K. One can assume that water is frozen (T < 273 K) at the interfaces when $G = G_i$ and the value of $\Delta G = G - G_0$ equals $\Delta G_i = G_i(T) - G_i\big|_{T=273K}$ and corresponds to lowering of the Gibbs free energy of the interfacial water due to its interaction with the solid surfaces (G_0 denotes the Gibbs free energy of undisturbed bulk water). The used ^{1}H NMR technique with freezing–out of the bulk and interfacial water was described in detail elsewhere [67]. On the basis of this approach, one can calculate the concentrations of strongly (SBW) and

weakly (WBW) bound unfrozen waters, a maximal reduction of the Gibbs free energy of strongly and weakly bound water, and the Gibbs free energy (γ_S) of adsorption of water unfrozen at $T < 273$ K [67]

$$\gamma_S = K \int_0^{C_{uw}^{max}} \Delta G dC_{uw}\,, \tag{23}$$

where C_{uw}^{max} is the total amount of unfrozen water at $T = 273.15$ K.

One can assume that pore filling by water begins from narrow towards larger pores. Consequently, the air/water boundary shifts towards larger pores with increasing hydration degree *h*. Since the carbon surface is rather hydrophobic, a major portion of adsorbed water can represent a condensed 'liquid' phase, *i.e.*, clusters and droplets. If the pore volume partially infilled by water is V_p^f, and only a part of the pore volume and a part of the surface area are in contact with adsorbed water, Eq. (23) can be expressed as:

$$\gamma_S^* = K \frac{V_p}{V_p^f} \int_0^{C_{uf}^{max}} \Delta G dC_{uw}\,, \tag{24}$$

where *K* is a constant dependent on the units of γ_S* and ΔG (for re–calculation of energy from kJ/mol to mJ/m^2 units using known SSA of carbons).

Relatively long time of longitudinal relaxation of nuclear spins is frequently observed for molecules adsorbed in nanopores of carbonaceous sorbents [67]. This leads to a significant enhancement of the ^{1}H NMR signal intensity with lowering temperature because of an increase in population of the corresponding nuclear levels (Curie's law) [67]. There is a relationship for nuclear magnetization (*M*) of the system of *N* spins with the spin quantum magnitude *s* and the gyromagnetic ratio *g*

$$M = K_1 N g^2 h^2 I(s + 1) B_0 / 3kT, \tag{25}$$

where B_0 is the magnetic field intensity, and K_1 is a coefficient dependent on the conditions of NMR spectra recording. If the signal intensity equals *I* and *I'* at temperatures T_0 and T, respectively, then Curie's law could be considered as multiplying the intensity at T by α

$$\alpha = (I' - I)/(T - T_0). \tag{26}$$

Quantum chemical calculations using density functional theory (DFT) method were carried out using a hybrid functional ωB97X–D with the cc–pVDZ basis set with the Gaussian 16 [121], GAMESS 2024 R2 [122], AMS 2025.1 [123] program suites. The solvation effects were analyzed using the solvation method SMD [124] implemented in Gaussian and GAMESS. To compute the Gibbs free energy of solvation (subscript s), $\Delta G_s = G_l - G_g$, where G_l and G_g are the Gibbs free energies of a molecule free or bound to a carbon cluster in the liquid (subscript l) and gas (g) media, respectively. The calculations were performed taking into account zero–point and thermal corrections to the Gibbs free energy in the gas phase and for solved molecules and carbon clusters using the geometry optimized using ωB97X–D/cc–pVDZ.

The distribution functions of the δ_H values were calculated using a simple equation [125–127]

$$f(\delta_H) = (2\pi\sigma^2)^{-0.5} \sum_j \frac{\exp[-(\delta_j - \delta_H)^2]}{2\sigma^2}, \tag{27}$$

where *j* is a number of H atom, σ^2 is the distribution dispersion, and δ_j is the calculated value of the *j*–th H atom. Large structures (up to 15000 atoms) were calculated using the PM7 method (MOPAC 23.1.2) [128]. To calculate the $f(\delta_H)$ functions using the PM7 results, a calibration

function was used to describe the dependence between atomic charges q_H (PM7) and the δ_H values estimated

$$\delta_H = -27.38435372 + 83.67491184 \times q_H. \quad (28)$$

Eq. (28) was used to calculate the ^{1}H NMR spectra of water clusters alone and bound to sorbents. To calculate the equation constants in Eq. (28) in linear approximation, the δ_H values were determined for several water clusters calculated using the GIAO/ωB97X–D/cc–pVDZ method as the difference between nuclear magnetic shielding of tetramethylsilane (TMS) as standard (σ_{TMS}) and tested (σ) systems using isotropic values (magnetic shielding tensor spurs) $\sigma = (\sigma_{11} + \sigma_{22} + \sigma_{33})/3$. The same clusters were also calculated using the PM7 method to obtain the q_H values. Note that similar simple δ *vs*. *q* correlations are absent for non–hydrogen atoms due to complex factors affecting the magnetic shielding tensors of multi–electron atoms. Additionally, the equation constants for H atoms in different compounds (*e.g.*, various organics and inorganics) are different for different types of compounds and also depend on the types of ab initio or DFT and semiempirical (*e.g.*, PM3, PM6, and PM7) methods (MOPAC, versions 16, 22, and 23) used. Visualization of molecular structures was performed using several packages [129–132].

RESULTS AND DISCUSSION

Texture and particulate morphology

The morphologies (Figs. 1–7) and textures (Figs. 8–12 and Tables 1–3) of studied CM/CMC demonstrate broad distribution functions characteristic for mainly nonporous (small SSA and V_p) to strongly porous materials of high porosity and SSA (up to 3500 m^2/g) and possessing narrow or broad PSD, small or large pore volume, and different contributions of nano-, meso-, and macro-pores. Additionally, among the studied CM/CMC, there are graphitized samples or graphene oxides with more ordered and larger carbon sheets and completely amorphous samples with disordered structures and smaller sheets with different amounts of various surface O–containing functionalities (*vide infra*).

There are several types of carbon material modifications and treatments used (i) activation (by CO, CO_2, H_2O at high temperatures, Table 2, Figs. 1–12) resulting in an enhancement of porosity, SSA and changes in PSD (growing contribution of nanopores and narrow mesopores and decreasing contributions of broad mesopores and macropores); (ii) oxidation (e.g., by H_2O_2), which grows the amounts of O–containing functionalities and changes in the texture (e.g., A2PS, A2PS–O4, and A2PS–O8 or W and WO, Table 1, Figs. 8 and 9); (iii) reduction (e.g., by H_2) providing opposite surface modification; (iv) carbon deposition typically diminishing porosity; (v) catalytic modification affecting the textural and structural characteristics; and (vi) freezing of water (or other liquids and solutions) in pores that affects the textural characteristics. A wide set of CM/CMC (Fig. 8 and 9, Tables 1–3) and different techniques of their synthesis and treatments could provide the appearance of different features of CSE, CE, SPE, equilibrium and dynamic adsorption of various probe compounds in different dispersion media. Note that the SSA values determined using the BET, NLDFT, and QSDFT methods (Tables 1–3) differ and for some samples $S_{BET} > S_{NLDFT} > S_{QSDFT}$.

The main error (overestimation) in the estimated S_{BET} values is due to uncontrolled changes in the area occupied by N_2 molecules due to changes in the molecule orientation with respect to a sorbent surface, even in the case of CM and especially upon interactions of probe molecules with various surface functionalities [67–70, 133].

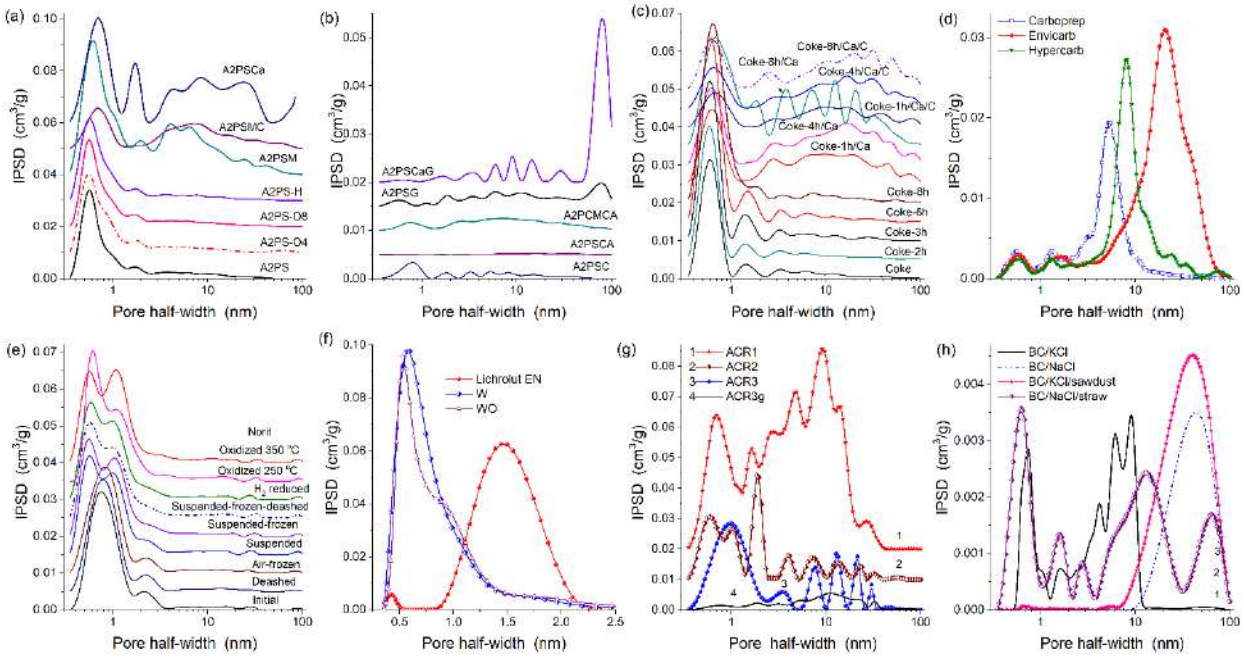

Fig. 8. Incremental pore size distributions with respect to the pore volume calculated using the DFT method (with self-consistent regularization) with the models of slit-shaped or slit-shaped/cylindrical (CM) and cylindrical (LiChrolut EN) pores for CM based on (*a*, *b*) A2PS, (*c*, *d*) coke, (*d*) Carboprep, Envicarb, Hypercarb, (*e*) Norit R 0.8 Extra, (*f*) W, WO, Lichrolut EN, (*g*) ARC, and (h) BC composites

There are certain correlations in changes in the textures of chars and related AC vs. the degree of burn-off (Tables 1–3). These correlations may be weak or absent if AC are prepared using different precursors and chars since the activation results depend not only on the degree of burn–off but also on the chemistry of raw materials and activation agents, as well as on other conditions (treatment time, temperature, pressure, atmosphere, particle sizes, *etc.*). Nanopores and narrow mesopores are mainly located in carbon nanoparticles, and they are of a slitshaped type (Figs. 1–12). Broad mesopores and macropores (complex non-slitstaped) are mainly located between nanoparticles tightly packed in microparticles (aggregates), which form visible carbon structures (see microscopic images). Burn-off activation of CM results in an increase in the porosity of nanoparticles (pore walls become thinner), but the nanoparticle sizes decrease. Therefore, the contribution of nanopores and narrow mesopores grows (Table 2), and their PSD peaks could shift toward larger pore sizes (Fig. 8–12) that provide larger SSA and V_p values (Tables 1-3). Additionally, smaller nanoparticles packed in the aggregates provide smaller voids between them. Therefore, carbon activation could lead to decreased contribution of broad mesopores and macropores. Any carbon modification could strongly affect the textural characteristics (Table 1–3, Figs. 1–14), as well as the surface structure. All the mentioned changes in the carbon characteristics can strongly affect the interfacial phenomena, occurring under different conditions, because of changes in CSE/CE, structure of adsorption layers, interactions of solvents with solutes, co-solvents, and active surface sites, and effects of dispersion media. CM are characterized by various morphologies and textures that result in very different nitrogen adsorption–desorption isotherms and PSD (Fig. 9). For various sorbents, there is a tendency for an increase in the pore volume with increasing surface area and an increase in the SSA with decreasing average pore sizes (Fig. 10). The scatter degree of V_p *vs.* S_{BET} (Fig. 10*a*) grows with decreasing temperatures of synthesis, activation, or pretreatment of solid samples. For example, porous silicas (silica gels, mesoporous ordered silicas, aerogels, precipitated silicas) were synthesized (200–500°C) and preheated (typically < 750°C) at much lower temperatures than that of the synthesis of fumed

silicas (1100–1300°C). CM (chars, activated carbons, carbon blacks) were synthesized and activated typically at 500°C < T < 900°C. The Pearson correlation coefficient values for a linear approximation of V_p *vs*. S_{BET} (Fig. 10*a*) grow in the same line as the temperature ranges of the synthesis/activation/treatment of the solid sorbents. The scatter degrees are much greater for V_p *vs*. R (Fig. 10*b*) and R *vs*. SSA (Fig. 10*c*) than for V_p *vs*. SSA (Fig. 10*a*) because equations for average pore sizes $R=2V_p/S_{BET}$ (cylindrical pores) and $x=V_p/S_{BET}$ (slitshaped pores) are valid (rather more or less accurate) only for the materials with monomodal PSD.

For activated carbons produced from the same precursors and chars using the same activation agent with only varied time of activation, all the textural characteristics demonstrate smooth changes in the values (Figs. 8–12). There is a tendency for the transformation of nanopores into narrow mesopores with opposite shifts of the PSD peaks of broad mesopores and macropores due to changes in primary nanoparticle sizes and their compaction in secondary structures. CM of different nature and particulate morphology can strongly differ concerning both nitrogen adsorption–desorption isotherms and PSD (Fig. 9).

According to quantum–chemical calculations, the orientation of the nitrogen molecules at a surface of various sorbents depends on the chemical composition of the surface and the presence of functional groups (such as O–H, C=O, COOH, *etc.*). As an example, the orientation of the nitrogen molecules is shown upon the interaction with activated carbon [88]. This effect leads to a decrease in the average value of the occupied surface area by nitrogen molecules (σ_0). In other words, the specific surface area (S_{BET}) values are overestimated by ca. 10–15%. This aspect should be considered if the estimation of the S_{BET} values is maximally accurate.

CM represent a large variety of porous or nanostructured materials such as exfoliated and oxidized graphite, graphene, graphene oxide, AC, carbon blacks, carbon nanotubes (CNT), fullerenes, and fullerites characterized by very different particulate morphology, texture, and surface structure. The CM could be divided into several classes with respect to their particulate morphology and porosity. First, purely nanoporous AC (microporous according to IUPAC; however, microporous nanoparticles are rather nonsense term, since micro is 10^{-6} and nano is 10^{-9}, *i.e.*, smaller one includes larger one) characterized by the nitrogen adsorption–desorption isotherms with a plateau onset at relatively low p/p_0 = 0.20–0.25 without a hysteresis loop (Fig. 9). Second, nano/mesoporous AC (biporous, Figs. 8–12) with nanopores ($x \leq 1$ nm) and narrow mesopores ($x < 3$ nm) characterized by nearly horizontal plateau (plateau onset shifts toward higher pressures) and narrow hysteresis loops. Third, nano/meso/macroporous AC is characterized by broad hysteresis loops (onset at $p/p_0 > 0.8$) and broad PSD. Thus, AC practically always include nanopores as their main attribute. Other types of CM, *e.g.*, carbon blacks, exfoliated graphite, CNT, *etc.*, can be mesoporous or meso/macroporous without nanopores. The use of several methods, appropriate for describing both open and closed pores in CM, is preferable. The morphological/textural features for chars and AC could be very different. For example, comparison of the SAXS and adsorption data for a char and AC shows that the difference strongly decreases for AC due to opening a significant part of the closed pores (present in chars) during activation.

For CM, the PSD could be broad with contributions of nano–, meso–, and macropores (Figs. 8–12). The textural features, depending on the burn–off degree, are more clearly visible for AC produced using the same precursors and chars. The contribution of narrow mesopores of 3–5 nm in size is small for all CM. This result for CM can be explained by features of voids (packing characteristics, see microscopic images in Figs. 1–7) between porous nanoparticles (PNP). For AC, pores at x < 2–3 nm are in PNP, but pores at x > 5 nm represent voids between PNP.

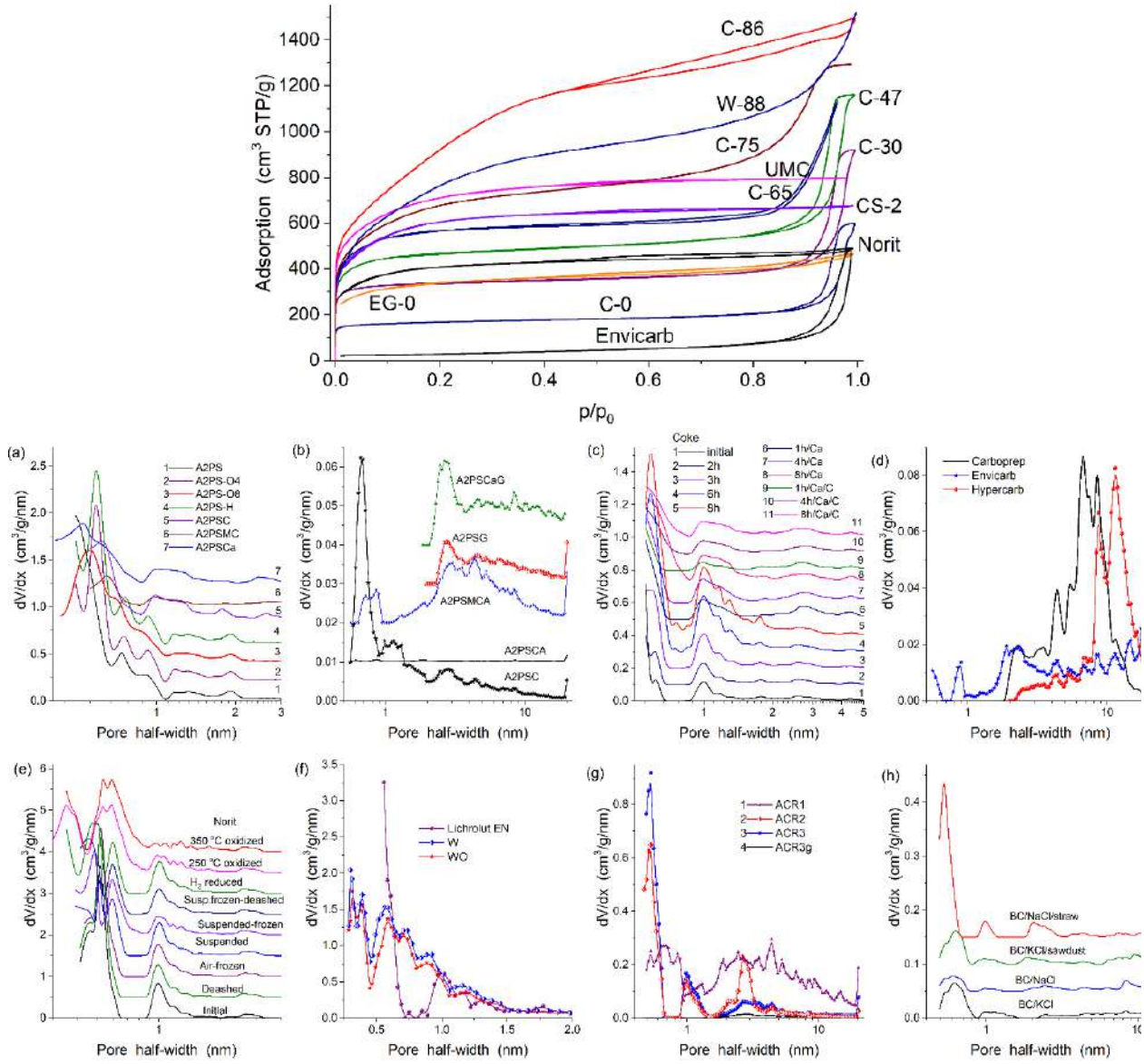

Fig. 9. Nitrogen adsorption–desorption isotherms (77.4 K) for AC prepared by carbonization of phenol formaldehyde resin beads (C–0, S_{BET} = 549 m^2/g, V_p = 0.98 cm^3/g) and activated by CO_2 at 1183 K (C–30, 993 m^2/g, 1.08 cm^3/g; C–47, 1648 m^2/g, 1.88 cm^3/g; C–65, 1840 m^2/g, 1.66 cm^3/g; C–75, 3047 m^2/g, 2.35 cm^3/g; C–86, 3463 m^2/g, 2.32 cm^3/g) or water vapor (W–88, 2793 m^2/g, 2.35 cm^3/g), various AC: Norit R 0.8 Extra (1553 m^2/g, 0.80 cm^3/g), CS–2 (coconut shells as a source, 2164 m^2/g, 1.04 cm^3/g), UMC (2300 m^2/g, 1.23 cm^3/g), EG–0 (plum stones as source, 1054 m^2/g, 0.72 cm^3/g), and Envicarb (carbon black, Supelco, 99 m^2/g, 0.75 cm^3/g); and NLDFT PSD with the models of slit–shaped or slit–shaped/cylindrical (CM) and cylindrical (LiChrolut EN) pores for CM based on (*a*, *b*) A2PS, (*c*, *d*) coke, (*d*) Carboprep, Envicarb, Hypercarb, (*e*) Norit R 0.8 Extra, (*f*) W, WO, LiChrolut EN, (*g*) ARC, and (h) BC

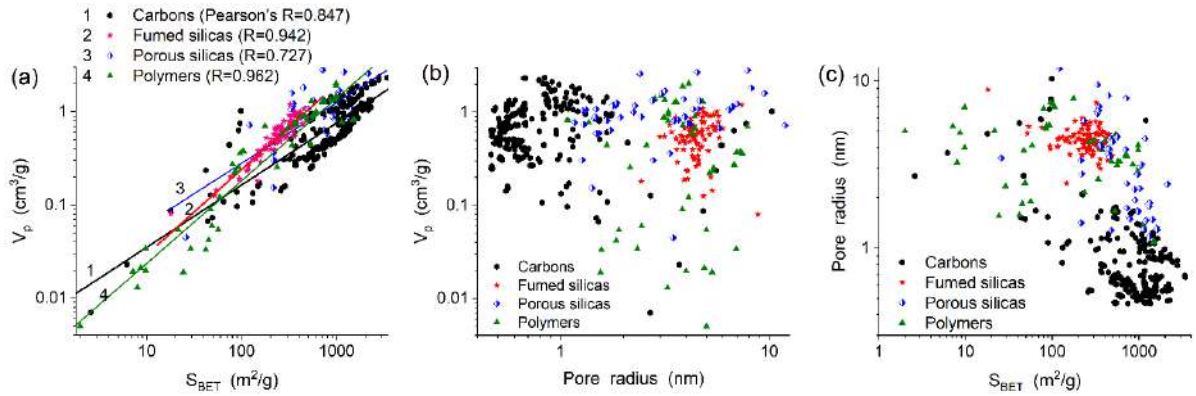

Fig. 10. Log–scale relationships for various sorbents (CM, silicas, and porous polymers) between (*a*) S_{BET} and V_p, (*b*, *c*) average pore radius ($R=2V_p/S_{BET}$ for fumed and porous silicas and polymers with a model of cylindrical pores) or average half-width ($x=V_p/S_{BET}$ for CM, slit-shaped pore model) and (*b*) V_p and (*c*) S_{BET} for various sorbents: fumed (93 samples) and porous silicas (56 samples), CM (230 samples), and polymers (53 samples) (Pearson correlation coefficients for linear approximation are shown in (*a*))

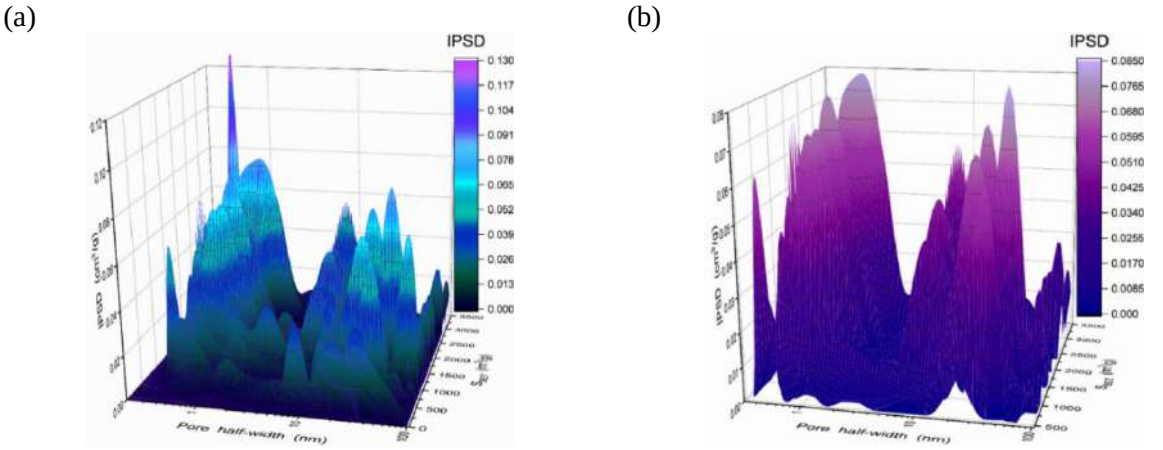

Fig. 11. DFT SCV/SCR IPSD for various CM (*a*) 230 samples and (*b*) 29 samples prepared using phenol formaldehyde resin beads as precursors carbonised in a CO_2 flow at 800°C and char activated with CO_2 (at 910°C) or H_2O (in a fixed bed reactor at 910°C or in a fluidized bed reactor at 750–770°C)

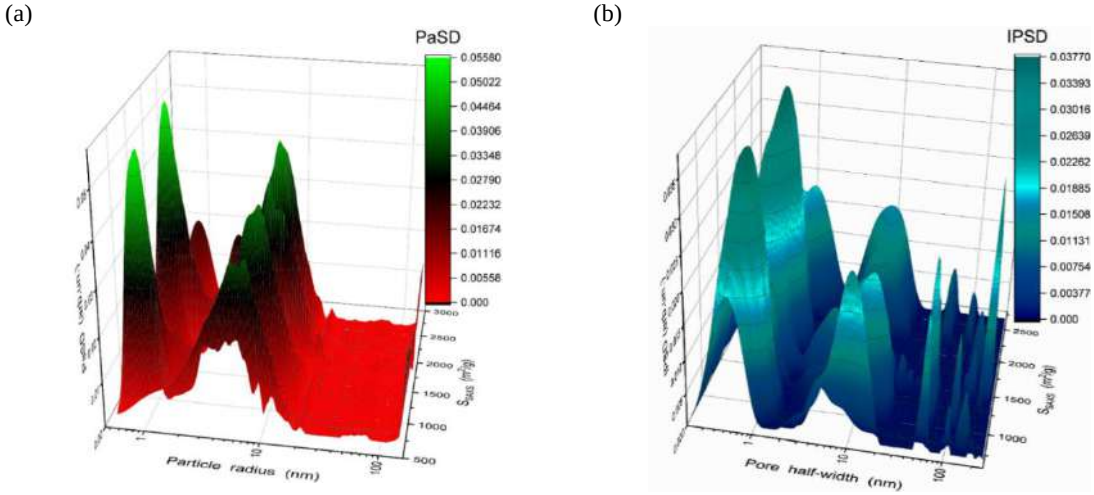

Fig. 12. (*a*) SAXS/SCR PaSD for various chars and AC (19 samples) and (*b*) SAXS IPSD for the same chars and AC (19 samples)

The adsorption and SAXS methods give a more comprehensive picture (Figs. 11 and 12) than that obtained within the scope of only one method (Figs. 8 and 9). Additional information could be also obtained using such microscopic methods as AFM, SEM, and TEM (Figs. 1–7). The microscopic images could be treated to obtain quantitative characteristics using various software (Fig. 6). Additional textural and other information could be obtained using various probe adsorbates or by estimating energetic characteristics of the probe interactions with sorbents [67, 88, 110].

Comparison of the textural characteristics computed using adsorption (open pores accessible for probe molecules) and SAXS (open and closed pores) data for CM (chars and AC) shows that their (adsorption and SAXS) difference decreases with increasing degree of burn–off.

Thus, based on the results, the most appropriate PSD (adsorption) and PaSD (SAXS) could be obtained using self–consistent procedures applied to integral equations describing pores of various shapes (slitshaped and cylindrical pores and voids between nanoparticles) in various materials (CM, *etc.*) and particles of various shapes (spherical, lamellar, and cylindrical). Useful quantitative morphological and textural information could be obtained from AFM, SEM, and HRTEM images treated using appropriate software. These data allow one to obtain information on the morphological and textural hierarchies of particles (nano-, micro-, and macro-particles) and pores (nano-, meso-, and macro-pores). Clear pictures on the particulate morphology and texture of various materials, such as various CM/CMC, could be obtained upon application of adsorption, SAXS, and microscopic methods with appropriate and correct treatments of the data. The application of one of these methods does not provide this possibility and some interpretations of the data could be incorrect that is of importance from a practical point of view. The surface structure play an important role in the interfacial phenomena that could be studied using spectroscopic, titration and other methods [67].

Titration of functionalities on the A2PS based CM (Table 5) was performed according to Boehm [134]. Dried carbon (1 g) was poured by 0.1 M NaCl (0.1 L) for 48 h. For titration of the most acidic COOH groups, 0.1 M $NaHCO_3$ (pK_2 = 6.37) was utilized. Less acidic carboxyls and hydroxy lactone groups were titrated using 0.05 M Na_2CO_3 (pK_2 = 10.75); hydroxyls akin to the phenolic type were titrated by 0.1 M NaOH (pK = 15.47), and carbonyl groups were titrated using 0.1 M $NaOC_2H_5$ dissolved in ethanol (Table 5).

Table 5. Concentration (meq/g) of surface functional groups calculated using Boehm titration method

Sorbent	pH	–COOH–	–COO–	>C–OH	>C–O	Basic
A2PS	5.4	0.208	0.191	0.203	0.201	0.226
A2PS–H	10.43	0	0	0.076	0.041	0.512
A2PS–O4	4.82	0.309	0.145	0.316	0.209	0.154
A2PS–O8	6.11	0.250	0.163	0.322	0.215	0.257

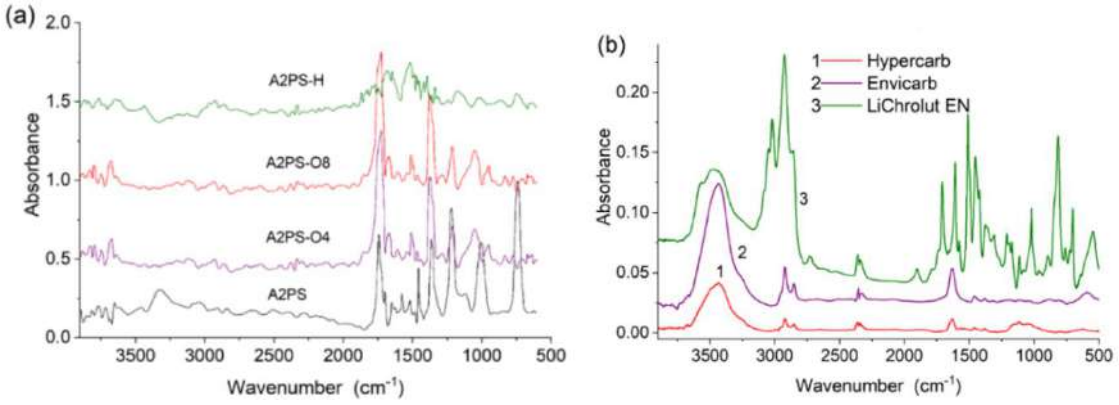

Fig. 13. FTIR spectra of (*a*) AC and (*b*) polymeric and carbon sorbents

The IR spectra of CM were recorded using an FTIR 1725x (Perkin–Elmer) spectrophotometer (Figs. 13–16, Table 6). The measurements were carried out over the 4000–400 cm^{-1} range. Carbon samples were stirred with dry KBr (Merck, spectroscopy grade) (1 : 300 or 1 : 400 w/w) and then pressed to form appropriate tablets. This technique was used since diffuse reflection FTIR spectra of pure carbon samples were less informative.

Table 6. FTIR data for A2PS based CM and possible assignment of functionalities

CM	Wavenumber, cm^{-1}	Structure or Group	*Vibration modes*
A2PS	*1743, 1728, 1711	Carboxyl	$\nu_{C=O}$
	*1364, 1353		ν_{C-O}
	1696	Lactone	$\nu_{C=O}$
	1458	carboxylate ion	$\nu_{CO_2^-}$
	1458 and 3350–3400	Aliphatic	δ_{C-H} and ν_{C-H}
	*1217, 1228, 1204	lactone, ether	ν_{C-O-C}
	*1005, 1026, 997, 972		
	*743, 732	Phenol	arom. substitution
A2PS–O4	*1725, 1760, 1738, 1713	Carboxyl	$\nu_{C=O}$
	*1377, 1369, 1352		ν_{C-O}
	*1216, 1230,	lactone, ether	ν_{C-O-C}
	1050–1010		
A2PS–O8	*1740, 1726, 1712	Carboxyl	$\nu_{C=O}$
	*1366, 1353		ν_{C-O}
	*1217, 1228, 1205	lactone, ether	ν_{C-O-C}
	1020		
	*1217, 1228, 1205	cyclic anhydrides	ν_{C-O-C}
	1020		

Note. *The most intensive signal in broad, split band of peaks.

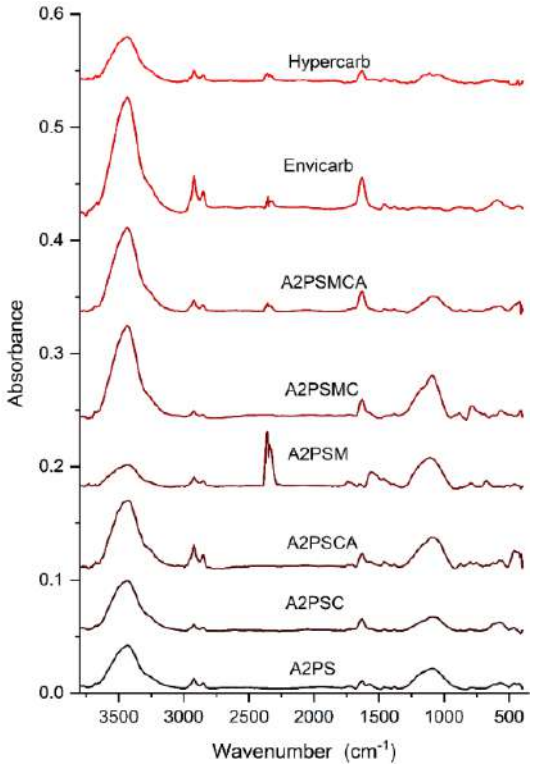

Fig. 14. FTIR spectra of various CM

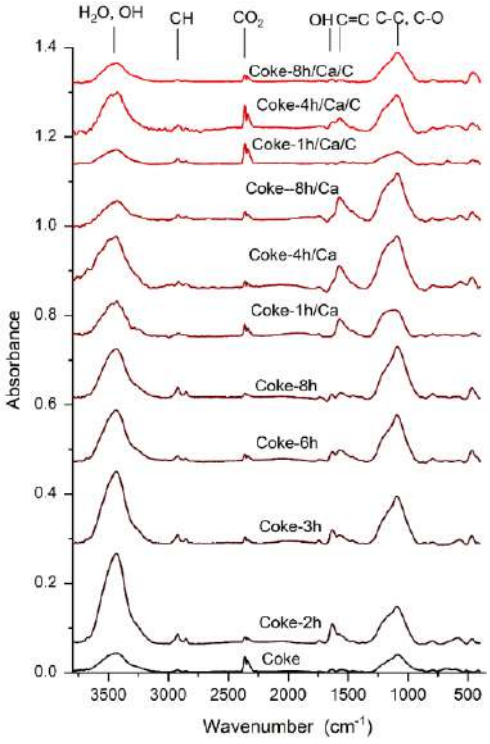

Fig. 15. FTIR spectra of initial and modified cokes

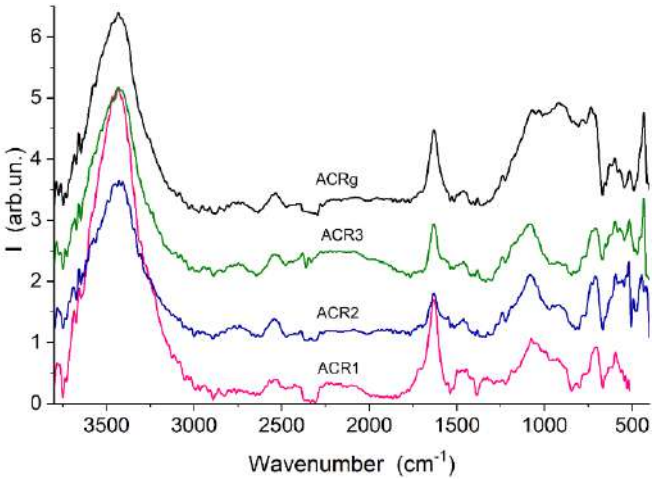

Fig. 16. FTIR spectra of CM produced using resins

INTERFACIAL PHENOMENA UNDER CSE

Both oxidation (by H_2O_2) and reduction (by H_2) of A2PS relatively weakly affect the textural characteristics (Table 1, Figs. 8a and 9a), but these treatments cause certain changes in the amounts of O-containing surface functionalities (Tables 5 and 6, Fig. 13). Unexpectedly, the CSE are sensitive to these structural changes of the carbon surface (Fig. 17). It is possible that these changes also affect the k_{GT} constant value in Eq. (21) that could depend on the surface nature through the σ_{sl} value. However, the effect of surface modification could rather appear in a thin adsorption layer of water or other sorbates. There is another effect linked to changes in location of water in pores of different sizes (i.e., under different CSE). The amount of unfrozen (at $T < 273$ K) water bound to more hydrophobic A2PS–H is ca. 40% (half is SBW) of the total water amount, but for A2PS–O8, practically all water is bound and unfrozen at $T < 273$ K and about 80% of this water is SBW (Fig. 17*a*). This difference could not be explained by only changes in the carbon surface chemistry. An increase in CSE for more strongly oxidized A2PS–O8 could be explained by the location of a larger amount of water in narrower pores than that for other samples. Pure carbon sheets are rather hydrophobic, and the energy of interaction of water with the hydrophobic carbon sheets is twice as small as that upon interactions with hydroxyl functionalities [67]. However, an increase in water amounts could cause its penetration into narrower pores (vide infra). There is an additional effect of changes in the porosity of CM upon freezing of water located in pores because of an increase in the volume of ice in comparison to liquid water [68] (note that the ^{1}H NMR measurements were always performed upon heating from a minimal temperature to avoid water supercooling; therefore, this effect could lead to certain textural changes of treated CM). Therefore, the amount of unfrozen ($T < 273$ K) water bound to A2PS–O8 is larger than the V_p value (Table 1). A portion of this excess water (it's half of 100–150 mg/g) could be bound to the external surface of carbon particles, but another half is located in pores. The latter should correspond to a certain increase in the carbon porosity, and similar effects were observed previously due to freezing of water located in pores of different adsorbents [67]. For hydrophobic A2PS, a significant amount of water (about 60%) remains out of pores and this unbound water is frozen at 273 K, but for A2PS–O8, all water is bound and unfrozen at $T < 273$ K. For all A2PS-based AC, a certain amount of water remains unfrozen even at $T < 200$ K due to the presence of narrow nanopores at $x < 0.5$ nm (Fig. 8a). Thus, there are several expected effects on bound water and other sorbates caused by oxidation/reduction of A2PS such as possible changes in sorption and SPE due to changes in the carbon texture and water (and other probes) location in pores of different sizes affected by changes in the texture due to freezing of water in pores. The chemical shifts of proton resonance (δ_H) for different compounds sorbed (from a saturated vapor phase at 293 K for 2 h) onto unmodified and modified A2PS (Table 7) show that the difference

$\Delta\delta_H = \delta_H - \delta_{H,0}$ for bound molecules (δ_H) concerning the bulk liquids ($\delta_{H,0}$) can be considered as a certain measure of CSE on bound sorbates. The $\Delta\delta_H$ values depend strongly on the sorbate type and location in pores of different sizes and shapes.

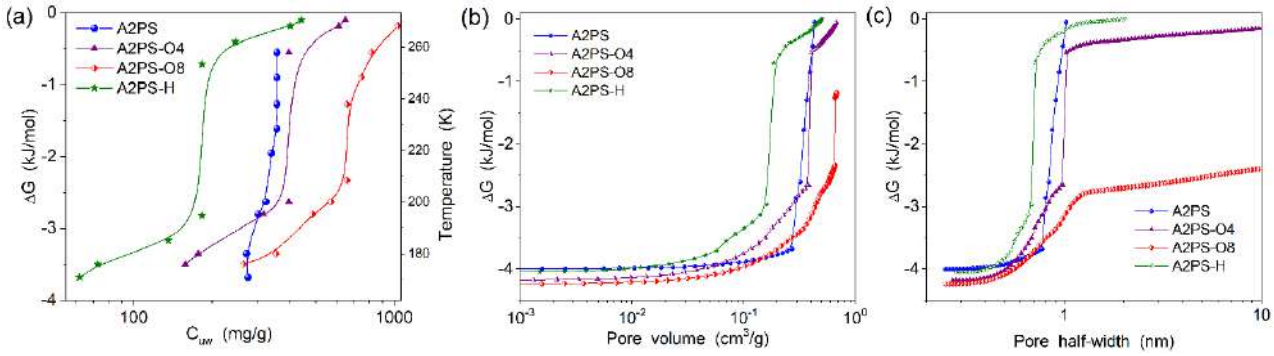

Fig. 17. Relationship between changes in the Gibbs free energy of bound water (h = 1 g/g) and (*a*) amounts of unfrozen water bound to A2PS-based CM and temperature, (*b*) volume, and (c) sizes of pores infilled by unfrozen water

Table 7. Changes in the chemical shifts (ppm) for molecules sorbed onto A2PS-based CM

Adsorbent	Water		Benzene		Acetone		Methane		DMSO	
	δ_{260}	$\Delta\delta_H$	δ_{260}	$\Delta\delta_H$	δ_{260}	$\Delta\delta_H$	δ_{260}	$\Delta\delta_H$	δ_{260}	$\Delta\delta_H$
A2PS	0.2	–4.3	–1.6	–8.9	–6.0	–8.2	–6.0	–5.0	3.0	0.5
A2PS-H	–4.4	–8.9	–2.0	–9.3	–5.3	–7.5	–	–	2.4	–0.1
A2PS-O4	–2.8	–7.3	0.2	–7.0	–4.7	–6.9	–6.0	–5.0	–	–
A2PS-O8	0.7	–3.8	0.0	–7.3	–5.3	–7.5	–5.5	–4.5	2.8	0.3

Note. For methane, its solution in chloroform was utilized; δ_{260} is δ_H for sorbed compounds at 260 K; $\Delta\delta_H < 0$ corresponds to upfield shift, and $\Delta\delta_H > 0$ corresponds to downfield shift.

Table 8. Characteristics of water bound to A2PS-based CM in frozen aqueous suspensions

Adsorbent	$-\Delta G_{max}$ (kJ/mol)	C_{uw}^{max} (g/g)	C_{uw}^{np} (g/g)	γ (mJ/m^2)
A2PS	4.2	0.38	0.38	58
A2PS–H	4.1	0.51	0.19	33
A2PS–O4	4.2	0.70	0.40	63
A2PS–O8	4.3	1.11	0.65	112

The maximal effect (upfield shift) is observed for benzene bound to A2PS–H ($\Delta\delta_H$ = –9.3 ppm) because planar benzene molecules can effectively penetrate into narrow hydrophobic nanopores, where the π-electron clouds at basal carbon planes provide maximal shielding effects. The δ_H value changes for water, acetone, and methane are lower ($\Delta\delta_H$ is from –4.0 ppm to –8.2 ppm) due to the effects of molecular polarity (affecting location of molecules in pores with and without polar functionalities) and shape of molecules, causing their location in broader pores for larger ones. For DMSO (largest 3D molecule among the studied ones), $\Delta\delta_H$ is close to zero, which can be caused by the location of the DMSO molecules in broader pores (mesopores) with minimal CSE and shielding effects. The $\Delta\delta_H$ values for various sorbates are differently affected by the A2PS modification. Stronger relative changes are observed for bound water, since the treatment of A2PS with hydrogen results in enhanced upfield shift (–4.3 ppm for A2PS and –8.9 ppm for A2PS–H). Oxidation of A2PS by H_2O_2 results in a decrease in $\Delta\delta_H$, and for A2PS–O8, it becomes close to that for A2PS. For benzene, in contrast to water, the $\Delta\delta_H$ values for A2PS–O are lower than those for A2PS. However, for other sorbates, the A2PS surface modifications result in relatively weak effects on related changes in $\Delta\delta_H$. These effects could be partially explained by changes in the location of sorbates in different pores; i.e., due to changes in both CSE and shielding effects.

For ^{1}H NMR signals of molecules bound in carbon pores, upfield shifts are typical due to the effects of π-electron clouds at planar carbon sheets and area of local magnetic anisotropy in the surrounding space. The maximal shielding effect is observed near the vertical axes of the π-electron systems (basal plane), and a deshielding effect could be observed only near the longitude axes at the sheet edges, where O-containg functionalities are located [67]. For graphitic structures, the shielding effect is observed in whole space inside the contour of the ring currents, causing a certain magnetic field around the basal planes. The molecules are under relatively strong shielding effects by π-electrons, whose value is correlated to the upfield shift for such probes as benzene. For more complex non-planar carbon nanoclusters (e.g., in pores of completely amorphous AC), the magnitude of the shielding effect depends on the resulting magnetic field of relatively small neighboring carbon sheet fragments. Great shielding effects (up to −18 ppm) were observed for graphitized nanoporous CM [67] with molecules bound in slitshaped nanopores under simultaneous effects from two relatively large graphite-like sheets.

Water molecules could be bound in slitshaped pores between nearly planar carbon sheets that resulting in significant upfield shifts (Table 7). However, water molecules can also form strong hydrogen bonds with polar O–containing functionalities (mainly located at the sheet edges), there proton deshielding could be observed. For A2PS–H, contribution of water molecules located in slitshaped pores grows since a number of O–containing functionalities as centres of water clusterization decreases at the sheet edges. Therefore, the upfield shift is observed. The A2PS oxidation leads to an increase in the contribution of water molecules bonded to polar surface functionalities located at the edges of carbon sheets at the entrances into shitshaped nanopores. Therefore, the upfield shift decreases (Table 7). Methane molecules are bound in pores by dispersion non-specific attraction interactions, and can be located in nanopores between basal planes or weakly bound to polar functionalities at the sheet edges. The maximum negative value of $\Delta\delta_H$ for methane is –5 ppm, which is smaller (by the module) than that of water bound to some AC (Table 7). This may be due to 3D shape of methane molecules that restricts their penetration into the narrowest nanopores. However, the assumption that plane carbon sheets forming nanopores provide the upfield shift for any bound molecule suggests that a major fraction of adsorbed methane is located in nanopores, and for A2PS and A2PS-O8, the effect is stronger than that for water. For benzene, the negative value of $\Delta\delta_H$ is maximal (Table 7) that may be caused by interactions between π-electron clouds of benzene and two basal planes in narrow slitshaped nanopores. Acetone molecules possessing electron-donor properties could be located inside nanopores and at their entrance with O-containing functionalities. However, the surface modification of A2PS practically does not affect the relative amounts of acetone bound in nanopores or interacting with polar functionalities, as the range of $\Delta\delta_H$ changes is ca. 1 ppm. However, the $\Delta\delta_H$ values for acetone are close to that for benzene. In contrast to other sorbates, DMSO molecules possessing strong electron-donor properties is poorly sorbed in narrow nanopores, therefore, the CSE on DMSO chemical shift is small (Table 7). The DMSO molecules could mainly interact with hydroxyl, carbonyl, and carboxyl groups located in narrow mesopores or on the outer surface of the particles. For a fixed hydration degree h = 1 g/g of A2PS CM, the curves of ΔG vs. C_{uw} and T (Fig. 17*a*) show that a portion of unfrozen water remains nearly constant over a certain ΔG range. This effect can be caused by water location in nanopores under strong CSE. The changes in the Gibbs free energy of water bound in nanopores depend weakly on temperature since bound water remains unfrozen in a certain temperature range (Fig. 17*b*). However, the changes in the Gibbs free energy of water slightly differ in narrow (x = 0.25–0.5 nm, pure nanopores) and broader (at x = 0.6–1.0 nm, supernanopores) nanopores (Fig. 17*c*). As a whole, bound water can be frozen in pores if its Gibbs free energy corresponds to that of ice at a certain temperature. If such a temperature has not been reached, water freezing is not observed, and unfrozen water concentration remains practically constant with changing temperature

(Fig. 17). A curve portion of ΔG vs. C_{uw} at the left side of a vertical line (Fig. 17*a*) corresponds to water bound in nanopores (lower freezing temperature is characteristic for SBW); and one at the right is associated with water located in broader pores (mesopores or on the outer surfaces of particles) and corresponding to WBW/UBW (Fig. 17) characterized by higher freezing temperature. As shown above, the ^{1}H NMR spectroscopy can be used to determine a set of characteristics related to the interfacial and temperature behaviors of bound water and other sorbates [67]. The amounts of unfrozen bound water (C_{uw}, total C_{uw}^{max} and located in nanopores C_{uw}^{np}) in the frozen aqueous suspensions of A2PS-based CM, changes in the Gibbs free energy (ΔG), and free surface energy of sorbents (γ) can be estimated (Table 8) from the low-temperature ^{1}H NMR spectra of bound water. These characteristics show that the interaction of A2PS with water strongly grows after oxidation and decreases after reduction by H_2 that is well observed from the amounts of water located in nanopores and changes in the free surface energy.

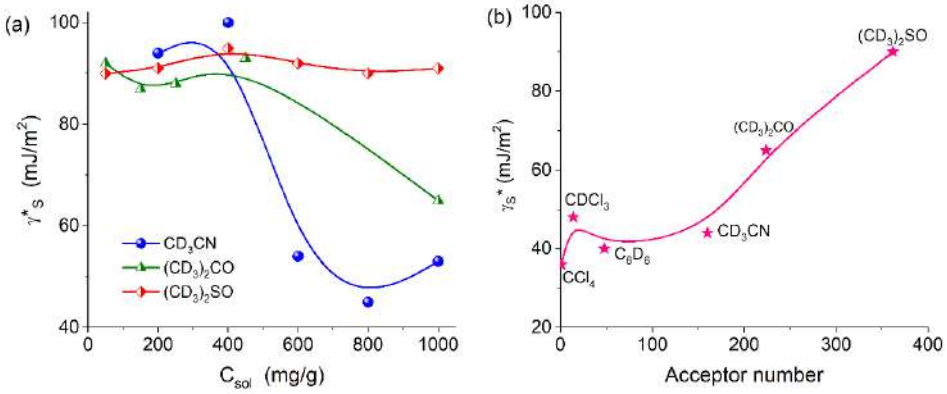

Fig. 18. Changes in the free surface energy of water (calculated with Eq. (24)) bound to AC Norit (*a*) with addition of different amounts of organic solvents miscible with water (CE under CSE), and (*b*) γ_S^* *vs.* the acceptor number of organic solvents (C_{sol} = 1 g/g)

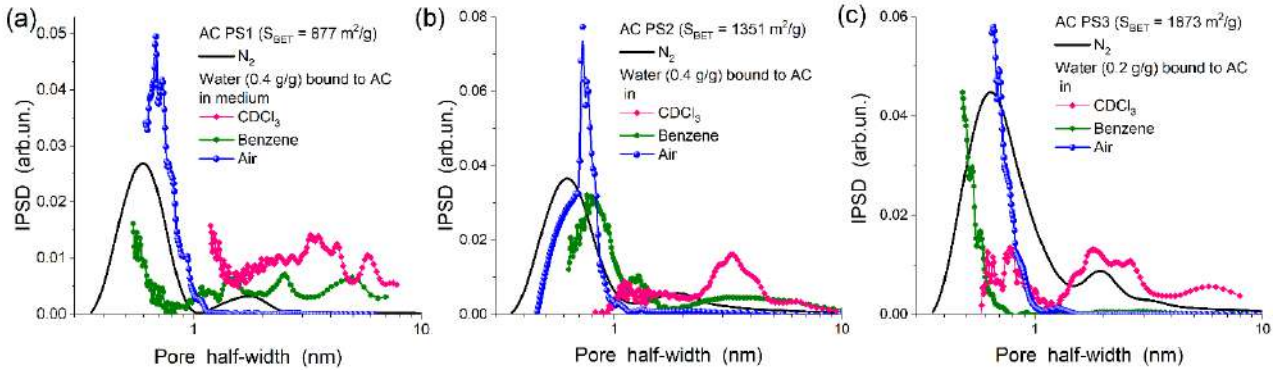

Fig. 19. Effects of co-solvents immiscible with water on unfrozen water location in different pores of three AC (prepared from plum stones) being in different media: $CDCl_3$ can more strongly displace bound water into broader pores of AC than benzene does; additionally, both solvents can displace a fraction of water into narrower pores (*c*)

The free surface energy γ and total content of unfrozen water C_{uw}^{max} decrease for A2PS–H (Table 8) in comparison to A2PS–O. This agrees with other data (Fig. 13*a*, Table 6) showing a decrease in the surface content of O-containing functionalities forming strong hydrogen bonds with bound molecules. Therefore, for A2PS–H, the amount of water bound in hydrophobic nanopores decreases (C_{uw}^{np}). This effect can be explained by the lower accessibility of hydrophobic nanopores for water molecules. For oxidized CM (A2PS–O4, A2PS–O8), an increase in the bound water amounts (both total and located in nanopores) is observed in comparison to both A2PS and A2PS–H due to polar functionalities forming strong hydrogen bonds with water

molecules in nano/mesopores and on the outer surfaces of the carbon particles. Thus, the textural characteristics of CM prepared from plum stones change only slightly (Fig. 8, Table 1) on oxidation with H_2O_2 at 523 K and 623 K for 6 h (steam phase) or reduction with H_2 at 1073 K for 8 h (gaseous phase). However, these modifications lead to an increase in energetic nonuniformity of the carbon surfaces that differently affect the adsorption of nitrogen, water, and organics (see also Figs. 18–21).

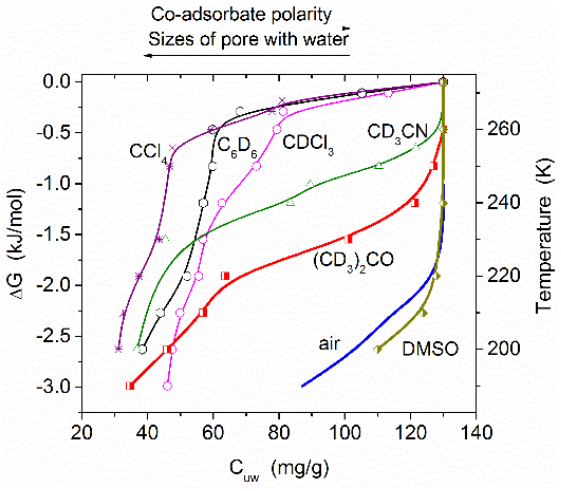

Fig. 20. CSE/CE on water/organic solvents bound to Norit R 0.8 Extra

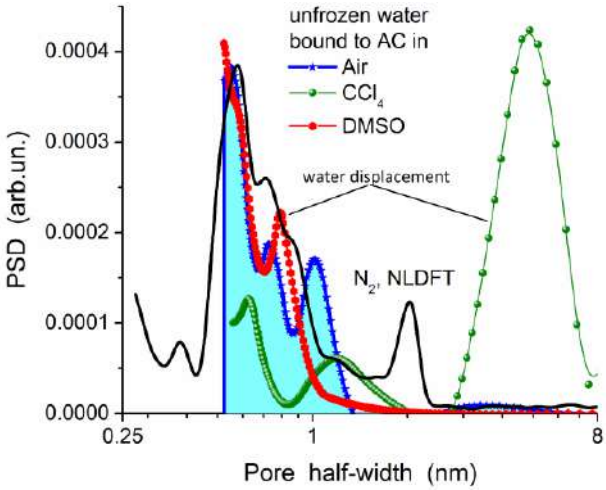

Fig. 21. CSE/CE on cryoporometry results compared to PSD based on nitrogen adsorption for Norit R 0.8 Extra (normalized)

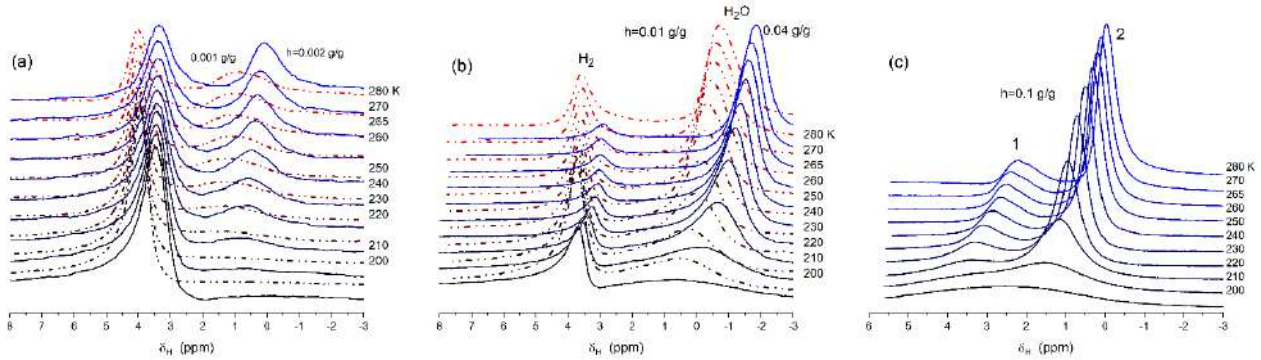

Fig. 22. Low-temperature ^{1}H NMR spectra of water and hydrogen bound to activated carbon C–86 possessing maximal SSA from studied CM (see Tables 1–3, and 10–13) at different hydration h = 0.001–0.1 g/g

The CSE could change the colligative properties (*i.e.*, cryoscopic effects) of solutions located in pores because pore-confined liquids become poorer solvents with reduced activity, molecular mobility, and diffusivity [67–70]. There is an additional effect for a mixture of immiscible or poorly miscible liquids confined in pores, since their repulsion interactions should lead to a diminution of their contact area to reduce the Gibbs free energy of the whole system. These interfacial phenomena could be analyzed using mixtures of organic solvents with water (Figs. 18–20) bound to nano/mesoporous AC Norit R 0.8 Extra (Figs. 8 and 9, Table 1) and other AC. To enhance the observed effects, the amounts of bound water should be smaller than the pore volume. Therefore, for all Norit samples studied, the total amount of bound water was constant h = 0.13 g per gram of dry carbon (Figs. 18–20). This water amount corresponds to approximately 16% of the pore volume; *i.e.*, one can assume that only a part of nanopores (which gives *ca*. 69% of the total pore volume) is filled by water sorbed alone. Dependences of ^{1}H NMR signal intensity of unfrozen bound water and changes in the Gibbs free energy on the amount of unfrozen water C_{uw} were studied for carbon in air or with added organic solvents (Figs. 18–20). The maximal

amounts of co-solvents (1 g of organics + 0.13 g of water per gram of carbon) correspond to the volume similar to V_p (≈ 0.8 cm^3/g) of dry Norit even for CCl_4 (fills 0.67 cm^3 per gram of carbon at C_{sol} = 1 g/g) and CCl_3D (0.63 cm^3 per gram of carbon). However, even for the latter, the total volume of adsorbed water (h = 0.13 g/g) and added solvent is close to V_p. Some solvents ($CDCl_3$, CCl_4, and C_6D_6) are practically immiscible with water, but others (CD_3CN, $(CD_3)_2CO$, and $(CD_3)_2SO$) can form aqueous solutions of any concentration in the bulk. The CE could be absent for the first set of nonpolar solvents (Fig. 20) and decreased for the second set due to CSE (Fig. 18). The ΔG *vs.* C_{uw} curve for the carbon hydrated in air (h = 0.13 g/g) with no addition of organic solvents has a vertical portion (Fig. 20) in the temperature range of 230–273 K. Its appearance is caused by the CSE resulting in water freezing in carbon nanopores only at a significant lowering of temperature at T < 230 K (Fig. 20). This water is strongly bound since ΔG < –1.5 kJ/mol. As a whole, the interfacial behavior of water bound to AC depends on the amounts of added organic solvents (water-soluble) and their kind (Fig. 18). The ΔG *vs.* C_{uw} curve shape significantly changes for water/organics if a solvent is immiscible with water, *i.e.*, its molecules do not form strong hydrogen bonds with water molecules, and the absolute magnitude of the Gibbs free energy of their solvation is relatively small. For similar solvent pairs (water + nonpolar organics), the cryoscopic effect is practically absent in contrast to CSE. One can see curve portions with small changes in ΔG over a relatively large C_{uw} range (Figs. 18 and 20) that can be due to SBW transformation into WBW due to displacement of water by organics into larger pores (Fig. 21) [67]. Similar results were observed for other sorbents [67, 69, 70]. Transform SBW → WBW can be explained by the displacement of a portion (its value dependent on a solvent type and content) of water molecules (clusters or droplets) by organics (stronger interacting with nonpolar basal planes of CM than water) from nanopores and narrow mesopores into larger pores (Fig. 21, CCl_4 medium). However, a portion of SBW remains in nanopores with the presence of nonpolar solvents (Figs. 20 and 21). The amount of this water is between 15% and 46% of h depending on a solvent type. This effect can be caused by the steric effect (observed for larger molecules in narrower pores) and nonuniformity of the carbon surfaces, since different O-containing functionalities are located at the periphery of carbon sheets (on their edges) at the entrances into nanopores or in nanopores as lattice defects of the planes [67]. Water clusters bound to such hydrophilic sites correspond to SBW and its displacement by nonpolar organic molecules is difficult, since the interaction energy of nonpolar molecules with polar sites can be lower than that for water molecules. Additionally, there is a difference in the molecular sizes of water and other solvents. Note that only water and benzene molecules are plain among studied probes, and this is important, as carbon nanopores are mainly slitshaped. That results in different accessibility of narrow nanopores for different molecules, and smaller water molecules can remain in these nanopores inaccessible for larger molecules. However, a significant fraction of water could be displaced into broader pores (Fig. 21, CCl_4 medium). For polar solvents, *e.g.,* DMSO, a similar displacement could be absent (Figs. 18 and 21, DMSO medium). This could be explained by well solubility of water in DMSO and *vice versa,* and significant CE effect for water/DMSO under CSE (Fig. 18). However, CE under CSE could be weaker than in the bulk liquids [67–70]. Thus, solvents insoluble in water can displace water bound to AC into broader or narrower pores (Figs. 19 and 21). Different treatments (suspending¸ drying, freezing by liquid nitrogen, deashing, oxidation by H_2O_2, reduction by H_2, and some combinations of these methods) of AC Norit R 0.8 Extra result mainly in changes in nanopores and narrow mesopores at the pore half-width x < 2 nm (Figs. 8*e* and 9*e*, Table 1). However, these changes can strongly change the temperature behavior of bound water and solvent mixtures (Figs. 20 and 21). The interfacial and temperature behaviors of bound water could be changed upon co-sorption not only with organic solvents but also with light gases such as hydrogen (Fig. 22) and methane [67–70]. These effects are well shown for AC C–86 possessing maximal SSA (S_{BET} = 3463 m^2/g) among all studied CM and significant porosity (V_p = 2.32 cm^3/g) (Tables 1 and 2). There is an unexpected effect since with increasing amount of

water bound to C–86, its signal demonstrates a certain upfield shift. This increased shielding effect could be explained by the penetration of water molecules into narrower pores (with stronger π-electrons effects) with increasing water content. With increasing content of bound water, the amount of adsorbed hydrogen decreases (because water occupies narrow pores appropriated for hydrogen adsorption), but shielding effect grows for hydrogen too (as well as for methane [67–70]).

Thus, localization of both water and hydrogen in pores of different sizes changes with increasing water amounts diminishing hydrogen adsorption. There is an additional effect caused by freezing of pore-confined water because of disjoining pressure of ice having a greater volume than that of liquid water [68], and the ^{1}H NMR measurements were carried out on heating of samples precooled to a minimal temperature. Since the amount of water is small in comparison to the volume of nanopores of C–86 (Table 2, V_{nano}), all sorbed water is located only in nanopores, similar to that for AC Norit (Figs. 18–21). Freezing of sorbed water in narrow nanopores could lead to an increase in carbon porosity by ice (this effect could be irreversible [67]).

This effect grows with increasing amount of water that resulting in enhancement of the shielding effect for water and hydrogen located in narrow pores with increasing water content (Fig. 22). However, an increase in the amounts of water located in narrow pores causes a decrease in the amount of adsorbed hydrogen despite changes in its location in narrower pores and the upfield shift observed. The morphology of AC such as C–86 corresponds rather to amorphous structure. Therefore, in AC, the carbon sheet fragments of a planar shape (forming nanopores) are rather small (from one to several nanometers). Therefore, the shielding effects for sorbates located in narrow pores of AC (Fig. 22) are weaker than that observed for graphitized CM (Fig. 23). The difference in the δ_H values for water located in carbon pores could be significant and depends strongly on the particulate morphology and surface chemistry of CM. Note that water bound to MWCNT and fullerite, which do not have narrow slitshaped pores between large planar carbon sheets in contrast to graphitized carbon, is characterized by significant downfield shifts in contrast to graphitized carbon (Fig. 23).

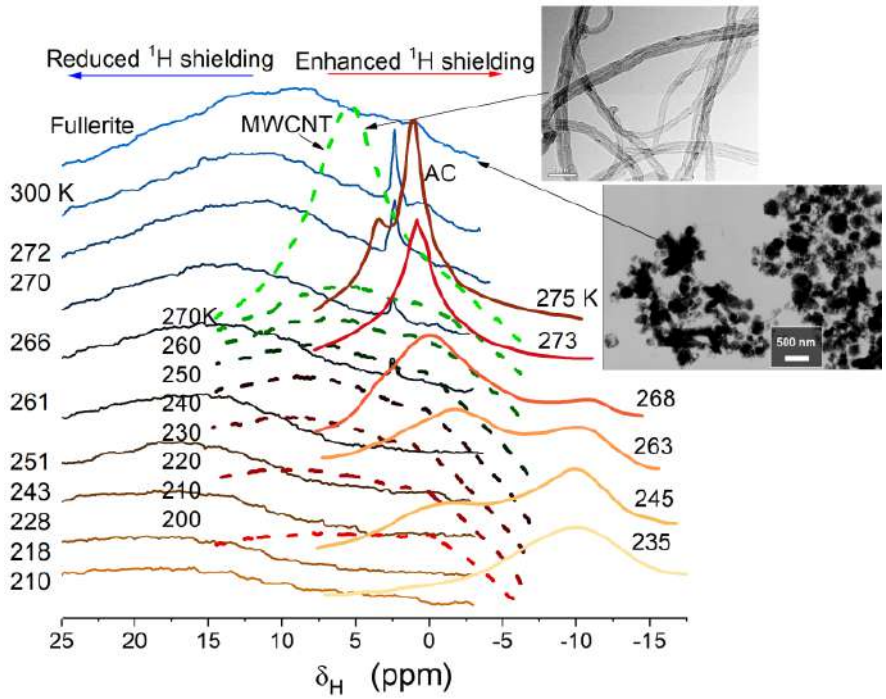

Fig. 23. Low-temperature ^{1}H NMR spectra of water bound to graphitized AC, MWCNT, and fullerite showing CSE affected by the topology and structure of CM, resulting in very different shielding effects from strong upfield shifts (graphitized AC) to strong downfield shifts (fullerite)

It is of interest to compare the temperature behavior of water bound to AC and polymeric sorbent possessing similar textural characteristics. On the NMR measurements, the predominantly hydrophobic character of LiChrolut EN caused incomplete filling of pores by water at hydration h = 2 g/g since the amounts of bound water corresponded to V_w = 0.73 cm^3/g (estimated from the amount of unfrozen water (C_{uw}) at 273 K) which was smaller than V_p = 0.83 cm^3/g but larger than that on the water vapor adsorption (30.44 mmol/g or 0.548 cm^3/g assuming that the density of adsorbed water ρ_0 = 1 g/cm^3) at $p/p_0 \approx 1$. The sorbent is composed of main two structures with cross–linked $[–CH–CH_2–Ph–CH–CH_2–]_n$ (DVB) and linear $[Ph(CH_2CH_3)–CH–CH_2–]_m$ (EVB) chains and includes oxygen–containing groups at the end of the chains (because on free–radical polymerization of PSD, DVB, *etc.* activated by peroxides, growth of the chain occurs from the opposite end to peroxide); *i.e.*, the number of polar active sites in LiChrolut EN is relatively low. Therefore, dispersive interactions of water with the pore wall surface are predominant, similar to that for carbon sorbents, which are characterized by much higher ordering of condensed polyaromatic rings in basal planes than LiChrolut EN that resulting in the upfield shift much smaller than that observed for CM (Fig. 24).

The ^{1}H NMR spectra of water (h = 2 g/g) are characterized by two signals at $T > 273$ K (δ_H = 5 and 4.5 ppm) and a single signal at $T < 273$ K with a slight downfield shift with lowering temperature (Fig. 24*a*). Consequently, the shielding effect of π–electrons of aromatic rings (observed, *e.g.*, in nanopores of carbon sorbents (Fig. 24b)) on water adsorbed in narrow pores is very weak because of orientation disordering of neighboring aromatic rings, which do not form the condensed system as in carbon sorbents.

The signal at δ_H = 5 ppm can be attributed to water located outside of pores (the amount of water is greater than the pore volume) because it is frozen at 273 K. The second signal can be assigned to strongly associated water (SAW), which includes SBW and WBW fractions. In the case of partial filling (approximately 30% V_p) of pores, the water state changes (Fig. 24*b*) in comparison to that on nearly completely infilling (~90%) of pores (Fig. 24*a*). An increase in the chemical shift δ_H is observed with decreasing temperature. Moreover, at 210 K, the δ_H value is equal to 6.9 ppm close to the limiting value (7 ppm) for ice. This can be due to formation of ordered ice crystallites in pores with hydrophobic polymer walls. Notice that all water on 30% filling of pores is SBW at $\Delta G < –2$ kJ/mol and is located only in pores.

Added polar DMSO (20 wt.% with respect to the weight of dry polymer sample) (Fig. 24*c*) or weakly polar $CHCl_3$ (30 wt.%) (Fig. 24*d*) weakly influences the δ_H value of adsorbed water. This is due to the location of water and organic phases in different pores, with a very low contact area between the two immiscible liquids. For chloroform poorly water–soluble, this effect is typical and, therefore, can be expected. However, for DMSO well water–soluble, it would be possible to expect the formation of a homogeneous mixture with adsorbed water (the sample after addition of DMSO was shaken and equilibrated before the measurements) at an intermediate δ_H value between 3 ppm (water dissolved in DMSO) and 5 ppm (SAW alone). However, only SAW is observed for this mixture (Fig. 24*c*). Similar effects were observed for the water/organic mixtures adsorbed on carbon and oxide sorbents. In the presence of $CHCl_3$ (Fig. 24*c*) a portion of water transforms from SAW into weakly associated water (WAW at $\delta_H < 2$ ppm). If the chloroform amount is larger than the pore volume that a significant portion of water becomes WAW, and a certain amount of water corresponds to WBW because it is frozen at temperatures close to 273 K (Fig. 24*e*).

This occurs because chloroform can displace a portion of water from narrow pores, and similar effects were observed for other sorbents because of several reasons: (i) decrease in contact area of practically immiscible liquids; (ii) weakly polar chloroform provides stronger dispersive interaction with hydrophobic pore walls than polar water molecules; (iii) small water clusters (WAW) remain in pores at O–containing sites. In the ^{1}H NMR spectra, besides the signal of SAW ($\delta_H \approx 5$ ppm), whose intensity decreases with decreasing temperature, and WAW signal is observed at $\delta_H \approx 1.3$ ppm. The intensity of the latter depends weakly on temperature. A relatively complex

shape of the ^{1}H NMR spectra of WAW can be due to (i) different values of the magnetic susceptibility of sorbates locating in pores of various sizes and (ii) the orientation effects of benzene rings (*i.e.*, local currents of π–electrons) in pores.

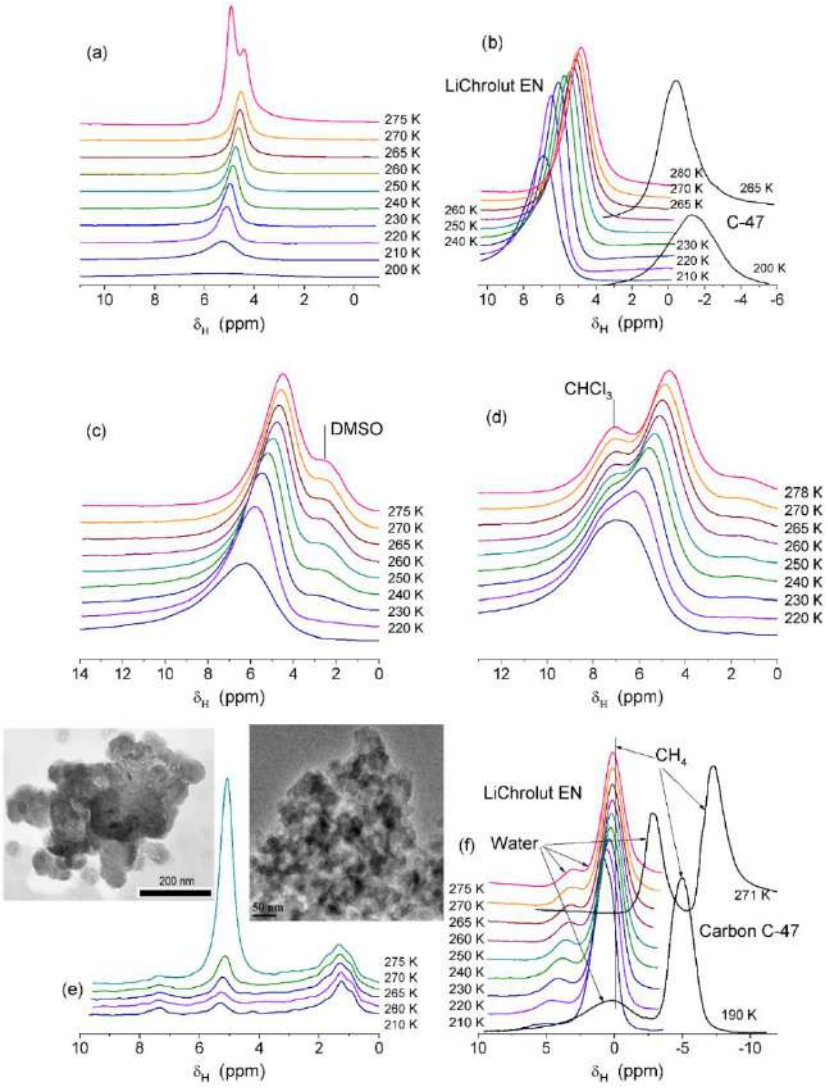

Fig. 24. ^{1}H NMR spectra of water adsorbed on LiChrolut EN sorbent at hydration h = (*a*) 2 and (*b*) 0.25 g/g and co–adsorption of water (pre–adsorbed at h = (*c*, *d*, *f*) 0.25 and (e) 0.175 g/g) and organics (*c*) 20 wt.% of DMSO (half DMSO–d_6); (*d*) 30 wt.% of $CHCl_3$; (*e*) in the $CDCl_3$ medium; and (*f*) 10 wt.% of methane, hydrated activated carbon sorbent C–47 at h = 4.71 g/g (*b*) and $h \approx 0.1$ g/g and adsorbed CH_4 (*f*) recorded at different temperatures (insert: TEM images of (left) LiChrolut EN, scale bar 200 nm, and (right) activated carbon, scale bar 50 nm)

On co–adsorption of water and methane, the ^{1}H NMR spectra strongly change (Fig. 24*b*, *f*) because of the contribution of methane and possible changes in the location and state of bound water. The signal intensity of SAW water decreases, and WAW appears. A residual quantity of SAW corresponds to not more than 25% of the initial quantity. The adsorption of methane is relatively high (up to 10 wt.%) because of a significant contribution of nanopores (incompletely filled by water) of a complicated shape in LiChrolut EN sorbent. The signals of WAW and methane overlap, but at T < 220 K, a clearly visible shoulder related to the methane signal appears at $\delta_H \approx 0$ ppm. On co–adsorption of water and methane, transition of water from the SAW into WAW is thermodynamically preferable because water and methane can form the hydrate system stabilized in narrow pores of the sorbent. Probably, the main reasons responsible for the formation

of such structures are the topological characteristics of polymer pores and the chemical structure of the walls with a low content of polar adsorption sites. The shielding effects of π–electrons of disordered aromatic structures on adsorbed water/methane mixture are much smaller for LiChrolut EN than that of ordered condensed polyaromatic systems in AC C–47 (Fig. 24*f*), since for the sorbents $|\Delta\delta_H|$ > 5–7 ppm, which grows with temperature. The associativity of water molecules depends on the presence of a co-adsorbate. For instance, adsorbed water alone can be assigned to SAW (Fig. 24*a*) because δ_H > 4 ppm over the total temperature range. When the amount of adsorbed water corresponds to approximately 30% of the pore volume, co–adsorption of water and weakly polar chloroform causes the appearance of WAW.

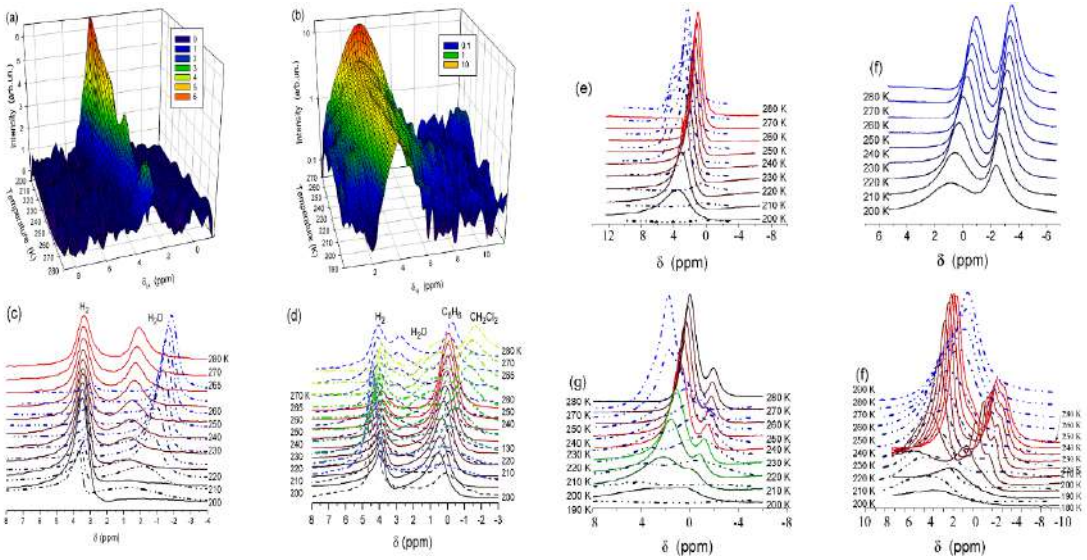

Fig. 25. ^{1}H NMR spectra of hydrogen bound to nanoporous silicalite (a) dry and (b) hydrated (*h*=0.02 g/g) without upfield shift; hydrogen and water co–sorbed onto C–86 at (c) *h*=0.002 g/g (solid lines) and 0.04 g/g (dotted–dashed lines); (d) with the presence of benzene (0.03 g/g) (solid lines), benzene (0.0075 g/g) and water (0.001 g/g) (dashed), and water (0.001 g/g) and CH_2Cl_2 (0.0085 g/g) (dotted–dashed); water (h=0.1 g/g) sorbed on C–47 in mixtures with (e) CD_3CN at 0.1 g/g (solid lines) and 2 g/g (dotted–dashed); (f) $(CH_3)_2CO$ (0.1 g/g); (g) $(CD_3)_2SO$ at 0.1 g/g (solid lines) and 2 g/g (dotted–dashed); and (h) $(CH_3)_2SO$ at 0.1 g/g (solid lines) and 2 g/g (dotted–dashed lines)

Competitive sorption of water, light gases, and organic liquids is strongly affected by the sorbent characteristics, content of sorbates, and temperatures (Fig. 25). For hydrogen and methane, pre–sorbed water effects could be textural (changes in effective porosity with increased contribution of narrower pores appropriate for adsorption of H_2 (Fig. 25*a, b*) and CH_4), trapping, and hydrate formation. The latter is less possible than the first two effects because maximal pressure could be provided in nanopores where the hydrate cells could not be formed due to steric effects. Even in the case of AC with high contribution of nanopores, great SSA and V_p, bound water can positively affect the hydrogen adsorption, but increasing water content results in a diminution of hydrogen adsorption (Fig. 25*c*). Not only bound water can affect the adsorption of light gases, but also other liquids with relatively small molecules (*e.g.*, C_6H_6 and CH_2Cl_2) (Fig. 25*d*). Co–sorption of organics and water can be used for more complete control of the adsorption of light gases (Fig. 25*d*) because competitive sorption of water and organics (Fig. 25*e–h*) results in certain changes in effective texture of sorbents that become better for light gases adsorption. Bound solvents located in narrower pores possess lower activity than those located in broader pores or in the bulk. This is due to strong interactions of molecules with sorbents that result in decreased mobility of molecules, changes in their organization in smaller clusters due to spatial restrictions.

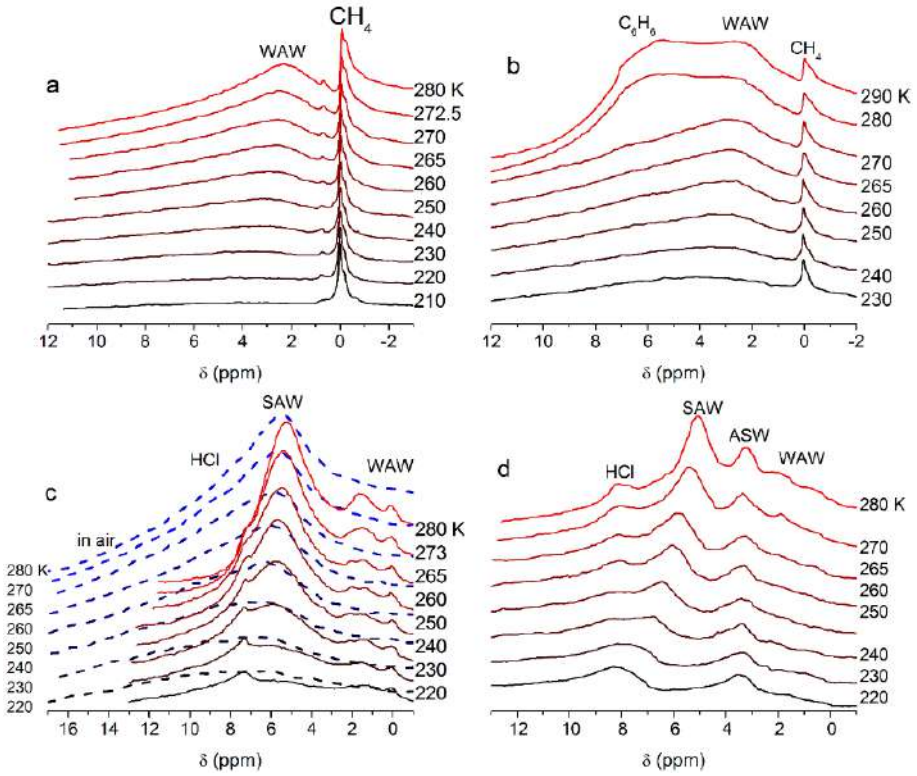

Fig. 26. ^{1}H NMR spectra of water bound to MLGO at hydration h = (*a*, *b*) 0.1, (*c*) 0.3 and (*d*) 0.5 g/g with co–adsorbed (*a*, *b*) methane (from reservoir at pressure of 1.1 bar), (*b*) + 1 g/g benzene; (*c*) 0.1 g/g HCl in air (dashed lines) or $CDCl_3$(solid lines) dispersion medium; and (*d*) 0.2 HCl (in $CDCl_3$+DMSO medium)

The formation of solvation shells in narrower pores is less likely than in broader ones. The spectral characteristics of water bound to MLGO did not change in the methane atmosphere (Fig. 26*a*) because the CH_4 adsorption was low (< 1 wt. %) since the volume of nanopores in MLGO is small. The spectra of co–adsorbed water and benzene (Fig. 26*b*) include an intensive broad signal of benzene (melting point 278.7 K) at T > 270 K. Consequently, its freezing temperature is only slightly decreased versus the bulk solvent. This is due to weak interactions of benzene molecules with the strongly oxidized surface of MLGO. The spectra of the adsorbed HCl solution depend on both the co–adsorbate content and the type of dispersion medium (Fig. 26*c*, *d*). An increase in the quantity of water and HCl and replacement of air by chloroform alone or in a mixture with DMSO leads to the appearance of a signal at 9 ppm, which is characteristic of a concentrated HCl solution. The downfield shift is observed with decreasing temperature due to two effects: (i) concentrating HCl solution in SAW, and (ii) stronger interactions of layers located close to the surface with the O–functionalities. In the $CDCl_3$ medium, the spectra change (Fig. 26*c*, *d*). The main signal demonstrates an upfield shift (by 0.5 ppm). The signal of the concentrated HCl solution ($\delta_H \approx$ 9 ppm) is not observed, but a signal of WAW appears at $\delta_H \approx$ 1.5 ppm. An increase in the dispersion medium polarity by the addition of 10% of DMSO results in more complex spectra (Fig. 26d), including 4–5 signals. For instance, the signal of water associated with DMSO molecules (ASW) at $\delta_H \approx$ 3.5 ppm does not change the position in contrast to a signal of SAW at $\delta_H \approx$ 5 ppm at 280 K (with a small portion of dissolved HCl) and 7 ppm at 240 K. The latter is due to changes in the content of HCl in SAW at decreasing temperature because of acid concentrating effect. Therefore, only one signal ($\delta_H \approx$ 8.5 ppm) of HCl/SAW is observed at 220 K. In contrast to SAW, WAW cannot dissolve HCl. Therefore, the signal position of WAW at $\delta_H \approx$ 1.5 ppm does not change with decreasing temperature.

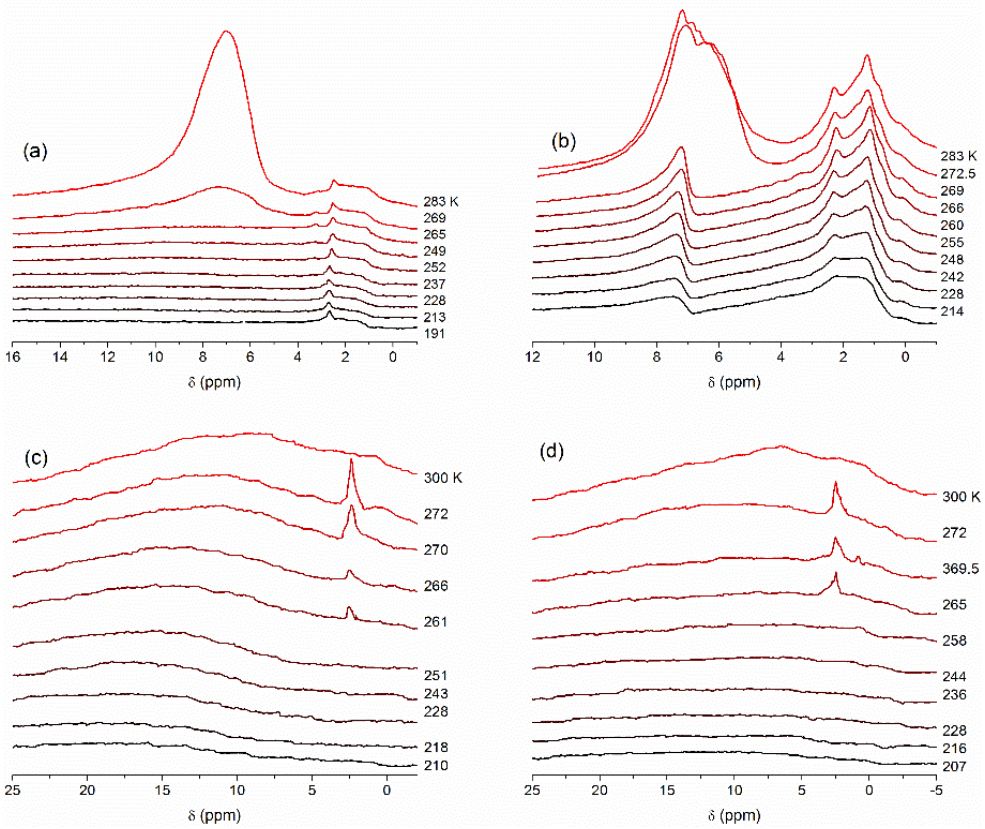

Fig. 27. ^{1}H NMR spectra of water and organics bound to fullerite at a constant hydration degree h = 20 mg/g of initial sample in (*a*) methane atmosphere, (*b*) $CDCl_3$, and preheated fullerite (at 500 K for 1 h) in (*c*) air and (*d*) $CDCl_3$

If water amounts added to CM are low (h = 20 or 50 mg/g) that water weakly interacts with a surface of both fullerite and MWCNT (Table 9, γ_s). Water rather forms relatively large structures and its contact area with the carbon surface is low (Table 9, S_{uw}). The interaction of water with MWCNT strongly grows with increasing h to 200 mg/g (Table 9, γ_s), and the value of S_{uw} grows to 325 m^2/g., *i.e.*, water coves the total surface of the nanotubes. Water molecules penetrate into nanopores (*e.g.*, defects in MWCNT structures and tight contacts between neighboring tubes in their aggregates) since the value of S_{nano} gives the major contribution to S_{uw}. This leads to a significant freezing point depression (Table 9, $<T_m> << 273$ K) because the freezing point depression grows with decreasing size of pores. Water (h = 20 mg/g) bound to fullerite located in the methane atmosphere (Fig. 27) gives two signals at δ_H = 7.5 and 1.5 ppm at 283 K. These signals can be attributed to SAW and WAW. A fraction of SAW (about 10 wt. %) is unfrozen even at 220 K (Fig. 27). The value of δ_H of SAW grows up to 11 ppm (Fig. 28), and the signal half–width is relatively large. This is due to the low mobility of molecules of unfrozen water bound in narrow voids of fullerite. Results of the decomposition of some characteristic ^{1}H NMR spectra of water bound to fullerite and MWCNT are shown in Fig. 28 and Table 10. The large values of δ_H for SAW (Fig. 29), which are much greater than those for water bound to other CM, can be explained by the electron–acceptor properties of fullerite. Note that such a strong deshielding effect is very unusual for CM. For activated carbons, especially for graphitized materials or nanoporous AC, there are strong opposite shielding effects with a great upfield shift. Note that MWCNT demonstrates weaker deshielding and stronger shielding effects than fullerite for protons of bound water.

Fullerite as a vdW molecular crystal is a hydrophobic material, and water cannot be strongly bound to its surface, especially if fullerite contains such residual organics as nonpolar toluene. Therefore, the signal intensity of SAW adsorbed to fullerite strongly decreases at

T < 273 K, *i.e.,* this weakly bound water becomes frozen with little lowering of temperature (Figs. 29 and 30). However, there is a small amount of bound WAW, which corresponds to SBW. Its signal intensity depends weakly on temperature. The small WAW structures (*e.g.*, 2D clusters) can be located in the narrowest voids between fullerene molecules in fullerite crystallites. There are several narrow ^{1}H NMR signals on the background of the broad signal of WAW that can be attributed to the CH_3 and CH_2 groups in residual (~1 wt.%) toluene and diethyl ether (δ_H = 2.5, 1.25, and 0.95 ppm) used as solvents upon extraction of fullerene. Note that the signal of methane at 0 ppm is practically absent, *i.e.*, there is no methane adsorbed to weakly hydrated fullerite located in the methane atmosphere. This is due to the blocking of entrances into narrow voids by residual toluene and water molecules, because SAW clusters are larger than the voids between buckyballs in the fullerite lattice.

Table 9. Structural characteristics of unfrozen water bound fullerite and MWCNT

Sample	S_{uw} (m^2/g)	S_{nano} (m^2/g)	S_{meso} (m^2/g)	V_{nano} (cm^3/g)	V_{meso} (cm^3/g)	γ_S (J/g)
Fullerite	2.8	2.1	0.7	0.001	0.007	0.4
Fullerite	13.9	11.7	2.2	0.004	0.015	1.2
Fullerite	11.0	10.3	0.7	0.004	0.008	0.9
MWCNT	4	0	3.9	0	0.027	0.3
MWCNT	325.4	290.4	35.0	0.105	0.095	21.3
MWCNT	133.6	40.0	93.6	0.016	1.135	20.1

Continued Table 9

Sample	$<T_m>$ (K)	ΔG_s (kJ/mol)	h (g/g)	$C_{uw,max}$ (mg/g)	Medium	Preparation conditions
Fullerite	251.3	–2.83	0.02	9.5	CH_4	Initial
Fullerite	242.4	–3.29	0.02	19.5	Air	Preheated
Fullerite	238.9	–3.32	0.02	16.4	$CDCl_3$	Preheated
MWCNT	268.3	–0.3	0.05	33.6	CH_4	Preheated
MWCNT	220.3	–3.24	0.20	199.9	CH_4	Preheated
MWCNT	268.2	–3.18	6.67	2665	Water	Initial

Note. S_{uw} is the specific surface area in contact with unfrozen water ($C_{uw,max}$), S_{nano}, V_{nano} and S_{meso}, V_{meso} the surface area and volume of water structures at radius R < 1 nm (nano) and 1 nm < R < 25 nm (meso), respectively, ΔG_s is the changes in the Gibbs free energy of the first adsorbed layer.

For initial fullerite (weakly hydrated at h = 20 mg/g), a band of toluene at approximately 7.2 ppm for the H atoms attached to the aromatic rings is not observed (Fig. 27). This is due to the very low mobility of the toluene molecules bound in the voids of fullerite particles as an inclusion compound (*i.e.,* toluene and diethyl ethers are strongly bound intercalants). However, in the $CDCl_3$ medium, the spectra change and include a signal of toluene at $\delta_H \approx 7.2$ ppm. Signal intensity of methyl and methylene groups of toluene and diethyl ether, as well as WAW, grows. This is due to the displacement of organic and water molecules by the $CDCl_3$ molecules from narrow voids in dense particles of fullerite into broader voids or onto the outer surface of crystallites, where the mobility of the molecules grows. To reduce the effects of residual organics (toluene, diethyl ether) on water penetration into narrow voids, the fullerite sample was preheated at 500 K for 1 h, and then water was added (h = 20 mg/g) (Figs. 27–30). This pretreatment of the fullerite results in enhanced penetration of water molecules into narrow voids (Fig. 31). The signal of SAW becomes much broader than that for the initial sample; *i.e.,* the molecular mobility of bound water strongly decreases. The amount of SBW grows since the amount of water unfrozen at low temperatures grows. The value of δ_H of SAW becomes very large, especially for a sample located in air. After the addition of $CDCl_3$, the value of δ_H decreases close to that observed for the initial sample because of the displacement of a fraction of water by the organic solvent from narrow voids in fullerite.

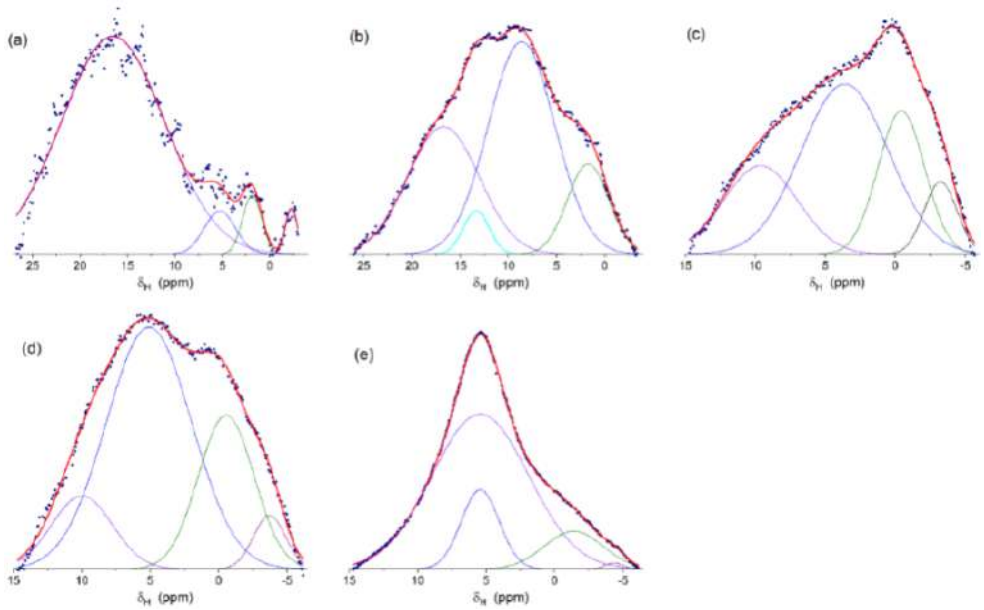

Fig. 28. Decomposition of the ^{1}H NMR spectra of water bound to (a, b) fullerite and (*c*–*e*) MWCNT at h = (*a*, *b*) 20 mg/g and (*c*–*e*) 6.7 g/g recorded at T = (*a*) 210 K, (*b*) 300 K, (*c*) 200 K, (*d*) 260 K, and (*e*) 270 K

Table 10. Results of decomposition of ^{1}H NMR spectra of water bound to fullerite and MWCNT

Sample	T (K)	h (g/g)	δ_1 (ppm)	c_1 (%)	FWHM$_1$ (ppm)	δ_2 (ppm)	c_2 (%)	FWHM$_2$ (ppm)
Fullerite	210	0.02	–2.29	1.90	1.50	1.86	4.53	2.38
Fullerite	300	0.02	1.73	13.21	5.06	8.63	50.41	8.14
MWCNT	200	6.7	–3.23	7.69	2.75	–0.43	20.09	3.92
MWCNT	260	6.7	–3.72	4.80	2.77	–0.56	24.22	4.79
MWCNT	270	6.7	–4.37	0.55	1.55	–1.41	10.84	5.04

Continued Table 10

Sample	T (K)	h (g/g)	δ_3 (ppm)	c_3 (%)	FWHM$_3$ (ppm)	δ_4 (ppm)	c_4 (%)	FWHM$_4$ (ppm)
Fullerite	210	0.02	5.25	5.45	3.87	16.54	88.12	12.88
Fullerite	300	0.02	13.34	4.05	3.19	16.74	32.32	8.74
MWCNT	200	6.7	3.61	49.06	7.33	9.63	21.16	6.25
MWCNT	260	6.7	5.09	58.60	7.36	9.99	12.38	5.22
MWCNT	270	6.7	5.43	14.88	3.26	5.43	73.73	8.30

Note. FWHM is the full width at half maximum.

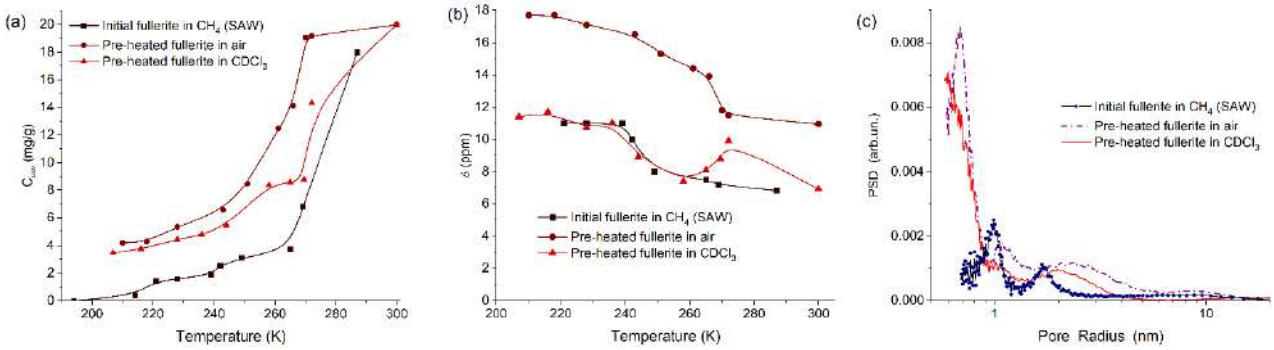

Fig. 29. (*a*) Amounts of unfrozen water at a constant hydration degree h = 20 mg/g of initial fullerite in methane atmosphere (only SAW) and pre–heated fullerite (at 500 K for 1 h) in air and $CDCl_3$ media

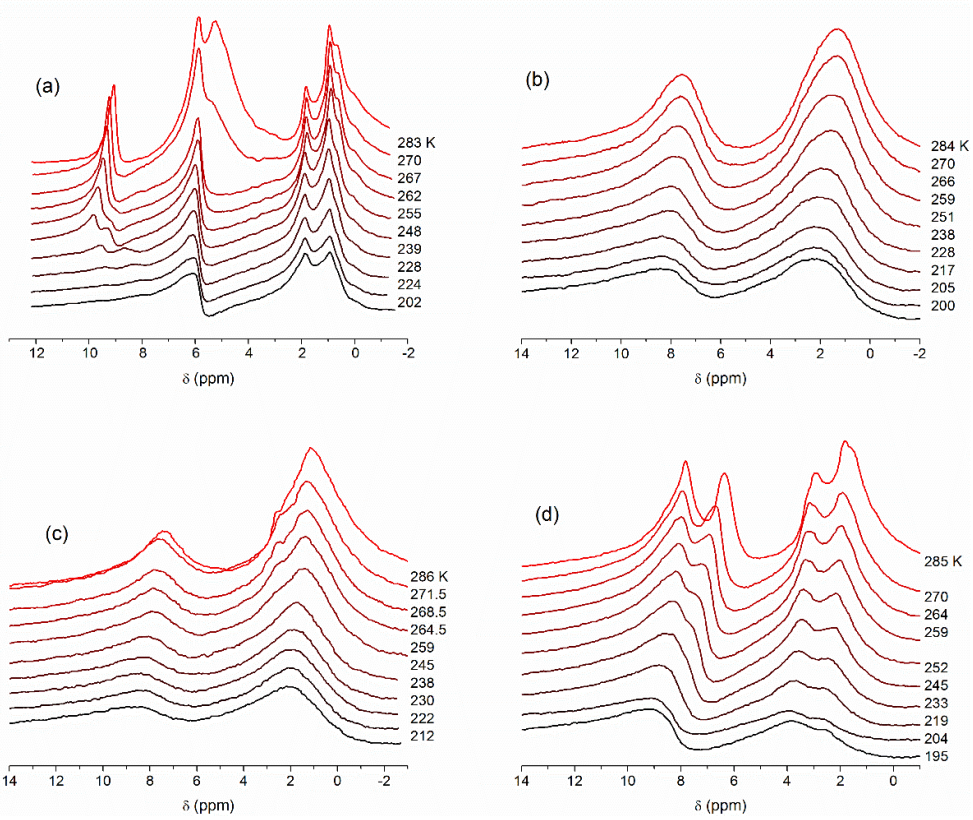

Fig. 30. ^{1}H NMR spectra of water and organics bound to fullerite in the $CDCl_3$ medium with addition of (*a*) TFAA (25% aqueous solution) to initial fullerite at h = 20 mg/g, (*b*) pre–heated fullerite (500 K for 20 min) with addition of 50 mg/g of hydrochloric acid, (*c*) then dried and heated sample at 400 K for 20 min after addition of 20 mg/g of water, and sample (*d*) with addition of DMSO–d_6 ($CDCl_3$/$(CD_3)_2SO$ = 4 : 1)

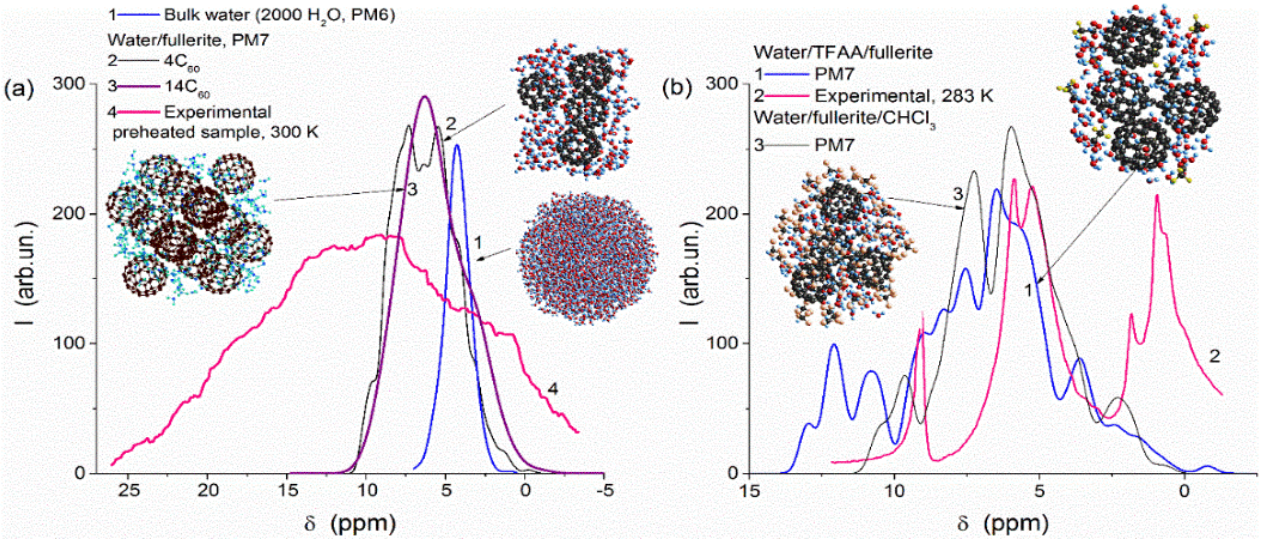

Fig. 31. Calculated and experimental spectra of (*a*) water and (*b*) water with $CHCl_3$ and water/TFAA bound to fullerite

Addition of a F_3CCOOH (TFAA) solution to fullerite results in the appearance of signals at 9–11 ppm (Fig. 30*a*), which can be attributed to the aqueous solution of TFAA with its different concentrations. The values of δ_H of SAW, which is free of dissolved TFAA, are practically the same (in the range of 4–6 ppm) as those observed for a sample without TFAA. In other words, this

SAW can poorly dissolve TFAA due to decreased activity of bound water as a solvent under confined space effects (CSE), *i.e.*, cryoscopy effect (CE) becomes weaker under CSE. To study the effects of residual organics on the adsorption of an acidic solution, fullerite was preheated at 500 K for 20 min, and then 50 mg/g of the aqueous solution of HCl was added to the sample cooled to room temperature. Two signals corresponding to WAW (1.5–2 ppm) and concentrated solution of HCl (8–10 ppm) are observed (Fig. 30*b*). WAW does not dissolve HCl, and the clusters of WAW are separated by $CDCl_3$ medium from clusters of SAW/HCl. This sample with the adsorbed acidic solution was also dried and preheated at 400 K for 20 min, and then 20 mg/g of water was again added (Fig. 30c). Signal of SAW/HCl remains, but its intensity decreases by approximately three times. Addition of DMSO to $CDCl_3$ affects the ^{1}H NMR spectra of the aqueous solution of HCl (Fig. 30*d*). Signals of WAW and SAW/HCl split due to the DMSO effect. One of the reasons of this splitting is the strong interactions of DMSO and water molecules in solvation complexes characterized by $\delta_H \approx 3.5$ ppm. This leads to a downfield shift of the signal of WAW. The content ratio of the structures with SAW and WAW changes with decreasing temperature due to faster freezing of WAW without HCl.

Theoretical calculations (Fig. 31) show that water interacting with the fullerene C_{60} molecules is characterized by broadened ^{1}H NMR signals in comparison with bulk water (Fig. 31*a*, curve 1). These results correspond to the experimental data. However, the experimental spectra are broader (Fig. 31a, comp. curves 2, 3, and 4) due to the lowered mobility of the molecules bound in narrow voids in fullerite. According to the calculations, TFAA has more acidic protons than those observed experimentally (Fig. 31*b*). This is due to the diminution of the activity of bound water as a solvent according to experimental observations; therefore, a fraction of TFAA can be in a molecular state with smaller values of δ_H. The $CHCl_3$ surroundings of hydrated fullerene molecules cause the appearance of WAW (Fig. 31*b*, curve 3, a small peak at 2.4 ppm).

MWCNT aggregates preheated at 400 K and then weakly hydrated can adsorb methane that appears in the ^{1}H NMR spectra as a signal at $\delta_H \approx 0$ ppm (Fig. 32*a*). Signal grows with decreasing temperature due to increased amounts of adsorbed methane. Water at $h = 50$ mg/g pre–adsorbed onto MWCNT located in the methane atmosphere has a signal at $\delta_H = 4.5$ ppm (Fig. 32*b*), which corresponds to SAW. In contrast to adsorbed methane having a very low freezing point, the signal intensity of water decreases with decreasing temperature due to its partial freezing–out. An increase in the value of h to 200 mg/g (Fig. 32*c*) results in the enlargement of the water signal width. Besides SAW, there is WAW at $\delta_H = 1.5$ ppm with a narrow signal width. The signal of WAW decreases with decreasing temperature, but to a lesser extent than SAW. Note that at $h = 200$ mg/g, the signal intensity of methane decreases in comparison to the sample at $h = 50$ mg/g. This effect can be caused by partial blocking of voids by water and ice that grows with decreasing temperature and increasing amount of sorbed water.

MWCNT, as well as fullerite, is a rather hydrophobic material, which, however, can include O–containing surface functionalities formed at structural defects. At a low hydration degree ($h = 50$ mg/g), water represents larger structures than that at increased hydration degree ($h = 200$ mg/g) because water overcoming the barrier of wetting of a surface of MWCNT can penetrate narrow voids in aggregates and slit–shaped defects in MWCNT. The latter is confirmed by the appearance of a water signal characterized by a significant upfield shift at the values of δ_H from 0 to –2 ppm (Fig. 32). Changes in the location of the water clusters with increasing hydration degree explain the reduction of the methane adsorption (Fig. 33) because such light gases as methane can be effectively adsorbed only in narrow pores. Therefore, filling of these narrow pores (voids) by water at $h = 200$ mg/g should result in a decrease in the adsorption of methane. On the other hand, the clusters of unfrozen water and ice change the topology of pores, that can affect subsequent adsorption of methane. Methane molecules can be adsorbed in voids partially filled by WAW or ice that can affect both signal shape and interfacial behavior of bound methane molecules.

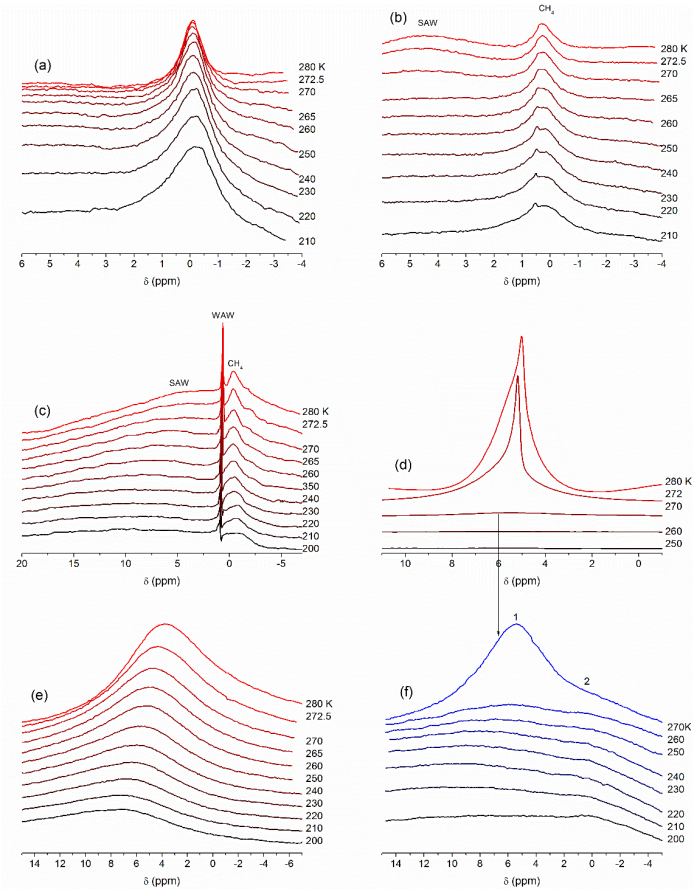

Fig. 32. ^{1}H NMR spectra of adsorbates bound to MWCNT (**a**) methane, (*b*, *c*) water at *h* = (*b*) 50 mg/g or (*c*) 200 mg/g and methane, (*d*,*f*) aqueous medium (*h* = 6.7 g/g), and (*e*) benzene (5.3 g/g)

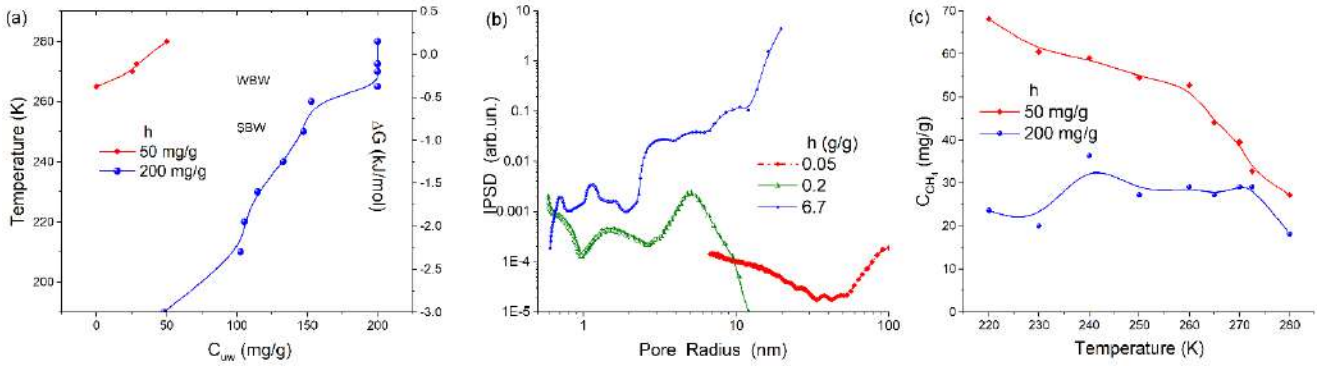

Fig. 33. (*a*) Relationships between the amounts of unfrozen water as a function temperature and changes in the Gibbs free energy of unfrozen water bound in voids of aggregates of MWCNT in CH_4 atmosphere; (*b*) the size distributions of pores (voids) filled by unfrozen water clusters at different values of *h*; and (*c*) temperature dependence of adsorption of methane at *h* = 50 and 200 mg/g

For MWCNT in the aqueous medium at *h* = 6.7 g/g (Fig. 32*d*,*f*), unfrozen water is observed as structures (Fig. 33b) characterized by signals at δ_H = 5 ppm (signal 1) and 0 ppm (signal 2) at 270 K. Intensity of signal 1 strongly decreases with decreasing temperature but the value of δ_H grows. Intensity of signal 2 depends weakly on temperature, as well as the value of δ_H (Fig. 32*f*). In this case, air microbubbles can be remained in aggregates of MWCNT. This results in smaller amounts of SBW (frozen at $T < 260$ K) and smaller values of S_{nano} and V_{nano} (Table 9) at *h* = 6.7 g/g

than those at h = 0.2 g/g. Note that the maximal values of δ_H at h = 0.2 and 6.7 g/g are close to 10 ppm. This tendency of the appearance of water signals with great downfield shifts is similar to that observed for water bound in voids of fullerite. Certain downfield shifts are also observed for unfrozen benzene bound to MWCNT with decreasing temperature (Fig. 32e). These deshielding effects on the protons of adsorbates bound in voids of fullerite (stronger effects) and MWCNT (weaker effects) can be caused by local magnetic anisotropy around strongly bending carbon structures such as fullerene C_{60} molecules (smaller values of the radius of curvature – stronger downfield shifts) or caps of MWCNT (larger values of the radius of curvature – smaller downfield shifts).

The various locations of water bound in voids of different sizes appear upon the adsorption of a small amount of water onto solid polymeric hyaluronic acid with the addition of a small amount (~2 wt.%) of MWCNT (Fig. 34). Water shows broad signals of WAW (signals at 0–2 ppm) with a certain upfield shift with decreasing temperature, and SAW interacting with the acid ($\delta_H \approx 8$ ppm) and demonstrating the downfield shift with decreasing temperature. Thus, WAW rather interacts with MWCNT than with the acid molecules, which should cause a downfield shift for bound water.

After the extraction of fullerenes C_{60} and C_{70} using toluene as a solvent, drying and washing–off by diethyl ether, small amounts (~1 wt.%) of these solvents remain in fullerite particles; however, these molecules can be removed by chloroform. Organics remained in the initial fullerite affect location of bound water, since they prevent penetration of water in narrow voids. After preheating fullerite and removal of organics, water can fill narrow voids (< 1 nm in radius). Water located in these narrow voids is characterized by great unusual downfield shifts up to δ_H = 18 ppm. This strong deshielding effect (Fig. 34) can be caused by local magnetic anisotropy in narrow voids around small buckyballs with a small value of radius of curvature in the molecular crystals. In these voids, the structure of π–electron clouds strongly differs from that observed at a plane carbon sheet in slitshaped pores in graphitized materials, in which strong magnetic shielding effects are observed for protons in bound molecules. Both shielding and deshielding effects are observed for water (Fig. 35) bound in nanopores and around the caps of MWCNT, respectively.

Overall, there are certain common features between water bound in the suspensions of graphite oxide and SLGO and MLGO (Fig. 36a–c) that has δ_H=4–7 ppm at different temperatures.

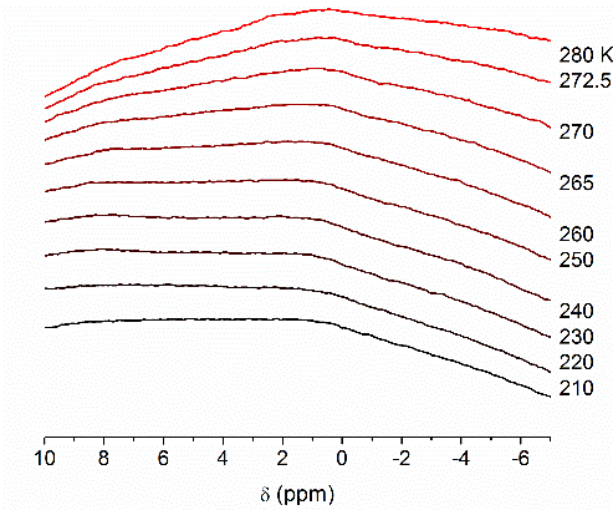

Fig. 34. ^{1}H NMR spectra of water bound to solid hyaluronic acid with addition of 2 wt.% of MWCNT (composite of very high strength) at h = 50 mg/g

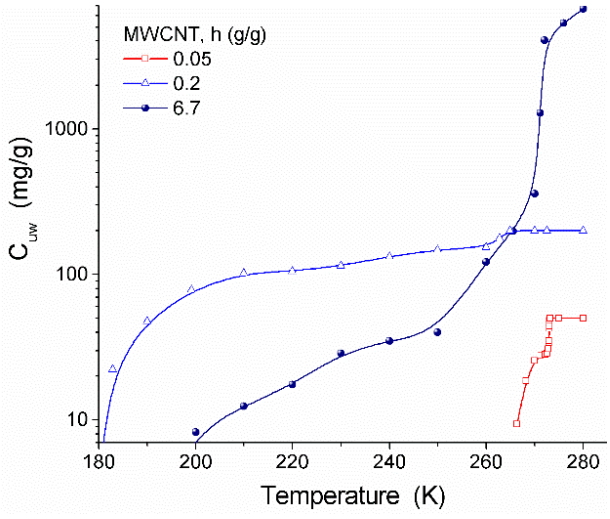

Fig. 35. Amounts of unfrozen water bound to MWCNT *vs*. temperature at different hydration degree

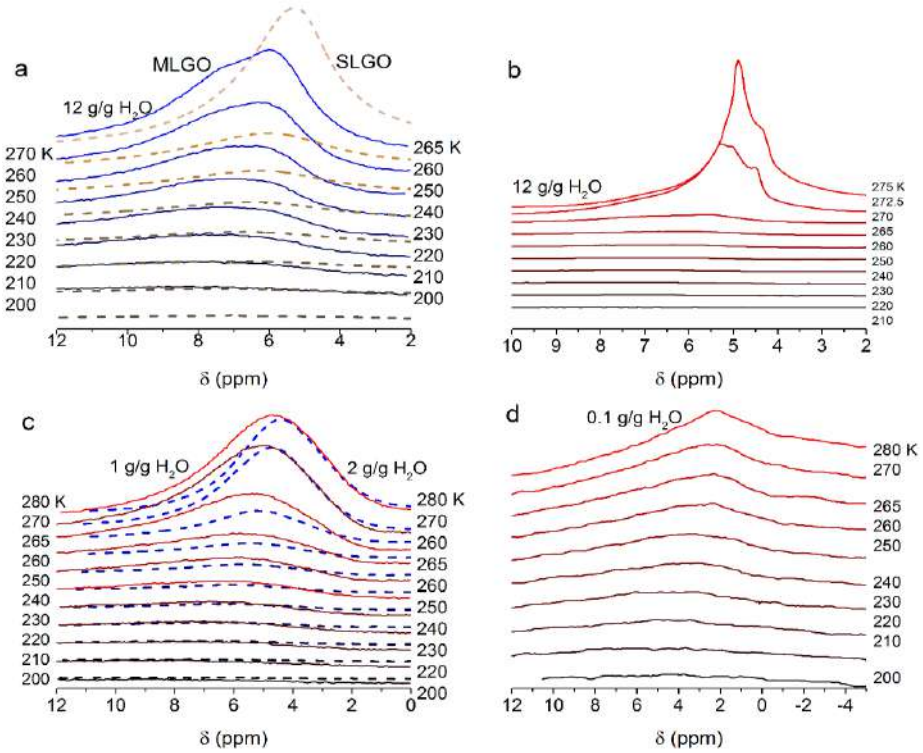

Fig. 36. ^{1}H NMR spectra (recorded at different temperature) of water bound to (*a*) SLGO and (*a–d*) MLGO at different hydration degrees, where h = (a, b) 12, (c) 1 and 2, and (d) 0.1 g/g

Water bound to MWCNT (Figs. 35 and 36), having a very large ratio of length/diameter and much larger values of radius of curvature than fullerene C_{60}, can form SAW and WAW structures in voids between neighboring tubes in their aggregates (broad pores with adsorbed SAW) and in structural defects in MWCNT (narrow pores with adsorbed SAW and WAW). However, the downfield shift for water located around electron–acceptor sites is smaller (by ~5–7 ppm) than that observed for fullerite. For a fraction of WAW, a small upfield shift ($\Delta\delta_H$ = –2 ppm) is also observed that can be explained by the location of water in narrow slitshaped nanopores. Water bound to fullerite or MWCNT can form structures with both weakly and strongly associated molecules. WAW cannot dissolve acids (*e.g.,* HCl, TFAA), but a certain fraction of SAW can dissolve the acids.

Fullerene molecules are densely packed in the FCC lattice of the molecular crystals. Therefore, pre–adsorbed water, even in a small amount, and molecules of toluene and diethyl ether remaining in fullerite can easily block the entrances into pores (voids), and, therefore, methane cannot be adsorbed. In the case of MWCNT, aggregates of tubes are much looser than the aggregates of molecular crystals in fullerite. Therefore, pre–adsorbed water (in a small amount of 50 or 200 mg/g) only weakly affects subsequent adsorption of methane. However, an increase in the amounts of pre–adsorbed water results in a decrease in the adsorption of methane. For the carbon samples in air, changes in the hydration degree of MLGO differ by two orders of magnitude (h = 0.1–12 g/g) and a high hydration of SLGO results in broad ^{1}H NMR spectra of static samples because of the effective and fast (in NMR timescales) exchange between different water structures at both high (1–12 g/g) and low hydration levels (h = 0.1 g/g). However, the peak position shifts towards smaller δ_H values with decreasing hydration because of a decrease in associativity of water, *i.e.,* water becomes more clustered, and the effect of carbon sheets, where voids between them can decrease with decreasing h value. Maximum clustering of water observed at minimal hydration h = 0.1 g/g is characterized by the lowest δ_H values (Fig. 36*d*).

At a low water content, the ^{1}H NMR spectra of CM in a $CDCl_3$ dispersion medium demonstrate a more detailed picture (Fig. 37*a*) than the spectra of samples in air (Fig. 36*d*).

Therein, strongly associated water, SAW (Fig. 37*a*) at δ_H = 5.5 (290 K) and 6 (200 K) ppm, and weakly associated water, WAW, with three signals at δ_H = 0.8, 1.2, and 1.8 ppm, are featured. Typically, SAW is characterized by δ_H = 4–6 ppm, similar to that of bulk water. WAW, as clustered water with an unusual structure, has a lower δ_H = 1–2 ppm, showing that the average number of hydrogen bonds per molecule is lower than in SAW. The signal intensity decreases with lowering temperature due to the freezing of a portion of bound water, and at higher temperatures for SAW than WAW because the contribution of strongly bound water (SBW) is greater in WAW than SAW. The positions of the boundary signals at δ_H = 0 ppm (TMS) and 7.2 ppm (chloroform) of the added standards are practically independent of temperature (Fig. 37a). The shielding effects of π–electrons of carbon sheets in SLGO are weak in comparison with those in activated carbon (AC), which has a very large surface area (S_{BET} = 3463 m^2/g) and high porosity. This is clearly seen when comparing the ^1H NMR spectra for these materials with the difference in position of the SAW peak $\Delta\delta_H \approx -2$ ppm (Fig. 37a). Notice that this behavior of water bound to ACs is characteristic of activated carbon with a broad pore size distribution, whereas for purely nanoporous ACs, the shielding effects are much stronger for adsorbed water at $\Delta\delta_H$ up to –6 ppm.

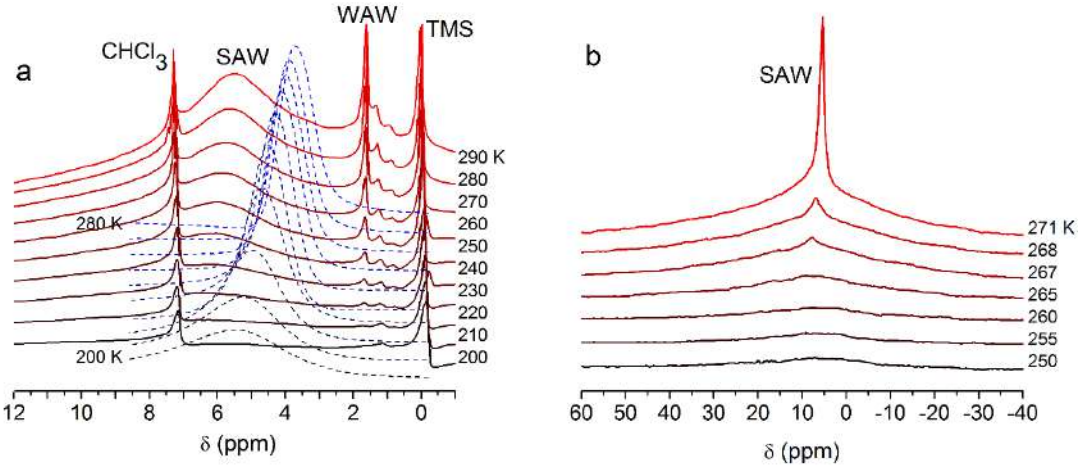

Fig. 37. ^1H NMR spectra of water bound to (a) SLGO at h = 0.16 g/g of water (in $CDCl_3$ medium) (solid lines) and activated carbon (burn–off 86%, S_{BET} = 3463 m^2/g, V_p= 2.04 cm^3/g) at h = 0.1 g/g and 0.4 g/g of $CDCl_3$ (dashed lines), and (b) SLGO at 1.6 wt.% (*i.e.,* h = 61.5 g/g) in the aqueous suspension

Theoretical calculations of a hydrated SLGO cluster and the ^1H NMR spectra of water bound to SLGO and surface OH groups show that a nonuniform structure of the sheet results in clustered adsorption of water (Fig. 38, upper structure). Water is mainly located at the hydrophilic sites of the sheet. However, 2D clusters can be formed over the hydrophobic sp^2–C regions, but these clusters are bound to other clusters that are formed around hydrophilic O–containing functionalities. A portion of the COOH groups located at the edge of the sheet are deprotonated. This results in the appearance of the downfield lines at δ_H = 8–10 ppm for structures such as $H_5O_2^+$. 2D water clusters also give peaks at $\delta_H \leq 2$ ppm (*i.e.*, the H atoms without hydrogen bonds) corresponding to WAW.

In the case of graphite oxide, the carbon sheets can be arranged in multi–layered stacks in contrast to SLGO (typically with 1–3 layers). Therefore, spatial hindrances for the exchange processes between different water clusters, domains, or layers are stronger for graphite oxide particles than for SLGO in the suspensions. In the suspensions, SLGO can be present in the form of single layers or more complex 2D or 3D structures with several or many sheets depending on the pH value, temperature, and dissolved species. In the case of wetted SLGO (h = 0.16 g/g), small 2D water clusters (WAW) can be located at the surface of the sheets around the O–containing functionalities either at the edges or inside the sheet, or between adjacent sheets

(minimal δ_H values). Dry or wetted SLGO sheets can form complex 3D structures. Therefore, small water clusters can form hydrogen bonds with two sheets (WAW with larger δ_H values) in these sheet aggregates. An increase in the pore size and the formation of 3D water clusters within result in the appearance of SAW structures, especially with increasing hydration. Water (h = 0.17 g/g) and methane adsorbed onto SLGO give three signals (Fig. 39*a*) at δ_H = 6–8 ppm (SAW), 1 ppm (WAW), and 0 ppm (CH_4).

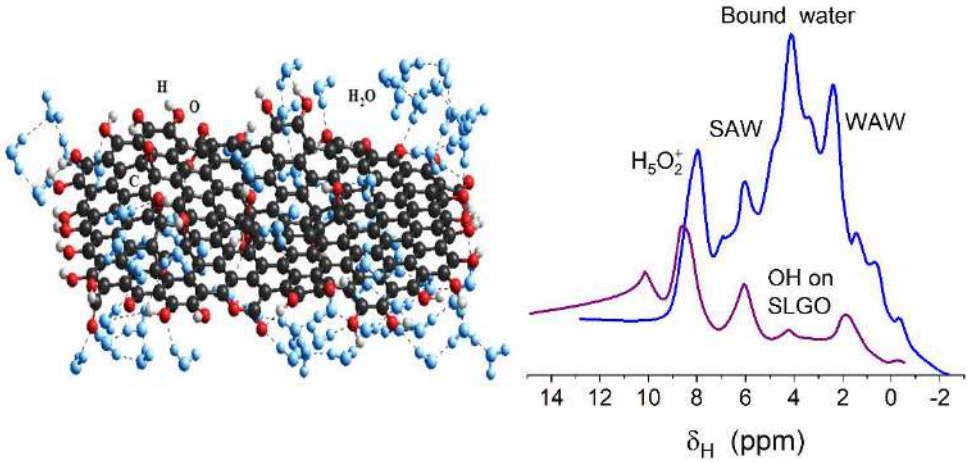

Fig. 38. Theoretical ^{1}H NMR spectra of water (curve 1) and hydroxyl groups (2) attached to the model SLGO sheet (calculated with the correlation function and PM7 atomic charges)

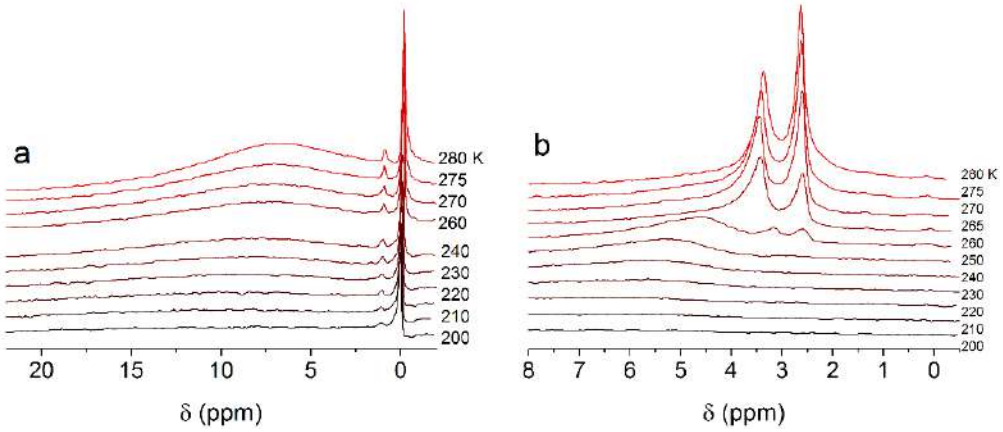

Fig. 39. ^{1}H NMR spectra of (*a*) water and methane bound to SLGO and (*b*) water interacting with SLGO in CCl_4/DMSO–d_6 (1.5/1) medium at h = 0.17 g/g (*a*, *b*)

The methane signal does not depend on temperature, but its intensity slightly grows with increasing temperature, which can be due to the reorganization of water structures in the melting portion of ice and SLGO aggregates. A great δ_H value of SAW is due to its interaction with numerous O–containing functionalities at the SLGO surface (O atoms represent about 10 at % in SLGO). A portion of SAW (distant from a surface) is frozen when lowering the temperature, but other portions interacting with the surface remain unfrozen and are characterized by greater δ_H values. A narrow WAW signal at δ_H = 1 ppm is observed in the presence of methane (or weakly polar $CDCl_3$).

The interfacial behavior of water bound to SLGO differs in a mixture (1.5/1) of nonpolar CCl_4 and polar DMSO–d_6 (Fig. 39*b*). Besides two signals of water (3–3.5 and 4.5–6.0 ppm), an intensive signal of CH_3 groups of $(CH_3)_2SO$ as an admixture in DMSO–d_6 is observed at 2.5 ppm. The CCl_4/DMSO mixture is frozen at $T < 260$ K, which allows the study of the behavior of bound water when the dispersion medium changes its phase state. Complete freezing of the medium occurs at $T \leq 240$ K and water has δ_H = 5–6 ppm. At higher temperatures $T \geq 265$ K water gives a

signal at 3.5 ppm characteristic of certain complexes such as HO–H···O=S$(CD_3)_2$ or HO–H···O=S$(CH_3)_2$. Consequently, a fraction of water transfers into the dissolved state in the liquid organic solvent and loses direct contact with the SLGO surface.

The temperature behavior of the C_{uw} for SLGO (Fig. 40*a*) and MLGO (Fig. 40b) depends on the amount of water present, since the smaller the water content, the larger the slope of the $C_{uw}(T)$ function. This effect can be explained by the freezing of more weakly bound water at higher temperatures (but at $T < 273$ K) than that for more strongly bound water. This phenomenon is described by the Gibbs–Thomson equation for the freezing point depression for liquids confined in narrower pores. Typically, WBW is frozen at 250–260 K, but a portion of SBW (located in nanopores) can be in an unfrozen state even at $T < 200$ K.

The $C_{uw}(T)$ functions were used to calculate the textural characteristics of SLGO and MLGO at different hydration levels (Table 9, Fig. 40) using the cryoporometry method. A decrease in the amounts of water adsorbed or bound to CM results in a strong diminution of the textural characteristics because they correspond to the specific surface area in contact with unfrozen water or the pore volume filled by unfrozen water at $T = 273$ K.

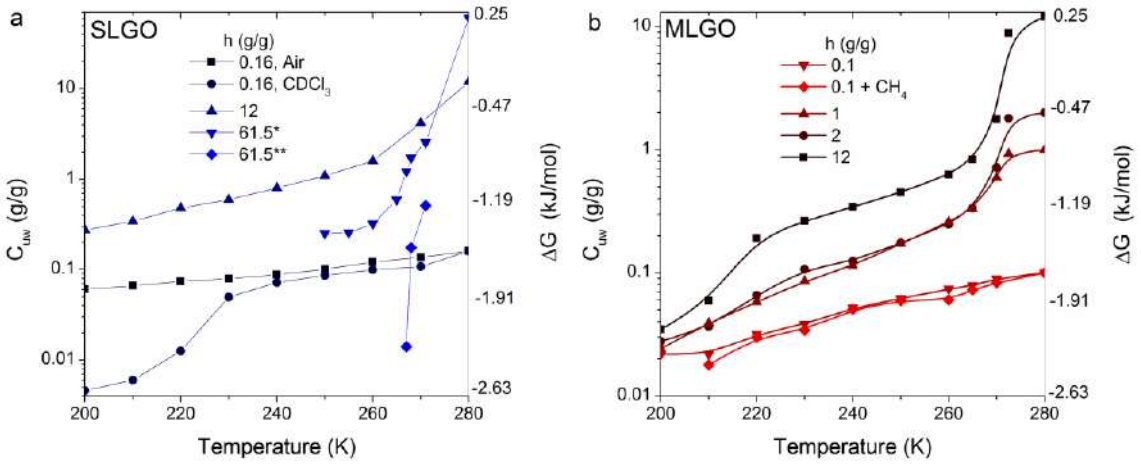

Fig. 40. Temperature dependences of the amounts of unfrozen water ($C_{uw}(T)$) and the relationships between $C_{uw}(T)$ and changes in the Gibbs free energy of water bound to (*a*) SLGO and (b) MLGO at different hydration degrees; (*a*) 61.5* and 61.5** g/g correspond to SAW (▼) and WAW (♦), respectively

The hydrated SLGO samples were frozen to 200 K and then thawed at 5–10 K steps to record the ^{1}H NMR spectra. In the case of the suspension samples ($h = 61.5$ g/g), freezing of bulk water leads to the formation of ice crystallites. The SLGO particles with bound unfrozen water (SBW) are located between the ice crystallites and undergo compressive effects. This leads to the removal of water located between SLGO sheets, bringing them into direct contact with one another, and, therefore, denser agglomerates are formed. This is reflected in the diminution of the specific surface area of the material, which is determined as the area in contact with unfrozen bound water after freezing of the suspension. This effect is practically absent for frozen wetted samples at $h = 12$ g/g because the portion of bulk water (SAW) forming ice crystallites is much lower than that in the suspension, and the dispersion structure can be different. In the case of a low content of water ($h = 0.1$–2 g/g), it cannot cover the total surface of the SLGO or MLGO sheets. Therefore, the maximal S_{uw} values are observed for SLGO or MLGO at $h = 12$ g/g (Table 11), when the coverage of the surface by water is great but insufficient to compress the carbon sheets by the formed ice crystallites strongly enough for a significant decrease in the contact area between interfacial water (unfrozen at $T < 273$ K) and the sheet surfaces. There is an additional effect of the concentration of the dispersion phase on its stability. Diluted suspensions (*e.g.,* at $h = 61.5$ g/g) are much less stable than concentrated suspensions (*e.g.,* at $h = 12$ g/g).

The incremental PSD (Fig. 41*a*) and differential PSD (Fig. 41*b–d*) for SLGO and MLGO are similar. However, the textural characteristics of SLGO have greater values than those of MLGO at the same or similar hydration levels (Table 9–11, Fig. 41) because MLGO has a larger number (n_s) of sheets in the stacks than SLGO. From the maximal S_{uw} values for SLGO or SLG, one can estimate the n_s values being 1–3 for SLGO or SLG and 5–6 for MLGO (assuming that for individual carbon sheets $S \approx 4200$ m^2/g, *i.e.,* a stack with two or three sheets gives $S \approx 2100$ or 1400 m^2/g, respectively).

Table 11. Structural and energetic characteristics of water bound to SLGO or MLGO differently hydrated

h (g/g)	S_{uw} (m^2/g)	S_{nano} (m^2/g)	S_{meso} (m^2/g)	V_{nano} (cm^3/g)	V_{meso} (cm^3/g)	$-\Delta G_S$ (kJ/mol)	C_{uw}^S (g/g)	C_{uw}^W (g/g)	γ_S (J/g)
61.5*	533	250	283	0.110	3.147	2.58	0.2	6.0	61.0
12.0*	1841	1304	536	0.505	3.853	3.13	0.6	4.8	177.5
0.16*	235	223	11	0.075	0.061	3.56	0.16	0.0	15.3
12.0**	787	493	294	0.209	2.814	2.79	0.5	8.31	84.5
2.0**	267	173	94	0.073	0.826	3.33	0.25	1.53	30.0
1.0**	223	149	74	0.064	0.566	3.15	0.25	0.67	25.5
0.1**	97	87	10	0.033	0.056	3.19	0.1	0.0	7.8
SLG[a]	1558 (BET)	1108	449	0.688	1.225	–	–	–	–

Note. *SLGO and **MLGO; [a]N_2 adsorption data for SLG was used to calculate the textural characteristics using DFT method, for SLG, V_{macro}= 0.068 cm^3/g, S_{macro}= 1.6 m^2/g, and the error for the slit–shaped pore model $\Delta w = -0.084$, *i.e.*, 8.4%.

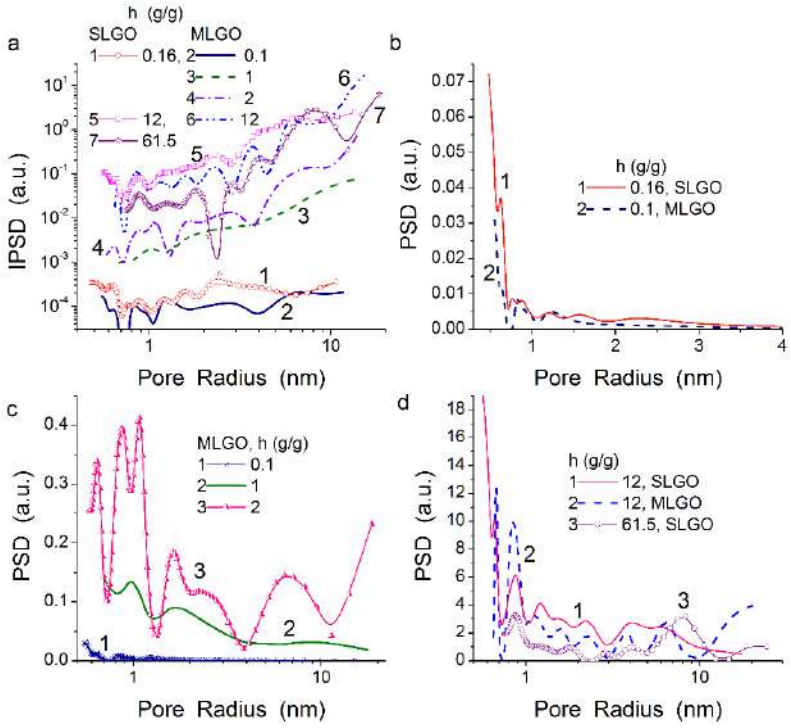

Fig. 41. (*a*) Incremental void (pore) size distribution IPSD and (*b–d*) differential PSD calculated using NMR cryoporometry method for SLGO and MLGO at different hydration degree

Since the S_{uw} value decreases for frozen diluted aqueous SLGO suspension (h = 61.5 g/g, Tables 9–11) and strongly wetted SLGO at h = 12 g/g (providing about 50% filling by water of the empty volume in the SLGO powder), it can be concluded that the agglomeration of the sheets grows in the diluted suspension. These results could be caused by the hydrophobic effect, *i.e.*, the rearrangement of the SLGO stack structure in the diluted suspension to reduce the contact area of hydrophobic sp^2–C regions of the sheets with water, as well as by the cryogelation effect and pressure of ice crystallites. In the wetted sample, which can be considered as a concentrated

suspension at 7.7 wt. % SLGO, a similar rearrangement does not occur since the S_{uw} value is maximal and corresponds to the stacks with only 2–3 single sheets on average. This is in agreement with the n_s value given by the SLGO manufacturer. A large difference in the V_{nano} values but similar V_{meso} values for these samples (Tables 9–11), as well as the position of the IPSD (Fig. 41*a*) and PSD (Fig. 41*d*) for the suspension and the wetted powder, also confirm the agglomeration effects for SLGO sheets in suspension.

Contributions of nanopores and narrow mesopores (R < 7 nm) in SLGO aggregates are greater than those in MLGO aggregates (Fig. 41) because of stronger aggregation of the sheets in MLGO. Therefore, the textural characteristics of the latter are lower than those of SLGO at the same or similar hydration degrees (Tables 9-11) that can influence the results of co–adsorption of water and organics. The IPSD and PSD shapes determined from the adsorption of water for SLGO and MLGO are complex and strongly differ from those for activated or graphitized CM that were determined from the adsorption of water or nitrogen. This is due to the random packing of the sheets in SLGO or MLGO aggregates and their weak bonding, which results in a facile rearrangement of the sheet aggregates depending on the dispersion medium characteristics.

It should be noted that MLGO prepared from natural flake graphite could contain nanoparticles composed of carbon and silica (Fig. 42) that can affect the interfacial phenomena at the surface of MLGO.

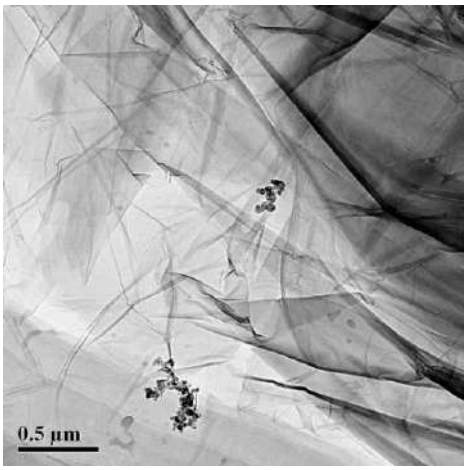

Fig. 42. TEM image of MLGO prepared using natural flake graphite precursor (visible nanoparticles are mainly composed of carbon and silica)

The structural characteristics and organization of aggregates of single and multi–layer graphene oxides strongly depend on the hydration degree, dispersion medium, parameters of solvents, co–adsorbates, and solvent freezing–thawing treatment. The temperature behavior, structure, and location of interfacial water bound to SLGO and MLGO in different dispersion media (air, $CDCl_3$, CCl_4, $CDCl_3$/DMSO) depend on the presence of the co–adsorbates studied (benzene, methane, or HCl). These features were analyzed using low–temperature ^{1}H NMR spectroscopy applied to static samples at 200–280 K to avoid signals from the solid phase (ice and OH groups attached to CM).

The use of the NMR cryoporometry method allowed the determination of the textural characteristics of SLGO and MLGO aggregates depending on the hydration degree and freezing–thawing effects. According to the cryoporometry results, MLGO is characterized by a larger number of sheets in the stacks (5–6 in average) than SLGO (1–2) in wetted powders. SLGO in diluted suspensions, which were frozen and then thawed, exhibited a greater degree of agglomeration, since the specific surface area in contact with bound water decreases more than three times (from 1841 to 533 m^2/g) due to the compression of the carbon sheets in aggregates by ice crystallites during the freezing of the suspension. In the case of strongly wetted SLGO (h = 12 g/g), this effect is much weaker since bulk water is practically absent, but frozen strongly

associated water cannot provide similar compressing effects because of insufficient quantity. The wetted MLGO at hydration h = 12 g/g has the specific surface area 787 m^2/g (~5 sheets in stacks, which is close to the n_s value given by the MLGO manufacturer) with a predominant contribution of nanopores. The S_{uw} values are maximal for SLGO and MLGO at h = 12 g/g since the amount of water is enough to form maximal coverage of the sheets surface, but not sufficient for strong compressing effects by ice crystallites. The results obtained show that the cryoporometry method provides valuable information on the texture of both wetted and suspended graphene oxides and the effects caused by freezing of the samples.

Confined space effects lead to the freezing point depression and can differently affect the colligative properties (CP) of liquid mixtures concerning FPD (*i.e.*, CE). Therefore, for some systems (maximal FPD for bulk non–ideal solutions) with no additivity of CSE and CP:

$$FPD_{CSE} < FPD_{CSE+CP} < FPD_{CP,b} \text{ and } |\Delta G_{CSE+CP}| < |\Delta G_{CSE}|+|\Delta G_{CP,b}|$$

but for some others (minimal FPD for bulk almost ideal solutions) with CSE and CP additivity:

$$FPD_{CP,b} < FPD_{CSE} < FPD_{CSE+CP} \text{ and } |\Delta G_{CP,b}|<|\Delta G_{CSE}|<|\Delta G_{CSE+CP}|$$

This occurs due to several factors:

- changes in the concentrations of different liquids in the mixtures;
- spatial restrictions for the formation of complete solvation shells in narrow pores;
- decrease in the solvation activity of any solvent located in narrow pores;
- stronger decrease in molecular mobility in narrower pores affected by topological nonuniformities of pores and pore walls;
- differentiation and structurization of the liquid phases of the mixtures located in pores;
- clusterization of molecules around strong adsorption sites;
- effects of dispersion media.

As one of the consequences of the obtained results for the mixtures, the corrected cryoporometry equation should be used

$$\Delta T_{f,CSE} - \alpha \Delta T_{f,CP/CSE} = -k/R,$$

where α is the structural factor affected by CSE, $\alpha < 1$ for miscible compounds (*e.g.*, acids, NaOH, DMSO with water) and $\alpha = 0$ for immiscible ones (*e.g.*, water and *n*–decane). Pore size decrease leads to an increase in CSE and a decrease in CP. This approach allows one to study the organization of various mixtures in pores.

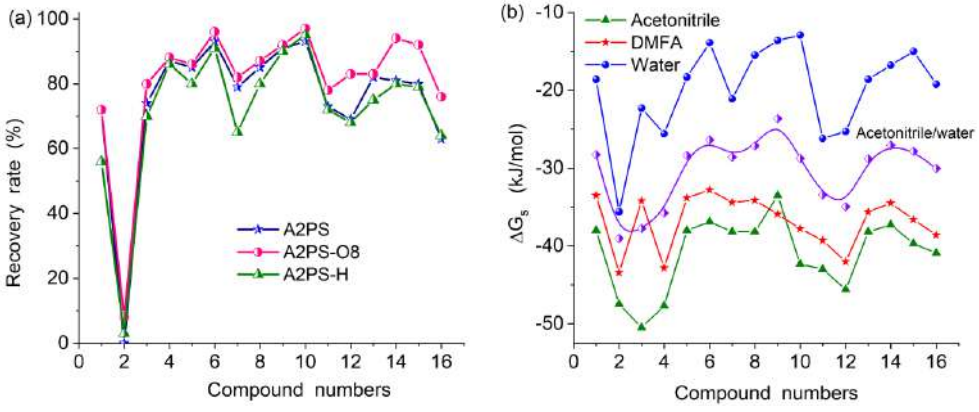

Fig. 43. (*a*) Recovery rates for A2PS-based sorbents and amphetamine derivatives (numbers correspond to compounds in Table 4); (*b*) free energy of solvation of amphetamine derivatives in acetonitrile, DMFA, water, and acetonitrile/water (additive model) calculated using SMD//ωB97X–D/cc–pVDZ (the geometry was optimized with consideration of solvation)

Thus, all the effects observed upon the ^{1}H NMR spectroscopy investigations of bound water and co-solvents could appear upon various studies linked to sorption and interfacial phenomena, solid phase extraction of trace amounts of different organics, or adsorption of metal

and other ions onto various carbon sorbents from aqueous solutions. Pre-adsorbed water (up to a certain limit value) can positively affect the adsorption of light gases (H_2, CH_4) [67–70] or negatively affect the gas-mask efficiency on the breakthrough of harmful gases [135]. On equilibrium conditions, many co-sorbates can displace water from narrower pores into larger ones or most narrow and inaccessible for larger molecules of co-sorbates [67]. Location of water or other solvents in pores with high adsorption potential can negatively affect the sorption of solutes. Therefore, CM with great SSA and narrow PSD in the range of nanopores and narrow mesopores (Table 1, Fig. 8) could be worse sorbents than CM with broader PSD, including nano/meso/macropores. These aspects of the interfacial phenomena could be seen in SPE of various solutes/eluates using various CM in different dispersion media. Upon SPE, changes of solvents can provide effective sorption (concentration) and then elution by other solvents. Therefore, the SPE results depend on several factors such as morphological, textural, and structural characteristics of sorbents, characteristics of solvents/eluents (alone or in mixtures) and sorbates/eluates.

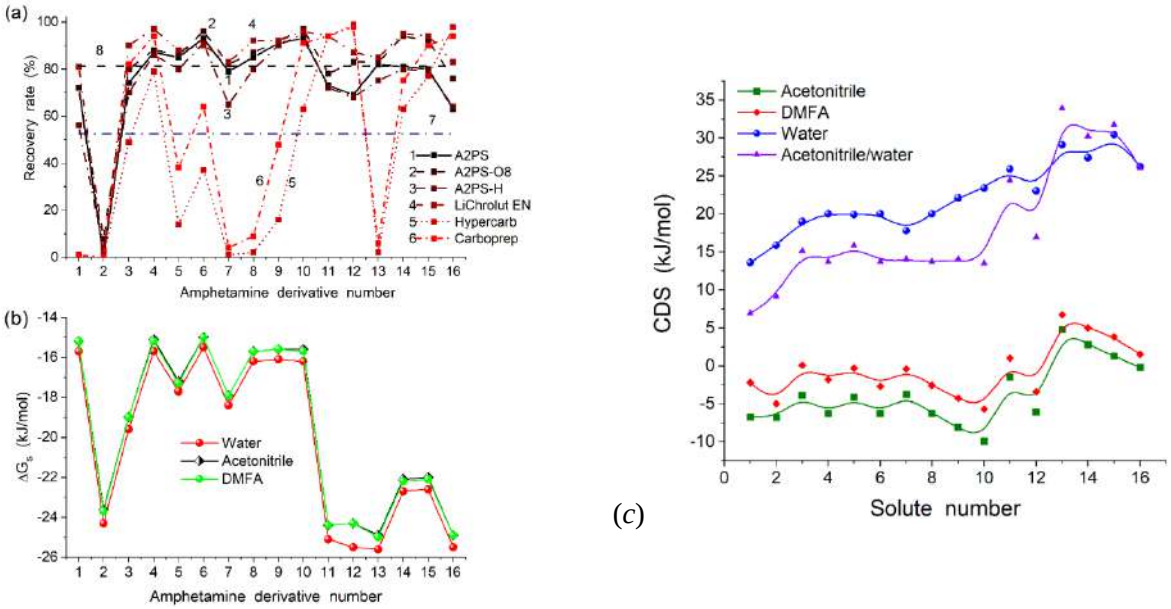

Fig. 44. (*a*) Recovery rates for different sorbents and different amphetamine derivatives; and average recovery for A2PS based CM (line 7) and for graphitized CM (line 8); (*b*) free energy of solvation of amphetamine derivatives in (1) water, (2) acetonitrile and (3) DMFA calculated using IEFPCM/B3LYP/6–31G(d,p) (compound numbers are shown in Table 2); (*c*) non–electrostatic energy of solvation (cavity–dispersion–solvent–structure (CDS) term) of amphetamine derivatives

To study the effects of the surface structure in addition to CSE in CM on SPE efficiency, a set of A2PS-based sorbents (Table 1, Fig. 8) was used. On SPE of trace amounts of solutes/sorbates/eluates, the recovery rates (η_1) for amphetamine, hydroxyamphetamine, metoxy- and methylenedioxyaphetamines sorbed on A2PS, A2PS–O8, A2PS–H, and some reference sorbents from the aqueous solutions (alkalized with ammonia to pH 10 and containing 0.5 vol % of acetonitrile) and desorbed in dimethylformamide (DMFA) are shown in Tables 12 and 13 and Figs. 43a and 44 (this task is linked to forensic investigations). It follows from the individual recovery degrees and their average values for the carbon sorbents that the most effective beds for the extraction of studied amphetamines from the aqueous solutions are well texturally developed AC and polymeric LiChrolut EN. The results for A2PS-based AC are quite consistent since the average recoveries ranged from 77 to 86 % (average value 81 %). The η_1 values for LiChrolut EN (possessing mainly narrow mesopores, Fig. 9f, and high SSA, V_p, and V_{meso}, Table 1) are slightly

higher since the average result reaches 90% (this high result can be due to not only its textural characteristics, such as the absence of narrow nanopores, but also the structure of pore walls). Graphitized CM (especially Hypercarb) with low textural characteristics (Table 1, Fig. 8) give worse results (average 53%). On the other hand, the recovery degrees achieved on Carboprep (possessing narrower mesopores than Hypercarb and Envicarb, Fig. 8) for some amphetamines (amphetamine (A), 2-metoxyamphetamine (2-MA), 2-metoxy-N-methylamphetamine (2-MMA), 3,4-dimetoxyamphetamine (3,4-DMA), 4-metoxy-N-propylamphetamine (4-MPA), 5-bromo-3,4-dimetoxyamphetamine (5-Br-3,4-DMA), 3,4-methylenedioxyethylamphetamine (MDEA), and 5-bromo-3,4-methylenedioxyamphetamine (5-Br-MDA)) are close to the values obtained for LiChrolut EN. For some of them (3,4-DMA, 5-Br-3,4-DMA and 5-Br-MDA), the recoveries by Carboprep and Hypercarb are equal or higher than that for LiChrolut EN. The recoveries of p-hydroxyamphetamine (4-OHA) for all studied sorbents are lower than 10% because of high hydrophilicity of 4-OHA (Figs. 43 and 44, Table 14) that leads to a great value of the desolvation energy for this compound upon sorption, that causes poor sorption onto any CM. Additionally, 4-OHA can strongly bind to polar functionalities at the entrances into pores, that can block the adsorption of other portions of the solute. It is possible to divide sorbents into two groups: (I) LiChrolut EN and A2PS-based AC and (II) graphitized CM. However, the data obtained for N-substituted amphetamines [84, 85] suggested three groups of sorbents: (i) A2PS, A2PS–O8, and LiChrolut EN, (ii) A2PS–H, and (iii) graphitized CM Envicarb and Hypercarb. The highest recoveries (> 90%) were obtained for the first set, while for A2PS–H, the average recovery was 71% since the surface hydroxyls (its amount decreases for A2PS–H) are the main adsorption sites for many sorbates [67]. The results for graphitized CM were from 0 to 80% (average ≈ 35%). For graphitized CM and A2PS-H, the amphetamines recovery rates grow with increasing length of the alkyl chain attached to the amino group. A similar effect can be for derivatives of 4-MA (4-MA, 4-MMA, 4-MEA, and 4-MPA) and MDA (MDA, MDMA, and MDEA) (Tables 2 and 13) clearly observed for graphitized CM (Fig. 44). A reason of these results is an increase in the solute sorption since the residual recoveries decrease (Table 13, η_2) after the first SPE run. This can be explained by preferable sorption of more hydrophobic solutes onto CM than their remaining in solution in polar solvents [67–70]. The results (Table 13) suggest that the position of the methoxy substitute at the benzene ring affects the SPE effectiveness similar to the influence of alkyls attached to the amino group observed for graphitized adsorbents. This is due to a decrease in larger solute sorption onto AC possessing mainly nanopores and narrow mesopores. The recoveries decrease in series 2-MA, 3-metoxyamphetamine (3-MA), 4-metoxyamphetamine (4-MA), 2-MMA, 3-metoxy-N-methylamphetamine (3-MMA), and 4-metoxy-N-methylamphetamine (4-MMA). The adsorption efficiency decreases and the amount of non-retained amphetamines in effluents grows (Table 13, η_2).

The SPE procedure was described in detail previously [82–87, 136, 137]. Standard stock solutions of explosive sorbates were prepared in acetonitrile at a concentration of 1 mg/10 ml, except nitrate esters at a concentration of 5 mg/10 ml. These solutions were stored for a month at 5°C. For recovery studies, aqueous samples were prepared daily and spiked with the described standard solution to get the concentration of 25 μg/100 ml for nitroamines and nitroaromatics but 125 μg/100 ml for nitrate esters. Acetonitrile of 5% vol. (0.48 M) was added to the aqueous samples for complete dilution of explosives. SPE cartridges contained the same amounts (100 mg) of sorbents packed in 3 ml polyethylene tubes with porous polyethylene frits (J. T. Baker, Philipsburg). Prepared cartridges were washed out and conditioned before experiments. Carbon beds were rinsed with 6 ml of DMFA to wash out impurities and then with 20 ml of water. The SPE experiments with the aqueous solutions of explosives using modified CM and HPLC quantification were described in detail elsewhere [82–87, 136, 137]. The 100 ml samples were percolated through the cartridges at a flow rate of 10 ml/min using a vacuum manifold. The residual water was removed by nitrogen aspiration for 10 min and elution was performed with 6 ml of DMFA in 10 ml graduated flask. Water was added to obtain the final eluate volume of

10 ml. When elution with other solvents (tert–butyl methyl ether, dimethyl sulfoxide, acetonitrile, tetrahydrofuran, methanol, ethyl acetate, chloroform) was performed adequately modified procedure of sample preparation was applied. All obtained 6 ml eluates were evaporated to dryness under nitrogen at 45°C. The residues were finally reconstituted to a volume of 10 ml with 6 ml of DMFA and a necessary portion of water.

Table 12. Recovery rates η_1 and η_{aver} (%) of amphetamine derivatives on studied sorbents

Sorbent	η_{aver} **(without 4–OHA)**	**A**	**4–OHA**	**2–MA**	**2–MMA**	**3–MA**	**3–MMA**	**4–MA**	**4–MMA**
A2PS	81	72	0	74	87	85	93	79	85
A2PS–O	86	72	8	80	88	86	96	82	87
A2PS–H	77	56	3	70	86	80	91	65	80
Average for A2PS	81								
LiChrolut EN	90	81	2	90	97	88	90	83	92
Hypercarb	46	0	0	49	79	14	37	1	2
Carboprep	59	1	0	82	94	38	64	4	9
Average	55								

Continued Table 12

Sorbent	η_{aver} **(without 4–OHA)**	**4–MEA**	**4–MPA**	**3,4–DMA**	**5–Br–3,4–DMA**	**MDA**	**MDMA**	**MDEA**	**5–Br–MDA**
A2PS	81	91	93	73	69	82	81	80	63
A2PS–O	86	92	97	78	83	83	94	92	76
A2PS–H	77	90	95	72	68	75	80	79	64
Average for A2PS	81								
LiChrolut EN	90	92	96	94	87	85	95	94	83
Hypercarb	46	16	63	94	99	2	63	77	98
Carboprep	59	48	91	94	98	6	75	90	94
Average	55								

Standard stock solutions of amphetamines at a concentration of 5 mg/ml (as free bases) were prepared in water/acetonitrile (1/1) mixtures and stored for a week at 2°C. For the recovery studies, 100–ml samples of water alkalized with 5 ml of ammonia solution (pH ≈ 10) were prepared daily and spiked with the described standard solution to get a concentration of 50 μg/ml. Prepared cartridges were washed with 5 ml of DMFA and conditioned by 20 ml of water before experiments. The amphetamine samples were percolated through cartridges at a flow rate of 5 ml/min using a vacuum manifold. The effluents obtained from each cartridge were collected for further studies. The residual water was removed from cartridges by nitrogen aspiration for 10 min, and subsequent elution was performed using 5 ml of DMFA in a 10 ml graduated flask. Water was added to obtain the final eluate volume of 10 ml. The consecutive SPE experiments allow separate evaluation of the efficiency of the adsorption and the elution. The effluents obtained after the amphetamine adsorption on the studied sorbents were collected and then passed through a cartridge containing polymeric packing LiChrolut EN (100 mg in 3 ml tube). Then the elution was performed according to the procedure described above.

SPE results for amphetamines (Figs. 44–47, Tables 12–14) and explosives (Figs. 48–50, Tables 15–19) demonstrate a complex character of related interfacial phenomena with concentration (adsorption) of solutes in some solvents and their recovery (elution) in other solvents because each system with sorbent/sorbate(solute/eluate)/solvent has certain unique features affecting the recovery rates. Therefore, there are no simple correlations between the characteristics of the sorbents or solvents (and solutes/eluates) and recovery rates. The calculated solvation energy of solutes depends on the used method, *e.g.*, for amphetamine in water -18.6 kJ/mol (SMD/ωB97X–D/cc–pVDZ, Gaussian 16) -24.4 kJ/mol (SM12/ωB97X/cc–pVDZ, AMS–25.1), -43.0 kJ/mol (SMD/ωB97X–D/cc–pVDZ,

GAMESS 2024 R2). Therefore, to obtain more accurate results, any comparison should be done within the frame of one program, one method, and one basis set.

Table 13. Residual recovery rates of amphetamine derivatives η_2 (%) obtained on LiChrolut EN for the effluents collected after adsorption step (no data for η_2 means 0%) and summarized recoveries $\eta_\Sigma = \eta_1 + \eta_2$ (%)

Sorbent		A	2–MA	2–MMA	3–MA	3–MMA	4–MA	4–MMA	4–MEA
A2PS	η_2	19	15				10		
	η_Σ	91	89	87	85	93	89	85	91
A2PS–O	η_2	21	10				5		
	η_Σ	93	90	88	86	96	87	87	92
A2PS–H	η_2	32	27		11		24	12	
	η_Σ	88	97	86	91	91	89	92	90
LiChrolut EN	η_2	7					11		
	η_Σ	88	90	97	88	90	94	92	92
Hypercarb	η_2	73	32	10	61	49	82	74	67
	η_Σ	73	81	89	75	86	83	76	83
Carboprep	η_2	81	9		52	20	76	79	41
	η_Σ	82	91	94	90	84	80	88	89

Continued Table 13

Sorbent		4–MPA	4–OHA	3,4–DMA	5–Br–3,4–DMA	MDA	MDMA	MDEA	5–Br–MDA
A2PS	η_2			12	18	7	10	12	29
	η_Σ	93	0	85	87	89	91	92	92
A2PS–O	η_2			8	6	12			17
	η_Σ	97	8	86	89	95	94	92	93
A2PS–H	η_2			23	30	19	12	16	28
	η_Σ	95	3	95	98	94	92	95	92
LiChrolut EN	η_2		3						6
	η_Σ	96	5	94	87	85	95	94	89
Hypercarb	η_2	24				75	26	19	
	η_Σ	87	0	94	99	77	89	96	98
Carboprep	η_2					69	12		
	η_Σ	91	0	94	98	75	87	90	94

Table 14. Solvation effects for amphetamines (SMD/ωB97X–D/cc–pVDZ, the geometry was optimized with consideration of solvation using SMD method)

Compound number	Without solvent	Solvent		
		Acetonitrile		
	E_t (Eh)	E_t (Eh)	ΔG_s (kJ/mol)	SMD–CDS (kJ/mol)
1	–405.433818395	–405.448285314	–38.0	–6.7
2	–480.639518807	–480.657614401	–47.5	–6.8
3	–519.925183434	–519.944420785	–50.5	–3.9
4	–559.220675865	–559.238828249	–47.7	–6.3
5	–519.928632687	–519.943088694	–38.0	–4.1
6	–559.225133484	–559.239171640	–36.9	–6.3
7	–519.930415126	–519.944955946	–38.2	–3.8
8	–559.223643543	–559.238182185	–38.2	–6.3
9	–598.531083570	–598.543849363	–33.5	–8.1
10	–637.835525361	–637.851643888	–42.3	–9.9
11	–634.418438568	–634.434818313	–43.0	–1.5
12	–3208.00361037	–3208.02098830	–45.6	–6.1
13	–592.669004181	–592.683539762	–38.2	4.8
14	–631.962471673	–631.976686284	–37.3	2.8
15	–671.269943680	–671.285058594	–39.7	1.3
16	–3166.25179843	–3166.26739251	–40.9	–0.2

Continued Table 14

Compound number	Without solvent	Solvents					
		DMFA			Water		
	E_t (Eh)	E_t (Eh)	ΔG_s (kJ/mol)	SMD–CDS (kJ/mol)	E_t (Eh)	ΔG_s (kJ/mol)	SMD–CDS (kJ/mol)
1	–405.433818395	–405.446592009	–33.5	–2.2	–405.440899476	–18.6	13.6
2	–480.639518807	–480.656062491	–43.4	–5.0	–480.653070868	–35.6	15.9
3	–519.925183434	–519.938207638	–34.2	0.1	–519.933669981	–22.3	19.0
4	–559.220675865	–559.236971417	–42.8	–1.8	–559.230427287	–25.6	20.0
5	–519.928632687	–519.941507001	–33.8	–0.3	–519.935595602	–18.3	19.9
6	–559.225133484	–559.237638643	–32.8	–2.7	–559.230416787	–13.9	20.0
7	–519.930415126	–519.943514304	–34.4	–0.4	–519.938433260	–21.1	17.8
8	–559.223643543	–559.236637733	–34.1	–2.6	–559.229532850	–15.5	20.0
9	–598.531083570	–598.544747493	–35.9	–4.3	–598.536279247	–13.6	22.1
10	–637.835525361	–637.849927911	–37.8	–5.7	–637.840422869	–12.9	23.4
11	–634.418438568	–634.433396506	–39.3	1.0	–634.428398648	–26.2	25.9
12	–3208.00361037	–3208.01962420	–42.0	–3.4	–3208.01322986	–25.3	23.0
13	–592.669004181	–592.682573047	–35.6	6.7	–592.676077297	–18.6	29.1
14	–631.962471673	–631.975611033	–34.5	5.0	–631.968860083	–16.8	27.4
15	–671.269943680	–671.283885590	–36.6	3.8	–671.275657770	–15.0	30.4
16	–3166.25179843	–3166.26651847	–38.6	1.5	–3166.25912661	–19.2	26.2

Note. E_t is the total energy, ΔG_s is the free energy of solvation, SMD–CDS is the non–electrostatic energy of solvation (cavity–dispersion–solvent–structure (CDS) term).

Table 15. Recovery rates η (%) for the first series of A2PS–based CM

Sorbent	EGDN	NG	PETN	TNB	HNDPA	TNMA	TNT	HNDB	HMX	RDX	$\eta_{aver,ad}$
A2PS	99	94	97	70	10	75	2	32	99	99	67.7
A2PSC	20	13	29	53	79	30	45	69	30	21	38.9
A2PSCA	10	6	17	40	47	12	23	48	11	9	22.3
A2PSM	90	72	88	56	27	73	28	64	93	95	68.6
A2PSMC	81	62	83	76	98	36	57	95	78	77	74.3
A2PSMCA	14	10	23	47	45	17	37	71	19	12	29.5
$\eta_{aver,ex}$	52.3	42.8	56.2	57.0	51.0	40.5	32.0	63.2	55.0	52.2	

Note. $\eta_{aver,ad}$ and $\eta_{aver,ex}$ correspond to average recovery rate for a given sorbent and explosive, respectively.

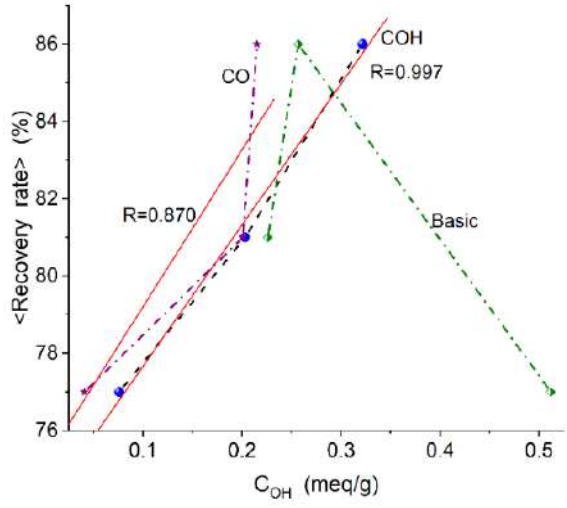

Fig. 45. Relationship between surface content of hydroxyls, CO, basic functionalities (from titration data) and average recovery of amphetamine derivatives on A2PS, A2PS–O8, and A2PS–H

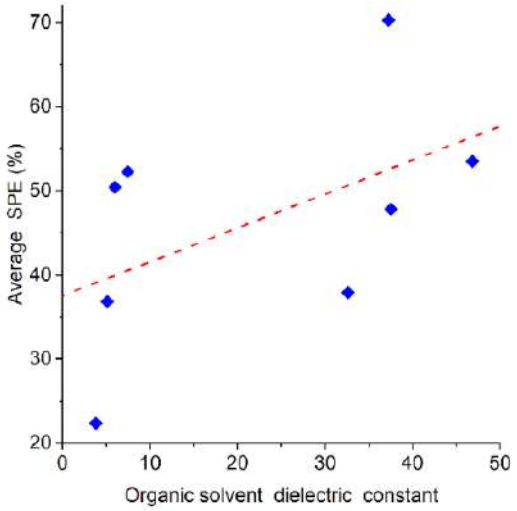

Fig. 46. Relationship between average SPE of amphetamines on A2PS based CM and dielectric constant of used organic solvents

Table 16. Recovery rates η_w (%) for residual solution after adsorption of explosives on CM, total $\eta_\Sigma = \eta + \eta_w$, and relative amounts (a,%) of irreversible adsorbed explosives

Sorbent	Parameter	EGDN	NG	PETN	TNB	HNDPA	TNMA	TNT	HNDB	HMX	RDX
A2PS	η_w	0	0	0	0	0	0	0	0	0	0
	η_Σ	99	94	97	70	10	75	2	32	99	99
	A	1	6	3	30	90	25	98	68	1	1
A2PSCA	η_w	65	60	45	30	35	55	45	20	70	80
	η_Σ	75	66	62	70	82	67	68	68	81	89
	A	25	34	38	30	18	33	32	32	19	11
A2PSMC	η_w	0	15	0	0	0	0	0	0	5	5
	η_Σ	80	77	83	76	98	36	57	95	83	82
	A	20	23	17	24	2	64	43	5	17	18
Initial Coke	η_w	0	0	0	0	0	0	0	0	0	0
	η_Σ	75	63	70	79	40	71	0	34	60	65
	A	25	37	30	21	60	29	100	66	40	35
Coke 8h/Ca/C	η_w	0	0	0	0	0	0	0	0	0	0
	η_Σ	100	80	100	100	100	100	57	95	100	95
	A	0	20	0	0	0	0	43	5	0	5
Evnicarb	η_w	30	55	0	0	0	0	0	0	0	30
	η_Σ	82	70	85	75	88	95	40	83	90	82
	A	18	30	15	25	12	5	60	17	10	18
Hypercarb	η_w	35	60	0	0	0	0	0	0	0	30
	η_Σ	84	75	84	77	88	96	40	82	89	77
	A	16	25	16	23	12	4	60	18	11	23
$A_{average}$		16	22	17	22	28	23	62	30	14	16

Table 17. Recovery rates (%) for explosives on different CM in dimethylformamide

Substance	$\eta_{aver,ex}$	Recovery Rates η (%)					
	(%)	Coke Initial	Coke 1h/Ca/C	Coke 4h/Ca/C	Coke 8h/Ca/C	Envicarb	Hypercarb
EGDN	63.8	75	47	60	100	52	49
NG	42.3	63	35	46	80	15	15
PETN	76.8	70	54	68	100	85	84
TNB	83.8	79	84	88	100	75	77
TNT	30.5	0	23	23	57	40	40
TNMA	86.3	71	77	79	100	95	96
HNDPA	84.0	40	92	96	100	88	88
HNDB	78.2	34	88	87	95	83	82
HMX	87.2	60	84	100	100	90	89
RDX	68.7	65	64	89	95	52	47
$\eta_{aver,ad}$ (%)		55.7	64.8	73.6	92.7	67.5	66.7

Note. $\eta_{aver,ad}$ and $\eta_{aver,ex}$ correspond to average recovery rate for a given sorbent and explosive, respectively.

Table 18. Efficiency of concentration of alkylhalides on CM

Sorbents	Recovery η (%)			
	$C_2H_3Cl_3$	CCl_4	$CHCl_3$	$CHBr_3$
Direct extraction with n–hexane, (%)	78.1	79.5	82.9	91.2
ACR1	38.7	55.3	64.1	85.2
ACR2	27.5	50.0	46.6	48.2
ACR3	46.5	61.6	50.5	65.6

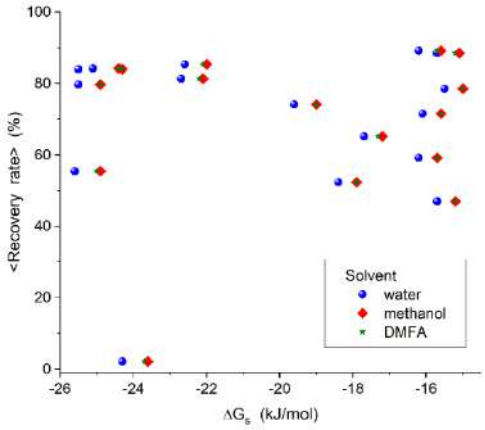

Fig. 47. Relationship between Gibbs free energy of solvation of amphetamine derivatives in different solvents (IEFPCM/B3LYP/6–31G(d,p)) used on SPE and the average recovery rate on A2PS based sorbents

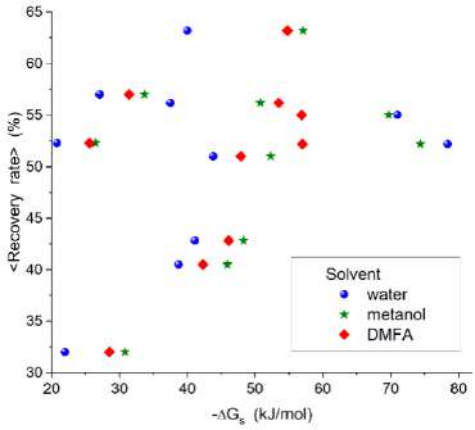

Fig. 48. Relationship between Gibbs free energy of solvation of explosives in different solvents (IEFPCM/B3LYP/6–31G(d,p)) used on SPE and the average recovery rate on A2PS based sorbents

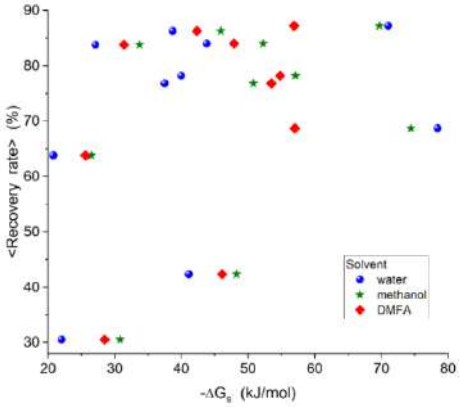

Fig. 49. Relationship between Gibbs free energy of solvation of explosives in different solvents (IEFPCM/B3LYP/6–31G(d,p)) used on SPE and the average recovery rate on coke–based sorbents

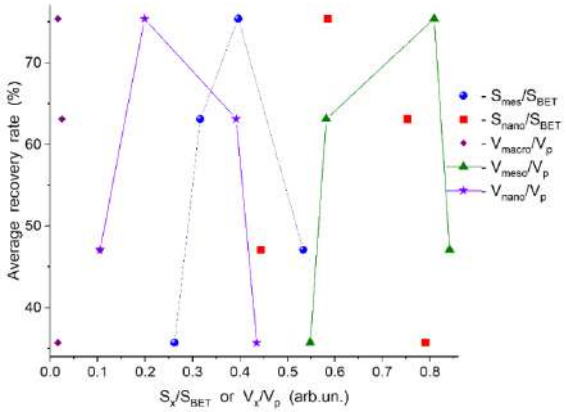

Fig. 50. Relationship between the textural characteristics related to relative contributions of nano–, meso–, and macropores in CM prepared from resins and the average recovery rate on these CM

Table 19. Efficiency of concentration of trace amounts of organics

Probe Compounds	**Sorbent**			
	ACR1	**ACR2**	**ACR3**	**ACR4**
Nitrate Esters				
Ethylene Glycol Dinitrate (EGDN)	83	37	76	27
Trinitroglycerin (NG)	76	42	72	12
Pentaerythritol Tetranitrate (PETN)	81	35	70	47
Cyclic Nitroamines				
Octogen (HMX)	100	45	69	55
Hexogen (RDX)	94	42	75	31
Nitroaromatics				
1,3,5–Trinitrobenzene (TNB)	87	34	46	70
2,4,6–Trinitrotoluene (TNT)	20	13	19	18
Tetryl (TNMA)	62	38	55	65
Hexyl (HNDPA)	93	39	92	59
Hexanitrodibenzyl (HNDB)	58	32	57	87
Average	75.4	35.7	63.1	47.1

$C_2H_3Cl_3$, CCl_4, $CHCl_3$, or $CHBr_3$ dissolved (concentration of 10^{-4} g/ml) in distilled water were used to test the adsorptive properties of synthesized CM. 100 mg of an examined carbon was placed in an extraction column (1 ml), and 100 ml of the aqueous solution of the mentioned organics was passed through this column. Then the adsorbed substance was eluted with 10 ml of n–hexane. The direct extraction with 10 ml of n–hexane from the aqueous solution of the same concentration was used as a relevant test. The ratio of chromatographic peak areas for extraction from the column (P_x) and direct extraction (P_w) was taken as a measure of the efficiency of the concentration process of trace amounts of probe organics; and the recovery efficiency is $\eta = (P_x/P_w)\times 100\%$. The hexane solution of the above compounds at a concentration of 10^{-3} g/ml was used as a standard. A DB–5 (J & W) capillary column (diameter 0.32 mm) with a stationary phase film of the 1μm thickness was used with Helium as a carrier gas at a flow rate of 1 ml/min. The temperature program corresponded to heating at 40°C for 5 min; then the temperature was elevated to 180°C (heating rate 10°C/min), which was kept constant for 5 min. The chromatographic measurements were performed using a GC–6000 Vega 2 gas chromatograph (Carlo Erba Instr.) with an ECD 40 detector. A 3396 (Hewlett Packard) integrator was used for storage and analysis of the chromatographic data. Three groups of explosive materials were chosen to study operation efficiency assessment of concentration process: (i) nitrate esters such as ethylene glycol dinitrate (EGDN), trinitroglycerine (NG), and pentaerythritol tetranitrate (PETN); (ii) cyclic nitramines such as octogen (HMX), and hexogen (RDX); and (iii) nitroaromatics such as 1,3,5–trinitrobenzene (TNB), 2,4,6–trinitrotoluene (TNT), tetryl (TNMA), hexyl (HNDPA), and hexanitrodibenzyl (HNDB) (Promochem, Warsaw, Poland). The solid–phase extraction investigations of these compounds using some commercial CM were described in detail elsewhere (31). All the used solvents (water and dimethylformamide (Lab–Scan, Dublin), acetonitrile and isopropyl alcohol (Merck, Darmstadt)) were of HPLC grade. The standard stock solution of explosives was prepared in acetonitrile at concentrations of 1 mg/10 ml for nitramines and nitroaromatics. For nitrate esters, the concentration was 5 mg/10 ml because of a lower level of detection sensitivity for them. All the used solutions were stored for a month at 5°C. The aqueous samples were prepared daily and spiked with the prepared standard solution to get the concentration of 25 μg/100 ml of nitroamines or nitroaromatics and 125 μg/100 ml of nitrate esters. Acetonitrile (5% v/v) was added to the aqueous samples for complete dilution of explosives.

Computations of the Gibbs free energy of solvation (Figs. 43*b*, 44, Table 11) and comparison of the ΔG_s values with the η_1 (Figs. 43*a*, 44*a*) and η_2 (Table 10) values reveal the influence of solvation/desolvation effects on the sorption efficiency of amphetamines. This effect is observed for 4-OHA with strongly negative ΔG_s values in polar solvents and minimal recovery rates for all sorbents. Notice that a trend of the ΔG_s curve (Figs. 43 and 44*b*, *c*) is close to that for η_1 values (Figs. 43*a* and 44*a*) for more effective sorbents of the first set (A2PS-based AC, LiChrolut EN). This is due to a difference in hydrophobic (dispersion) interactions of amphetamine derivatives with AC, LiChrolut EN, and graphitized adsorbents, and acetonitrile (a water/acetonitrile mixture was used) and smaller SSA values for the latter (Tables 1 and 2). However, these interactions are weaker than the hydrogen bonding, and graphitized sorbents have much smaller SSA and broader pores than A2PS-based AC or LiChrolut EN have (Table 1, Figs. 8 and 9). Therefore, the trend of the recovery rate η_1 for graphitized CM corresponds to a stronger decrease in the η_1 values than the diminution of the ΔG_s values. The CSE differ for these sorbents (it is much smaller for graphitized CM), possessing very different PSD (Figs. 8 and 9). This difference gives more positive results for graphitized CM than could be expected based on their low textural characteristics only; *i.e.*, a decrease in the negative CSE effects on the colligative properties is smaller for CM with broader pores that give the positive results for the SPE. As a whole, the surface functionalities of the carbon sorbents with similar morphology and texture have a relatively weak influence on the recovery rates with similar values for initial A2PS, oxidized

A2PS–O8, and reduced A2PS–H (Fig. 43*a*). However, there is a linear correlation between the amounts of OH-containing surface functionalities and the average recovery rate for A2PS-based CM (Fig. 51). Other characteristics do not give similar linear correlations (Figs. 45–50). There are the SSA and PSD effects because the recovery rates for Carboprep and Hypercarb with low SSA values are lower for a set of compounds than those for other sorbents with greater porosity and SSA (A2PS-based, LiChrolut EN). The solvation/desolvation effects for amphetamine derivatives play an important role and the minimal recovery rate is for 4-OHA characterized by great solvation effects in all used polar solvents. This effect is much stronger than the influence of the porosity and surface chemistry on the η_1 value for 4-OHA. The effects of the structure of amphetamines much strongly appear for graphitized CM because of enhancement of hydrophobic interactions, low SSA, broad pores (providing decreased CSE and increased colligative properties for solutions) of Hypercarb and Carboprep in comparison with AC or LiChrolut EN. Additionally, the presence of strong active sites (*e.g.*, O-containing functionalities) at a surface of sorbents can enhance the CSE because of an increase in the energy of solid–liquid interaction (σ_{sl} in Eq. (21)). This effect could appear on SPE of 4-OHA. Thus, for appropriate modifications of sorbents, possible influence of the active surface sites on SCE should be considered.

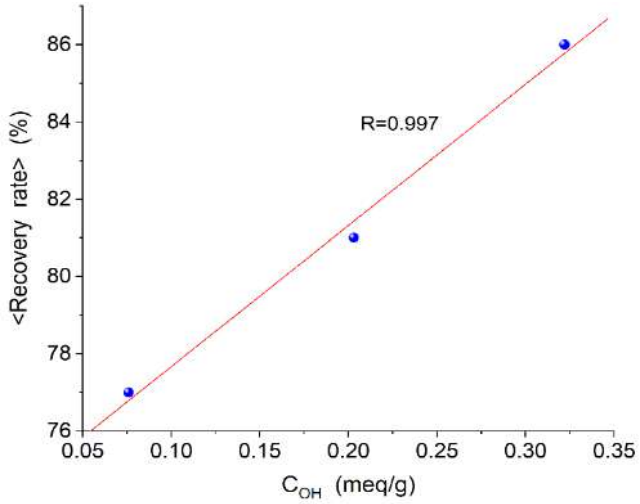

Fig. 51. Linear relationship between surface content of hydroxyls on AC and average recovery of amphetamine derivatives increased for A2PS–H, A2PS, and A2PS–O8 with increasing C_{OH}

Different types of modification of CM could result in significant changes in their textural and structural characteristics, affecting CSE and other interfacial phenomena (Table 1, Figs. 8 and 9). For A2PS-based AC, only A2PSM (activated with Ca(II)) possesses more developed porosity and SSA than initial A2PS. A2PSC, A2PSCA, A2PSMC, and A2PSMCA modified by pyrocarbon deposits (upon chemical vapor deposition, CVD-C) are characterized by strongly diminished porosity and accessible SSA. However, catalytic modification of A2PS (giving enhanced mesoporosity) before pyrocarbon deposition leads to diminution of pore blocking by CVD-C in A2PSMC and A2PSMCA in comparison to that for A2PSC and A2PSCA, respectively, despite larger C_C values. These modifications affect CSE and colligative properties of the solutions that results in changes in the SPE and other interfacial phenomena. Modified Coke-*x* samples with one exception (Coke-1h/Ca/C) have larger pore volume, and for half of them, SSA is larger than that of the initial coke (Table 1). Non-catalytically activated CM are characterized by a significant contribution of nanopores (Table 1). An increase in the burn-off degree with activation time leads to nearly linear increase in SSA, total porosity, volume of nanopores, and SSA of mesopores (Table 1). CM with developed mesoporosity and a marked contribution of the nanoporosity can be effective sorbents for SPE of explosives. However, the chemical composition of the carbon surfaces can also play an important role due to specific interactions of bound polar molecules with

active (polar) surface sites. FTIR spectra of CM (Figs. 13-16, Table 6) show the presence of surface functionalities with C=O (carboxylic, anhydride, lactone, and ketene groups at 1750–1630 cm^{-1}), C–O (lactonic, ether, phenol, *etc.* at 1300–1000 cm^{-1}), CH (3100–2800 cm^{-1}), CC (1600–1450 cm^{-1}), and CH (3070–3030 cm^{-1}) in aromatic groups. A low-intensive band at 2070–2040 cm^{-1} observed for some samples can be due to twinned bonds (C=C=C, C=C=O, C=C=N). Aliphatic structures characterized by the stretching vibrations at 2930 and 2850 cm^{-1} can be linked to both organic molecules adsorbed on CM and functional groups on carbon surfaces. There are low amounts of N-, P-, and S-containing functionalities for CM prepared from natural precursors. An intensive band at 3700–3200 cm^{-1} of adsorbed water, typically observed, overlaps with a band of CO-H. Note that the bands between 2400 and 2300 cm^{-1} can be attributed to adsorbed CO_2 molecules. Thus, the chemical structure of the studied CM is relatively complex. The FTIR spectra of Hypercarb and Envicarb (Figs. 27 and 28) differ significantly from the spectra of other CM, especially over the 1000-1200 cm^{-1} range related to different oxygen-containing functionalities; *e.g.*, for Envicarb, the absorbance is very low there. However, the intensity of a band at 1650 cm^{-1} for this carbon is relatively high. Consequently, Hypercarb and Envicarb are more hydrophobic than other studied CM. Note that polar functionalities can play a significant role (both positive and negative, depending on the characteristics of solvents/eluents and solutes/sorbates/eluates) in SPE and elution of adsorbed organics from different pores. The textural characteristics of CM (as well as the characteristics of solutes/sorbates/eluates and liquid media) affect the concentrating and SPE recovery rates for explosives [82, 83, 86, 87]. The SPE studies of three classes of explosives adsorbed by A2PS-based AC (Tables 15–17) show minimal irreversible adsorption and maximal η values for nitrate esters and cyclic nitroamines for initial A2PS with a large contribution of nanopores (Fig. 8, Table 1). However, significant amounts of nitroaromatics are irreversibly adsorbed by A2PS, *i.e.*, poorly desorbed on elution, that gives low η values. A2PSMC is more effective for nitroaromatics due to smaller contribution of narrow nanopores (Figs. 8 and 9), where the adsorption can be stronger than that in mesopores. The elution of explosives sorbed in narrow nanopores is more difficult than that from mesopores. Thus, a low recovery of nitroaromatics is caused by their irreversible sorption (Table 16, A) in nanopores, especially for TNT bound in narrow nanopores of A2PS. Note that a maximal average η = 78.5% for the same explosives is for A2PS-O. Average SPE rates ($\eta_{aver,ad}$) grow with increasing SSA and pore volume (however, SSA and V_p can be not too great, *e.g.*, for A2PSMC, Hypercarb, or Envicarb with minimal negative CSE on colligative properties of the solutions) and decrease with pore width. The SPE analysis for compounds sorbed by modified cokes and Hypercarb or Envicarb (Tables 15–17) confirms these relationships. Coke-8h/Ca/C demonstrates a high average η value greater than that for other CM. This can be caused by (i) a significant contribution of broad nanopores at $x \approx 1$ nm and narrow mesopores at 1 nm < x < 3 nm (easier occurring sorption and desorption in comparison to those for nanoporous CM characterized by maximal negative CSE), and (ii) lower amounts of surface functionalities (ranges 1400–1700 and 500–800 cm^{-1}) in comparison to some other CM. Specific interactions (*e.g.*, hydrogen bonds) between nitro groups of sorbates and surface hydroxyls can play a negative role on the elution of explosives or other eluates. A simple linear correlation between the solvent polarity and recovery rates is absent [82, 83, 86, 87]. However, a tendency for an increase in the average η values with increasing medium polarity is observed because of the enhancement of elution (despite CSE) of polar molecules by polar solvents. For example, a maximal average η value is for polar DMFA as a solvent/eluent and minimal for nonpolar tert-butyl-methyl ether with a low dielectric constant, and methanol (but its ε value is close to that of DMFA). Note that the hydrogen bonds between nitro groups and surface OH groups of CM are weaker than those for C=O group of DMFA (according to quantum chemical calculations). Therefore, the maximal η values are observed for Coke-8h/Ca/C, having not too large amounts of O-containing functionalities and a significant contribution of mesopores, since

elution of adsorbates from larger pores is more effective (due to smaller CSE) than from narrow pores (maximal CSE). Thus, the analysis of the relationships between the SPE recovery rates and characteristics of both sorbents and sorbates/eluates should be accompanied by the analysis of their chemical compositions and electronic structures affected by solvents; *i.e.*, with consideration for the Gibbs free energy of solvation, sorption, and elution against CSE dependent on the pore sizes. Catalytic or non-catalytic activation of CM allows one to prepare sorbents (*e.g.*, Coke-4h/Ca/C and Coke-8h/Ca/C, A2PS, A2PSM, and A2PSMC, Table 1, Fig. 8) possessing appropriate characteristics for effective sorption and recovery of various organics. The maximum effective multi-step-modified Coke-8h/Ca/C sorbent possesses not too high textural characteristics related to nano- and mesopores, whose contributions are close to one another. Its PSD with respect to mesopores is akin to that of Hypercarb and Envicarb; however, Coke-8h/Ca/C has larger contribution of narrow pores at $x < 2$ nm and large pores at $x > 30$ nm. The effectiveness of Coke-8h/Ca/C in SPE is significantly higher (average value for ten probe compounds of *ca.* 93% using DMFA as an eluent) than that of other sorbents. These effects can be explained by appropriate changes (diminution) of the CSE in broader pores in comparison to that in narrow nanopores of CM. Thus, high SSA and porosity are not always needed to solve some tasks related to the sorption, concentration, elution, and other interfacial phenomena, since stronger CSE in narrower pores are rather negative factor for sorbent efficiency the mentioned applications. An example of sorption efficiency of CMC with relatively low textural characteristics could be seen upon investigations of CMC such as BC based on cheap raw materials. Adsorption experiments were conducted using carbonized BC/NaCl/straw to purify two samples of industrial wastewater containing various compounds (Fig. 52, Table 20).

To analyze the textural characteristics of synthesized bentonite–carbon sorbents, low–temperature (77.4 K) nitrogen adsorption–desorption isotherms (Fig. 52a) were recorded using a Kelvin–1042 adsorption analyzer (Costech Microanalytical). The nitrogen desorption data were used to compute the pore size distributions (Fig. 52b). The images of granules of bentonite–coal sorbents (Fig. 53) were taken using a digital portable microscope, Dino–Lite Special lighting–UV AM4113FVT (Taiwan). The phase composition of the examined samples was identified by employing an X–ray diffractometer (XRD–6100, Shimadzu) (Fig. 54). The Raman spectra (Fig. 55) were recorded using an InViaRaman (Renishaw, UK) spectrometer (785 nm, 1 mW excitation laser). Fourier transform infrared spectroscopy (FTIR) was used to analyze the surface functional groups using an Agilent Technologies Cary 640 Series FTIR Spectrometer with a Li range of 400–4000 cm^{-1} (DR mode) (Fig. 56).

On wastewater purification, the amounts of CMC were 5 g/L, and the equilibration time was 5 h. The amounts of K^+, Na^+, Li^+, Ca^{2+}, Ba^{2+} in water were determined (by 3 times) using a Sherwood Scientific M360 photometer (errors ±1.5–2.0%), and a FlashSmart (Thermo Scientific) apparatus was used for CHNS/O analysis. NH_4^+, NO_2^-, Fe^{2+} were analyzed using UV–5100 spectrophotometer (errors ±0.5%), CO_3^{2-}, HCO_3^-, Ca^{2+} and Mg^{2+} were analyzed by titration (errors ±2–5%), NO_3^- was detected using a Mettler Toledo FiveEasy F30 (errors ±3.0%), SO_4^{2-} and dry residual were estimated using gravimetry (errors ±1–3%), pH was measured using a Mettler Toledo FiveEasy F30. Used CMC regeneration was performed by solution of H_2SO_4 or H_2O_2 for 30 min, then it was washed with distilled water up to neutral pH, and then it was dried at 70°C.

Low–temperature nitrogen adsorption isotherms have an *S*–shape. They can be classified as the 4th type characteristic of porous materials, since a sharp increase is observed in the initial section at low relative pressure, followed by a slowing down at higher relative pressures (Fig. 52*a*). For most samples, the hysteresis loop is not visible due to the low value of their specific surface area. Only the carbonized BC/NaCl/straw sample has a well–defined hysteresis loop, which indicates additional absorption of nitrogen due to capillary condensation.

Nitrogen adsorption–desorption isotherms were used to determine the specific surface area of BC samples, PSD, and their total volume (Fig. 52*a*, Table 1). It was found that the addition of

modifiers to the initial BC contributed to an increase in their SSA and porosity. The SSA value of the initial raw bentonite is 33 $m^2 \cdot g^{-1}$, while the BC sample has the smallest specific surface among the synthesized carbon samples (35 $m^2 \cdot g^{-1}$) with low porosity (total pore surface area of 18 $m^2 \cdot g^{-1}$). The addition of an inorganic component, namely potassium and sodium chlorides, leads to an increase in specific surface area, pore volume, and also contributes to the formation of meso– and microporous. Thus, the BC/KCl sample displayed a twice increase in SSA (71 $m^2 \cdot g^{-1}$) compared to BC.

On the PSD curve (Fig. 52*b*), there are maxima at 1.5 nm (nano/narrow mesopores), 10 nm (mesopores), and a broad peak at 55 nm (macropores), with predominant mesopores contribution. The introduction to the mixture of a plant component, such as sawdust and straw, further increased the total porosity and SSA the BC samples. The carbonized sample BC/KCl/sawdust exhibits the highest total porosity (V_p = 0.27 $cm^3 \cdot g^{-1}$, Table 1), with almost equal contributions from nano– (0.10 $cm^3 \cdot g^{-1}$) and mesopores (0.12 $cm^3 \cdot g^{-1}$). In the case of the BC/NaCl/straw sample, the total porosity is slightly lower (0.19 $cm^3 \cdot g^{-1}$), but the largest contribution is from nanopores (0.026 $cm^3 \cdot g^{-1}$) and mesopores (0.14 $cm^3 \cdot g^{-1}$), and the SSA grows almost 4 times (up to 135 $m^2 \cdot g^{-1}$), which allows us to suggest the best sorption properties of this sample. Additionally, it should be noted that the use of NaCl in the synthesis results in smaller average pore sizes (R = 10.3–12.3 nm) compared to the application of KCl (R = 21.5–23.7 nm) for all synthesized samples.

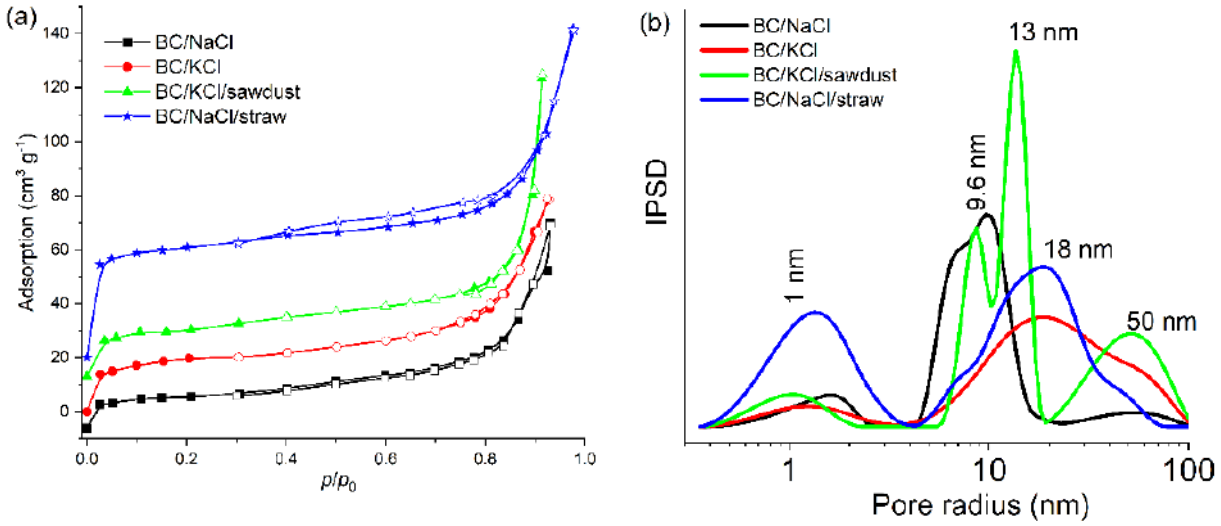

Fig. 52. Low temperature nitrogen adsorption/desorption isotherms (*a*) and incremental pore size distributions (IPSD) curves (*b*) for BC sorbents

Fig. 54 shows the diffraction patterns of the initial bentonite clay and synthesized BC sorbents based on bentonite and brown coal after carbonization/activation at 950°C. Natural bentonite is a polyphase mineral, primarily composed of layered aluminosilicate montmorillonite, α–crystobalite, and kaolinite. The addition of organic components of brown coal, as well as sawdust and crushed straw leads to a slight change in the phase composition of the BC sorbents in comparison with the initial bentonite. The X–ray patterns of all BC sorbents are similar and are characterized by a small halo in the range of 20–30º, which corresponds to the presence of an X–ray amorphous phase and confirms the typical carbon structure. Reflexes characteristic of the minerals of the initial bentonite are also observed: montmorillonite, α–crystobalite, and kaolinite, but their intensity is significantly lower compared to the initial bentonite. This reduction in intensity may result from acid–thermal activation, causing changes in the clay's chemical composition through the removal of cations such as Mg^{2+}, Fe^{2+}, Fe^{3+}, Al^{3+}. It leads to increased surface acidity due to an increase in the number of Brønsted acid sites, while the number of Lewis acid sites may decrease due to the removal of Al^{3+}.

Fig. 53. Granulated activated BC composite

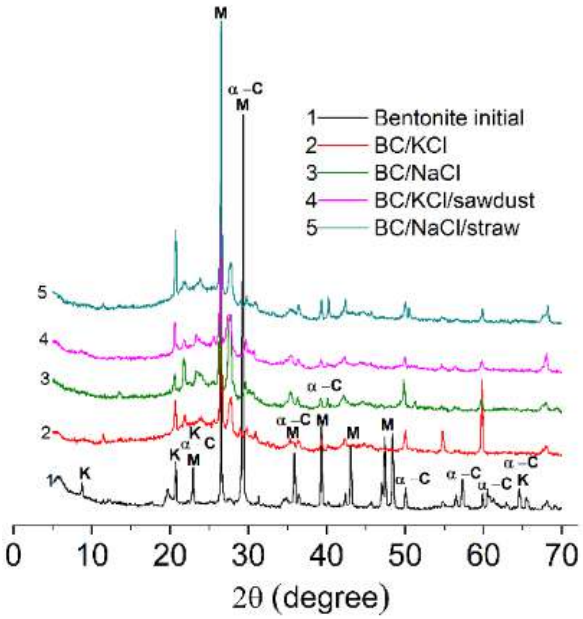

Fig. 54. X–ray diffraction of initial bentonite clay and BC sorbents:
M – montmorillonite, **α–C** – α–crystobalite, **K** – kaolinite

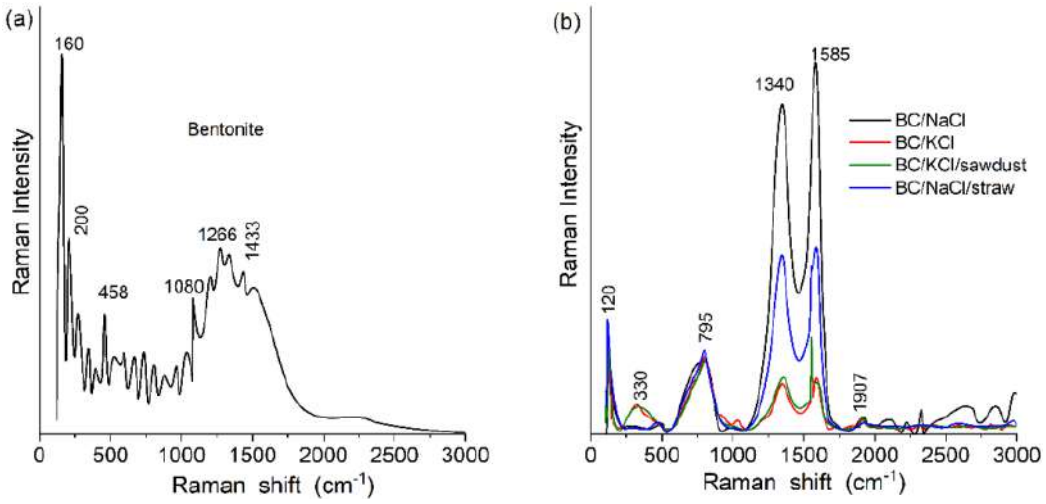

Fig. 55. Raman spectra of initial bentonite clay (*a*) and BC sorbents (*b*), λ = 785 nm

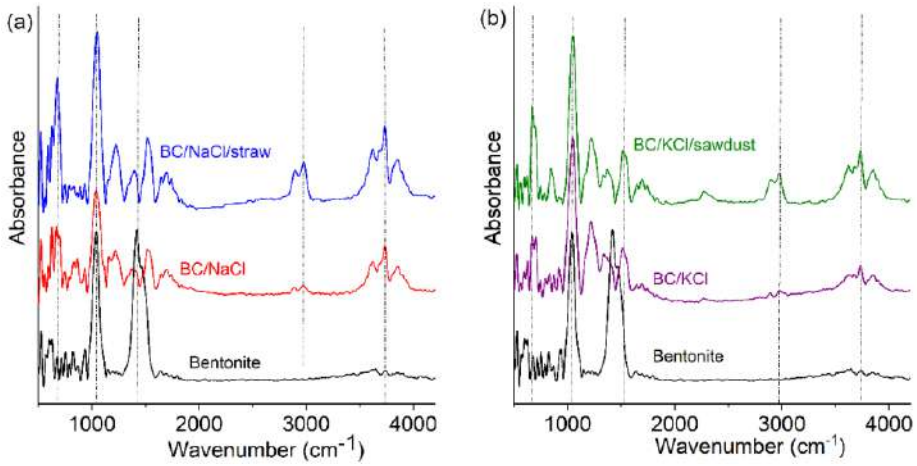

Fig. 56. FTIR spectra of initial bentonite clay (*a*) and BC sorbents (*b*)

The Raman spectra of bentonite and bentonite–carbon sorbents are shown in Fig. 55. There are several Raman peaks associated with mineral constituents in bentonite, including montmorillonite, crystobalite, kaolinite, and water. There is an intense band related to kaolinite at 160 cm^{-1}, since the anatase phase can appear in this area in the spectrum of the initial bentonite (Fig. 55*a*). The presence of α–crystobalite in the synthesized BC sorbents is confirmed by the existence of the corresponding peaks in the Raman spectra: at 120 cm^{-1} and 795 cm^{-1}. The latest one also belongs to the Al–O–H deformation vibrations of montmorillonite. The band with a maximum of 330 cm^{-1} is a superposition of several bands attributed to α–crystobalite (286 cm^{-1} and 368 cm^{-1}) and montmorillonite (289 cm^{-1} and 429 cm^{-1}). The 1080 cm^{-1} band caused by Si–O–Si stretch vibrations of montmorillonite is present in the spectrum of pure bentonite and is absent in the spectra of modified samples. Instead, a band of 1038 cm^{-1} appears in the modified ones, which also lies in the region of probable Si–O–Si or Si–O–C vibrations.

All vibrational modes of H_2O (three internal and six external) are active in the FTIR (Fig. 56) and Raman (Fig. 55) bands at both low and room temperatures. Low–intensity bands in this area belong to the valence vibrations of surface OH groups. The bending mode of H_2O 1637 cm^{-1} is masked by two intense bands in the region 1100–1700 cm^{-1} corresponding to coal (1500–1600 cm^{-1} – G-band and 1345 cm^{-1} – D-band). These peaks depend on several parameters, such as clustering of sp^2 phases, carbonization rate of materials, unevenness of bonds, sp^2/sp^3 ratio, porosity, crystal size, and presence of sp^2 rings. Peaks around 3600–3850 cm^{-1} may be attributed to the stretching vibrations of free or interlayer water molecules and hydroxyl groups. The removal of carbonates during decarbonization might reveal or alter these hydroxyl groups.

These wastewater samples exhibited high hardness levels exceeding 29 mg/eq.% and contained heavy metal ions, sulfate ions, chlorides, cyanides, and thiocyanides (Table 20, Fig. 57). Following treatment, bentonite-coal sorbents demonstrated significant efficacy in the sorption of various compounds (Table 20, sorbent amount 5 g/L, equilibration time 5 h). After water treatment, the sorbents underwent chemical regeneration to check the potential degradation during recycling. A 3% sulfuric acid (H_2SO_4) solution and a 3% hydrogen peroxide (H_2O_2) solution were used as regenerants (30 min), then washed and dried. The regenerated sorbents were then reused for wastewater treatment. Results indicated that sulfuric acid regeneration is more effective in comparison to sorbent recovery by hydrogen peroxide. These findings suggest that the regeneration using strong oxidants yields promising results, supporting the feasibility of multiple regeneration cycles. For the dynamic and equilibrium co-adsorption of low- (LMWC) and high-molecular (HMWC) weight compounds on AC, the adsorption results depend on several factors: AC PSD, concentrations of solutes, adsorption kind, solvent characteristics, *etc*. For AC possessing only nanopores and narrow mesopores, HMWC can more easily block the pore entrances that results in a decrease in the LMWC adsorption [1–4, 67, 138]. Additionally, HMWC can mainly

adsorb on the outer surfaces of AC particles with narrow PSD that corresponds to rather low adsorption ability of nanoporous CM concerning HMWC. The effects of HMWC on the LMWC co-adsorption decrease for AC possessing broad meso- and macro-pores [138].

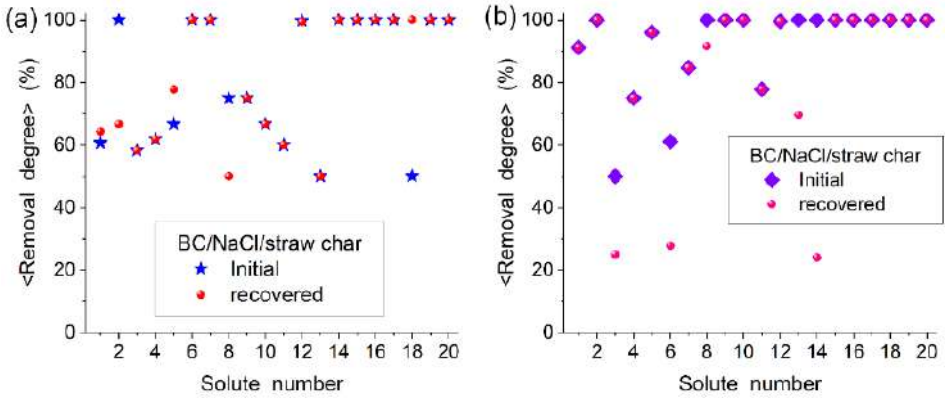

Fig. 57. Removal degree of various cations and anions from industrial wastewater: (a) recycled water from bacterial oxidation reactors and (b) tailings pond water containing Al^{3+} (solute number 1), Ba^{2+}(2), Br^{-} (3), Ca^{2+} (4), Cl^{-} (5), Cr^{3+}(6), Cu^{2+} (7), CN^{-} (8), Fe^{3+} (9), K^{+} (10), Mg^{2+} (11), Mo^{2+} (12), Mn^{2+} (13), Ni^{2+}(14), NO^{2-} (15), NO^{3-} (16), SO_4^{2-} (17), SiO_2 nanoparticles (18), Zn^{2+} (19), and cyanic acid (20)

Table 20. Sorption characteristics of carbonized BC/NaCl/straw to purify industrial wastewater (the regeneration was using sulfuric acid 3 g/l)

Ions content (mg/l) Sample	**Al^{3+}**	**Ba^{2+}**	**Br^{-}**	**Ca^{2+}**	**Cl^{-}**	**Cr^{3+}**	**Cu^{2+}**	**CN^{-}**	**Fe^{3+}**	**K^{+}**
Recycled water from bacterial oxidation reactors										
Initial composition of industrial wastewater	0.028	3	0.12	0.21	0.09	0.03	0.01	0.004	0.04	0.3
After sorption by initial sorbent	0.011	0	0.05	0.08	0.03	–	–	0.001	0.01	0.1
Regenerated 1	0.012	1	0.06	0.10	0.03	0.01	1.02	0.002	0.02	0.1
Regenerated 2	0.010	0	0.04	0.08	0.02	0.01	–	0.002	0.01	0.1
Regenerated 3	0.010	1	0.05	0.08	0.02	–	–	0.002	0.01	0.1
Tailings pond water										
Initial water	0.068	1	0.04	0.2	0.25	0.18	0.72	0.012	0.03	0.4
After sorption by initial sorbent	0.006	0	0.02	0.05	0.01	0.07	0.11	0	0	0
Regenerated 1	0.006	0	0.03	0.06	0.01	–	–	0.001	0.01	0
Regenerated 2	0.006	0	0.03	0.05	0.01	0.00	–	0.001	0	0
Regenerated 3	0.006	0	0.03	0.05	0.01	0.13	0.11	0.001	0	0

Continued Table 20

Ions content (mg/l) Sample	**Mg^{2+}**	**Mo^{2+}**	**Mn^{2+}**	**Ni^{2+}**	**NO_2^{-}**	**NO_3^{-}**	**SO_4^{2-}**	**SiO_2**	**Zn^{2+}**	**cyanuric acid**	**Turbidity**
Recycled water from bacterial oxidation reactors											
Initial composition of industrial wastewater	0.10	4.3	0.4	0.026	7	1.2	1	2	0.02	1	11
After sorption by initial sorbent	0.04	0.01	0.2	0	–	0	0	1	0	0	1
Regenerated 1	0.05	0.03	0.2	0	–	0	0	1	0	0	5
Regenerated 2	0.04	0.03	0.2	0.048	–	0	0	–	0	0	4
Regenerated 3	0.04	0.03	0.2	–	0	0	0	–	0	0	4
Tailings pond water											
Initial water	0.09	4.67	0.33	0.1	63	0.63	5.67	0.1	0.06	2.33	30
After sorption by initial sorbent	0.02	0.02	0	0	–	0	0	0	0	0	2
Regenerated 1	0.02	0.02	0	0	–	0	0	0	0	0	3
Regenerated 2	0.02	0.02	0	0	–	0	0	0	0	0	2
Regenerated 3	0.02	0.02	0.1	0.076	–	0	0	0	0	0	2

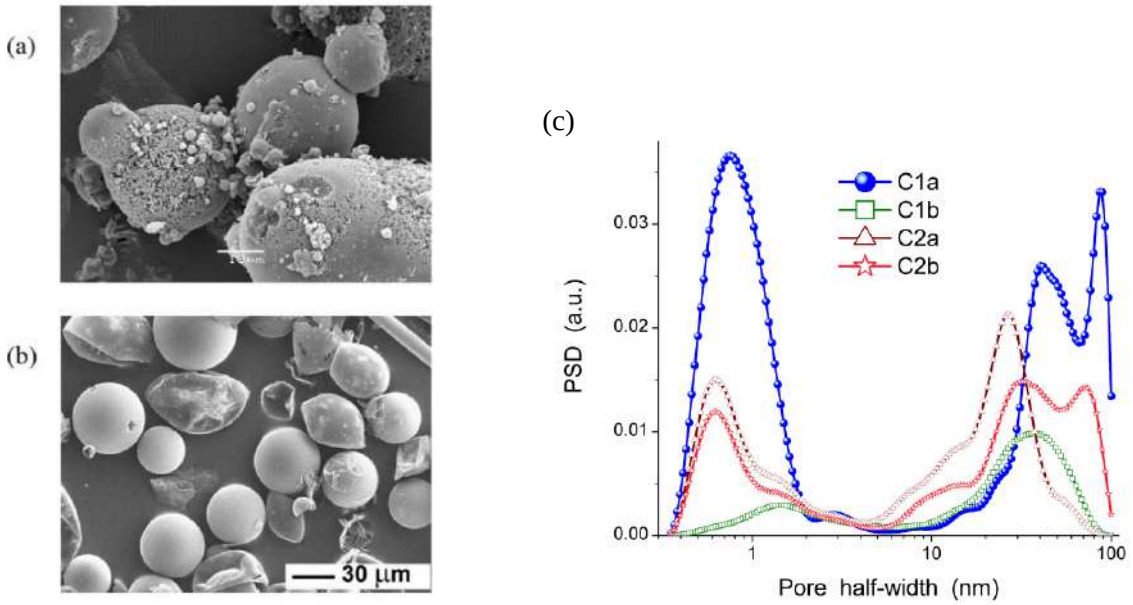

Fig. 58. SEM images of CM (*a*) C2a and (*b*) C1a; and (*c*) pore size distributions of different ACs (SCV/SCR model)

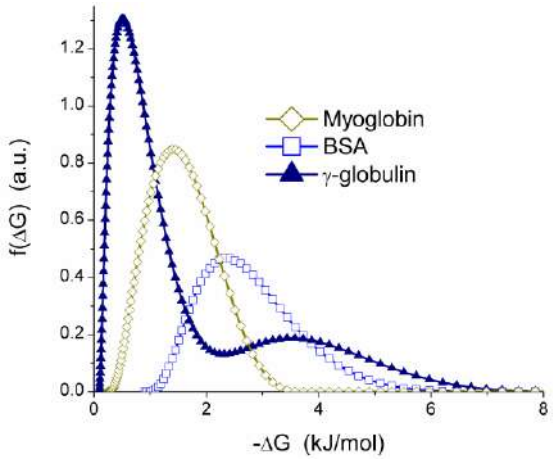

Fig. 59. Distribution functions of the Gibbs free energy of the protein adsorption onto carbon C1a (kernel in integral equation of a Langmuir type similar to Eq. (9))

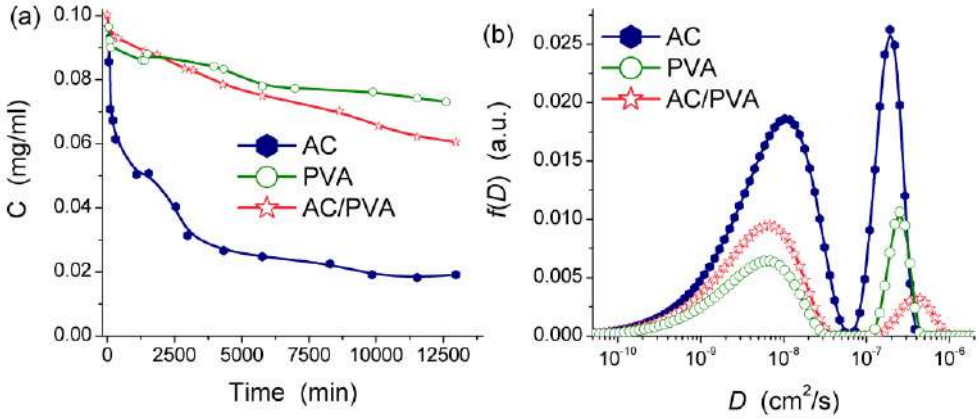

Fig. 60. (*a*) Kinetics of Mb adsorption (residual concentration is shown) on C1a carbon (batch mode), PVA cryogel and AC–PVA composite cryogel (0.9 × 2.5 cm) (flow–through mode), containing the same amount of AC (6 mg, 3.8 mg/mL); and (*b*) the distribution functions of the Mb diffusion coefficient

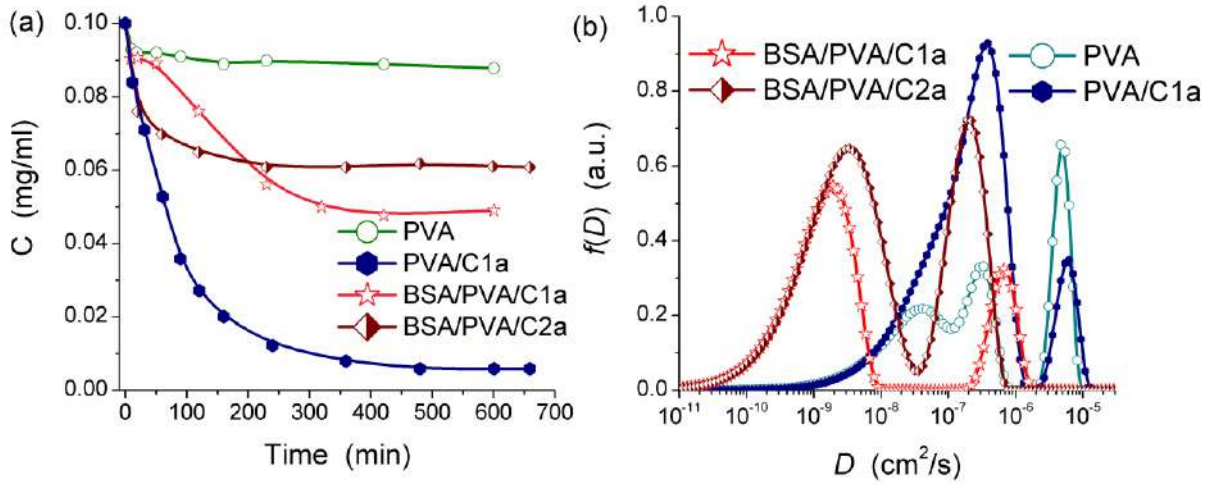

Fig. 61. (*a*) Residual concentration of myoglobin in 10 mM sodium phosphate buffer solution containing 0.15 M sodium chloride and 0.02% w/v sodium azide, pH 7.0 or in the same buffer solution containing 50 mg/mL albumin pumped through PVA or AC–PVA composite cryogels (3×100 mm) of a high carbon content (40 mg/mL), as a function of time. (*b*) The corresponding distribution functions of the myoglobin diffusion coefficient

Table 21. Structural characteristics of activated carbons

Sample	S_{BET}, m²/g	S_{nano}, m²/g	S_{meso}, m²/g	S_{macro}, m²/g	V_p, cm³/g	V_{nano}, cm³/g	V_{meso}, cm³/g	V_{macro}, cm³/g	Δw	c_{slit}	c_{cyl}	c_{void}	Treatment
C1a	1939	1553	364	23	1.82	0.698	0.355	0.762	0.433	0.770	0.097	0.133	CO_2 at 910 °C and then in air at 300 °C
C1b	167	50	105	12	0.38	0.025	0.193	0.222	0.351	0.496	0.499	0.005	1500 °C
C2a	749	622	166	11	0.74	0.272	0.482	0.236	0.327	0.717	0.114	0.169	CO_2 at 910 °C and then in air at 300 °C
C2b	644	498	122	16	0.8	0.214	0.297	0.450	0.286	0.615	0.165	0.220	CO_2 at 910 °C

Note. The samples C1a and C1b were produced from one phenolic resin precursor; the samples C2a and C2b were produced from another phenolic resin precursor. Δw is the relative deviation (errors) of the pore shape with SCV/SCR model; c_{slit}, c_{cyl} and c_{void} are the weight coefficients of slit and cylindrical pores and voids between spherical particles, respectively.

Table 22. Structural characteristics of CM calculated from the nitrogen adsorption isotherms

Carbon	S_{BET} (m²/g)	S_{ext} (m²/g)	V_p (cm³/g)	$V_{nano,,slit}$ (m³/g)	$V_{meso,slit}$ (cm³/g)	$V_{macro,slit}$ (cm³/g)	$S_{nano,slit}$ (m²/g)	$S_{meso,slit}$ (m²/g)	$S_{macro,slit}$ (m²/g)	Δw_{slit}
Carboxen 569	457	347	0.51	0.114	0.265	0.130	178	44	3	0.471
Carboxen 1002	1177	386	0.97	0.454	0.188	0.323	821	54	10	0.160
Carboxen 1003	1168	436	0.85	0.451	0.222	0.137	820	66	6	0.147
Carboxen 1010	953	247	0.46	0.367	0.035	0.058	697	26	1	0.143
Carboxen 1012	1375	352	0.64	0.590	0.048	0.003	968	36	0	0.041
Carboxen 1016	74	63	0.44	0.011	0.238	0.191	28	28	6	0.205
Carbopack B	99	79	1.02	0.015	0.276	0.730	25	42	19	0.151
Carbopack F	6	6	0.02	0.001	0.010	0.011	2	2	0	0.275
Carbopack X	225	203	0.47	0.105	0.245	0.120	164	41	3	0.073

Interactions of macromolecules with CM depend strongly on the PSD because nanopores and narrow mesopores are rather inaccessible for large molecules due to the steric effects. Interactions of BSA, myoglobulin, and γ–globulin with CM possessing broad PSD (Fig. 58, Table 21) are characterized by different Gibbs free energy of adsorption (Fig. 59), kinetics, and diffusivity (Figs. 60 and 61) [139,140]. In the case of nanoporous CM, the adsorption of biomacromolecules occurs only onto the external surface of carbon microparticles [138].

Among the studied carbon sieves and graphitized carbon blacks, microporous Carboxens 1010 and 1012 possess simpler PSD in comparison with other CM characterized by more complex multimodal PSD including pores over a wide range from narrow nanopores at x = 0.35–0.6 nm, supernanopores at x between 0.7 and 2 nm, mesopores and/or macropores (Table 22) [139,140]. Such a complex structure of pores results in a complex shape of the adsorption potential distributions, especially for non–graphitized carbon sieves. Graphitization significantly reduces not only the textural non–uniformity of CM but also the energetic heterogeneity of their surfaces.

Analysis of the PSDs of mesopores at x < 25 nm (Carboxens 569, 1002, 1003, 1016) and macropores at x > 25 nm (Carboxen 569, Carbopacks B and X) (Supelco, Inc.) shows [138] that these CM can effectively adsorb relatively large biomacromolecules with the size from several till dozen nanometers. This assumption is confirmed by the investigation of the adsorption of lipopolysaccharide (Sigma Aldrich) molecules by different CM. The efficiency of this process depends not only on the total pore volume but also on contributions of large mesopores and macropores of the sorbents and their particle size. Therefore, nanoporous Carboxen 1010 adsorbs only 20% of LPS mainly by the outer surface of particles, whereas Carboxen 1003 adsorbs 90% of LPS because of its larger pore volume, specific surface area, and essential meso/macroporosity [138].

CONCLUSION

Various carbon materials and related composites represent a large set of materials effectively used in industry, medicine, and science. There are several aspects causing effective applications of CM. Different treatment methods could be used to strongly change the particulate morphology, carbon sheet size and shape, porosity, SSA, PSD, and surface functionalities. Strong changes in the CM characteristics appear in significant changes in the interfacial phenomena occurring in pores, where confined space effects, colligative properties, cryoscopic effects, changes in molecular mobility of solutes/sorbates/eluates, and activity of solvents could result not only in expected phenomena but also in some unexpected ones. Some of these effects could be positive for certain practically important applications (e.g., irreversible adsorption of harmful compounds and ions), but others could be negative ones, such as CSE reducing SPE efficiency on CM possessing narrow pores. Low temperature ^{1}H NMR spectroscopy of water, solvents, liquid mixtures, solutions of low- and high-molecular weight compounds, various ions, *etc.* give detailed information on the temperature and interfacial behaviors of the complex systems, CSE/CE, solvent activity *vs*. pore sizes, changes in location of solvents in different pores due to changes in dispersion media, *etc.* Additionally, ^{1}H NMR cryoporometry allows one to analyze the distribution of water alone or in mixtures with polar and nonpolar organic solvents, and various solutes in pores of different sizes. This approach gives information on changes in solvent activity in pores of different sizes depending on temperature, concentration, and other conditions. All these results are important for a deeper insight into various interfacial phenomena appearing on practical applications of CM and other sorbents. More comprehensive results and deeper insight into complex interfacial phenomena including sorption from complex solutions, SPE of trace amounts of various solutes, *etc.* could be obtained using a maximum wide set of methods: (i) microscopic, XRD, SAXS, gravimetry for analysis of the particulate morphology; (ii) adsorption of probes (*e.g.*, nitrogen, benzene, water) and SAXS for textural characterization; (iii) spectral (FTIR, Raman, UV/vis, XPS) and titration methods to analyze the surface structure and presence of different functionalities; (iv) NMR, gravimetry, differential scanning calorimetry, quantum chemistry to study interfacial phenomena; (v) equilibrium and kinetic adsorption, breakthrough dynamics, SPE, *etc.* for estimate efficiency of different CM in various applications. The results analyzed in the present work are of interest from both theoretical and practical points of view because they show different aspects of the interfacial phenomena occurring in pore space of various CM and composites characterized by very different morphology, texture, and surface structure that is important for optimization of CM/CMC characteristics for effective usage in various applications.

REFERENCES

1. Safeer S., Pandey R. P., Rehman B., Safdar T., Ahmad I., Hasan S. W., Ullah A. A review of artificial intelligence in water purification and wastewater treatment: recent advancements. *J. Water Proc. Eng.* 2022. **49***:* 102974.
2. Newcombe G., Dixon D. (Eds.) *Interface Science in Drinking Water Treatment. Theory and Application* (Vol. 10, Interface Science and Technology, Elsevier, 2006).
3. Somasundaran P. (Ed.) *Encyclopedia of Surface and Colloid Science* (Third Edition, CRC Press: Boca Raton, 2015).
4. Ahuja S. (Ed.) *Separation Science and Technology* (Vol. 15, Elsevier: Amsterdam, 2022).
5. Ledesma Cano B., Rodríguez E. M., González González J. F., Nogales-Delgado S. Reuse of Activated Carbons from Filters for Water Treatment Derived from the Steam Cycle of a Nuclear Power Plant. *C.* 2025. **11**: 19.
6. Cao Y., Dhahad H. A., Hussen H. M., Anqi A. E., Farouk N., Issakhov A., Xu N.-Y., Wei Z. Adsorption properties of two-dimensional carbon material towards the heavy metal ions. *J. Mol. Liquids.* 2021. **342**: 117500.
7. Suoa C., Dub K., Yuana R., Chena H., Wanga F., Zhou B. Adsorption study of heavy metal ions from aqueous solution by activated carbon in single and mixed system. *Desal. Water Treat.* 2020. **183**: 315.
8. Wu Q., Li W., Liu S. Carboxyl-rich carbon microspheres prepared from pentosan with high adsorption capacity for heavy metal ions. *Mater. Res. Bull.* 2014. **60**: 516.
9. Saygılı H., Akkaya Saygılı G. A., Levent A. Design of microwave-supported activated carbon derived from lentil processing residual for efficient heavy metals adsorption and supercapacitor applications. *Talanta.* 2025. **293**: 128068.
10. Sun J., Li M., Zhang Z., Guo J. Unravelling the adsorption disparity mechanism of heavy-metal ions on the biomass-derived hierarchically porous carbon. *Appl. Surf. Sci.* 2019. **471**: 615.
11. Li K., Li Q., Zhang Y., Yang Y., Jiang T. Effect of metal ions on gold adsorption onto activated carbon in the acidic thiourea solution: Experiment study and DFT calculation. *J. Mol. Liquids.* 2023. **387**: 122691.
12. Kyzasa G. Z., Bomisa G., Kosheleva R. I., Efthimiadou E. K., Favvas E. P., Kostoglou M., Mitropoulos A. C. Nanobubbles effect on heavy metal ions adsorption by activated carbon. *Chem. Eng. J.* 2019. **356**: 91.
13. Marciniak M., Goscianska J., Frankowski M., Pietrzak R. Optimal synthesis of oxidized mesoporous carbons for the adsorption of heavy metal ions. *J. Mol. Liquids.* 2019. **276**: 630.
14. Aguayo-Villarreal I.A., Bonilla-Petriciolet A., Muñiz-Valencia, R. Preparation of activated carbons from pecan nutshell and their application in the antagonistic adsorption of heavy metal ions. *J. Mol. Liquids*. 2017. **230**: 686.
15. Luo X., Zhang Z., Zhou P., Liu Y., Ma G., Lei Z. Synergic adsorption of acid blue 80 and heavy metal ions (Cu^{2+}/Ni^{2+}) onto activated carbon and its mechanisms. *J. Ind. Eng. Chem.* 2015. **27**: 164.
16. de Castro-Alves L., Yanez-Vilar S., Gonzalez-Gomez M. A., Garcia-Acevedo P., Arnosa-Prieto A., Pineiro-Redondo Y., Rivas J. Understanding adsorption mechanisms and metal ion selectivity of superparamagnetic beads with mesoporous CMK-3 carbon and commercial activated carbon. *Microp. Mesop. Mater.* 2024. **374**: 113159.
17. Ahmad A., Kumar R., Jawaid M. (Eds.) *Emerging Techniques for Treatment of Toxic Metals from Wastewater* (Elsevier: Amsterdam, 2022).
18. Moreno–Piraján J. C., Giraldo–Gutierrez L., Gómez–Granados F. *Porous Materials. Theory and Its Application for Environmental Remediation* (Springer Nature: Cham, 2021).
19. Rousseau R.W. *Handbook of Separation Process Technology* (John Wiley & Sons: New York, 1987).

20. Rahimi V., Pimentel C.H., Gómez-Díaz D., Freire M.S., Lazzari M., González-Álvarez J. Development and Characterization of Biomass-Derived Carbons for the Removal of Cu^{2+} and Pb^{2+} from Aqueous Solutions. *C.* 2025. **11**: 2.
21. Huang Y., Luo Y., Liu Z., Xie X., Xue M., Gao B. Engineering carbon materials for organic pollutant removal via adsorption and photodegradation: A review. *Separation and Purification Technology.* 2025. **359**: 130872.
22. Zhang C., Li J., Chen Z., Cheng F. Factors controlling adsorption of recalcitrant organic contaminant from bio-treated coking wastewater using lignite activated coke and coal tar-derived activated carbon. *J. Chem. Technol. Biotechnol*. 2017. **93**: 112.
23. Liu F., Wang Q., Zietzschmann F., Yang F., Nie S., Zhang J., Yang M., Yu J. Competition & UV_{254} projection in odorants vs natural organic matter adsorption onto activated carbon surfaces: Is the chemistry right? *Water Res.* 2025. **268**: 122764.
24. Anumol T., Sgroi M., Park M., Roccaro P., Snyder S.A. Predicting trace organic compound breakthrough in granular activated carbon using fluorescence and UV absorbance as surrogates. *Water Res*. 2015. **76**: 76–87.
25. Apul O.G., Wang Q., Zhou Y., Karanfil T. Adsorption of aromatic organic contaminants by graphene nanosheets: comparison with carbon nanotubes and activated carbon. *Water Res.* 2013. **47**: 1638.
26. Bhatnagar A., Sillanpää M. Removal of natural organic matter (NOM) and its constituents from water by adsorption – A review. *Chemosphere.* 2017. **166**: 497–510.
27. Bong T., Kang J.-K., Yargeau V., Nam H.-L., Lee S.-H., Choi J.-W., Kim S.-B., Park J.- A. Geosmin and 2-methylisoborneol adsorption using different carbon materials: isotherm, kinetic, multiple linear regression, and deep neural network modeling using a real drinking water source. *J. Clean. Prod*. 2021. **314**: 127967.
28. Cheng W., Dastgheib S. A., Karanfil T. Adsorption of dissolved natural organic matter by modified activated carbons. *Water Res*. 2005. **39**: 2281.
29. Fan W., Sun G., Wang Q., Yang F., Gao Y., Yang M. Identifying the critical activated carbon properties affecting the adsorption of effluent organic matter from bio-treated coking wastewater. *Sci. Total. Environ*. 2023. **871**: 161968.
30. Hena S., Patil K.S., Leinecker N., Bhatelia T., Shah M. Effect of algal organic matter on adsorption of glyphosate using coconut shell-activated carbon. *Chem. Eng. J. Adv.* 2025. **22**: 100754.
31. Liu Y., Wei G., Liu H., Zhao S., Su X., Zhu Y., Wang X. Effect of organic/inorganic separation on the adsorption performance of sludge-based activated carbon. *J. Env. Chem. Eng.* 2024. **12**: 114861.
32. Chen F., Ma L., Wang R., Chai Y., Zhan Y., Chen C. Enhanced adsorption of organic matter from coal chemical membrane concentrate by applying positive potential to mesoporous activated carbon fiber. *Separ. Purif. Techn.* 2025. **369:** 133128.
33. Juang R.-S., Ke G.-C., Lee C. C. Adsorption removal of low-molecular-weight uremic toxins from simulated spent dialysate using various low-cost mixed-matrix membrane stacks. *Journal of the Taiwan Institute of Chemical Engineers.* 2025. **169**: 105987.
34. Ma Y. H., Li S. H., Tonelli M. Unsworth L. D. Adsorption-based strategies for removing uremic toxins from blood. *Microp. Mesop. Mater.* 2021. **319**: 111035.
35. Ho L., Lambling P., Bustamante H., Duker P., Newcombe G. Application of powdered activated carbon for the adsorption of cylindrospermopsin and microcystin toxins from drinking water supplies. *Water Res*. 2011. **45**: 2954
36. Wanga H., Hob L., Lewisa D. M., Brookes J. D., Newcombe G. Discriminating and assessing adsorption and biodegradation removal mechanisms during granular activated carbon filtration of microcystin toxins. *Water Res*. 2007. **41**: 4262.

37. Zhao X., Wang C., Xu B., Liang J., Li K., Guo Y., Gong M., Zhao Y., Huang Y., Li Y., Zha M., Zhuang D., Gong Q. Efficient selective adsorption of cytokine IL-6 and other middle-macromolecular toxins in the serum of uremia patients with specially designed porous hollow carbon spheres. *Chem. Eng. J.* 2023. **454**: 140213.
38. Yang C., Diao L., Song Z., Guan C., Xu L., Bu Q., Jiang W., Yu H., Li D., Xu Y. Mesoporous activated carbon derived from Chinese herbal medicine residues for hemoperfusion removal of uremia toxins from progressive chronic kidney diseases patients. *Heliyon* 2024. **10**: e38892.
39. Annesini M. C., Piemonte V., Turchetti L. Removal of albumin-bound toxins from albumin-containing solutions: Tryptophan fixed-bed adsorption on activated carbon. *Chem. Eng. Res. Design*. 2010. **88**: 1018.
40. Gregg S. J., Sing K. S. W., Stoeckli H. F. (Eds.) *The Characterisation of Porous Solids* (The Society of Chemistry and Industry: London UK, 1979).
41. Gregg S. J., Sing K. S. W. *Adsorption Surface Area and Porosity* (2nd ed. Academic Press: London, 1982).
42. Adamson A. W., Gast A. P. *Physical Chemistry of Surface* (6th ed., Wiley: New York NY USA, 1997).
43. Yang R. T. *Adsorbents: Fundamentals and Applications* (Wiley: New York, 2003).
44. *Ullmann's Encyclopedia of Industrial Chemistry* (Wiley–VCH: Weinheim, 2008).
45. Bhadra B. N., Seo P. W., Jhung S. H. Adsorption of diclofenac sodium from water using oxidized activated carbon. *Chem. Eng. J.* 2016. **301**: 27.
46. Amuda O. S., Giwa A. A., Bello I. A. Removal of heavy metal from industrial wastewater using modified activated coconut shell carbon. *Biochem. Eng. J*. 2007. **36**: 174.
47. Belver C., Bedia J. Adsorption on Carbon-Based Materials. *C.* 2024. **10**: 102.
48. Gonçalves G. Nanocarbon-Based Composites and Their Thermal Electrical and Mechanical Properties. *C.* 2025. **11**: 21.
49. Nejadshafieea V., Islami M. R. Adsorption capacity of heavy metal ions using sultone-modified magnetic activated carbon as a bio-adsorbent. *Mat. Sci. Eng. C.* 2019. **101**: 42.
50. Chi K. A., Donghee P., Seung H. W., Jong M. P. Removal of cationic heavy metal from aqueous solution by activated carbon impregnated with anionic surfactants. *J. Hazard. Mater*. 2009. **164**: 1130.
51. Kırbıyıka Ç., Pütünb A. E., Pütün E. Equilibrium kinetic and thermodynamic studies of the adsorption of Fe(III) metal ions and 2 4-dichlorophenoxyacetic acid onto biomass-based activated carbon by $ZnCl_2$ activation. *Surf. Interface.* 2017. **8**: 182.
52. Shin K.-Y., Hong J.-Y., Jang J. Heavy metal ion adsorption behavior in nitrogen-doped magnetic carbon nanoparticles: Isotherms and kinetic study. *J. Hazard. Mat.* 2011. **190**: 36.
53. Xu Q., Du J., Su X., Li X., Si Y., Fu Y. Highly porous carbon with rich inherent groups for ultrahigh adsorption of organic dyes from wastewater. *Colloids Surf. A: Physicochem. Eng. Aspects.* 2024. **703**: 135288.
54. Veselá P., Slovák V. N-doped carbon xerogels prepared by ammonia assisted pyrolysis: Surface characterisation thermal properties and adsorption ability for heavy metal ions. *J. Analyt. Appl. Pyrolys.* 2014. **109**: 266.
55. Fang C., Liu H., Yin Z., Zhu Z., Shi Y., Meng W., Zhu H., Li M. Surface curvature-driven adsorption-reduction mechanism over hollow N-doped carbon enhances recovery of precious metal ions from wastewater. *Envir. Res.* 2025. **269**: 120914.
56. Khue T. D., Ngoc P. K., Viet D. T., Thanh T. D., Nguyen T. H., Vinh P. V., Nguyen D. L., Thang P. D., Duong A. T., Das R., Nguyen H. T. Efficient adsorption of organic dyes using Fe_3O_4/carbon sphere nanocomposites: Synthesis and performance evaluation. *J. Sci.: Adv. Mat. Devic.* 2025. **10**: 100880.

57. Choi M., Jang J. Heavy metal ion adsorption onto polypyrrole-impregnated porous carbon. *J. Colloid Interface Sci.* 2008. **325**: 287.
58. Pustahija L., Bandl C., Alem S. A. A., Kern W. Surface Functionalization of Activated Carbon: Coupling of 3-(Aminopropyl) trimethoxysilane and (3-Glycidyloxypropyl) trimethoxysilane. *C.* 2024. **10**: 104.
59. Saleem J., Moghal Z.K.B., Tahir F., Al-Ansari T., McKay G. Environmental Impacts and Adsorption Isotherms of Coconut Shell Activated Carbon: Effect of Acid Activation Water and Fuel. *C.* 2025. **11**: 22.
60. Oliveira S. d. C., Dutra R. C., León J. J. L., Martins G. A. V., Silva A. M. A., Azevedo D. C .S. d., Santiago R. G., Ballesteros-Plata D., Rodríguez-Castellón E., Prauchner M. J. Activated Carbon Ammonization: Effects of the Chemical Composition of the Starting Material and the Treatment Temperature. *C.* 2025. **11**: 15.
61. Jiang W., Qi X., Huang P., Zhang S. Highly efficient arsenate adsorption removal from wastewater based on activated carbon-iron based metal organic framework in situ grown composites. *Mat. Sci. Eng. B.* 2025. **313**: 117927.
62. Li X., Zhu H., Wei X., Yang Q., Xiong C., Shi Z. Nanocellulose/activated carbon composite aerogel beads with high adsorption capacity for toxins in blood. *Int. J. Biolog. Macromol.* 2025. **300**: 140279.
63. Dehghani M. H., Karri R. R., Mubarak N. M. (Eds.) *Water Treatment Using Engineered Carbon Nanotubes* (Elsevier, 2024).
64. Wei Y., Yang R., Chen X., Wang L., Liu J.-H., Huang X.-J. A cation trap for anodic stripping voltammetry: NH_3–plasma treated carbon nanotubes for adsorption and detection of metal ions. *Analytica Chimica Acta.* 2012. **755**: 54.
65. Abdulkareem A. S., Hamzat W. A., Tijani J. O., Egbosiuba T. C., Mustapha S., Abubakre O. K., Okafor B. O., Babayemi A. K. Isotherm kinetics thermodynamics and mechanism of metal ions adsorption from electroplating wastewater using treated and functionalized carbon nanotubes. *J. Env. Chem. Eng.* 2023. **11**: 109180.
66. Yue Z., Guo X. Applications of coal-based carbon materials in adsorption. *Journal of Molecular Structure* 2025. **1337**: 142210.
67. Gun'ko V. M., Turov V. V. *Nuclear Magnetic Resonance Studies of Interfacial Phenomena* (CRC Press: Boca Raton, FL USA, 2013).
68. Chaplin M. *Water Structure and Science* Available online: http://www1.lsbu.ac.uk/water/ (accessed on 20 April, 2025).
69. Gun'ko V. M., Turov V. V. Interfacial phenomena in nanostructured systems with various materials. *ChemPhysChem* 2024. **25**: e202300622.
70. Gun'ko V. M., Turov V. V. Colligative properties of various liquid blends vs. temperature under confined space effects in pores of different adsorbents. *Chem. Phys. Tech. Surf.* 2024. **15**: 3.
71. Ngu L. H. *Carbon Capture Technologies* (Elsevier: Amsterdam, 2022).
72. Chung D. D. L. *Carbon Materials. Science and Applications. Engineering Materials for Technological Needs* (Vol. 3 World Scientific, 2019).
73. Inagaki M. Itoi H. Kang F. *Porous Carbons Syntheses and Applications* (Elsevier, 2021).
74. Biswas K., Mohanta Y.K., Mohanta T.K., Saravanan M. (Eds.) *Carbon-based Nanomaterials in Biosystems. Biophysical Interface at Lower Dimensions. Progress in Biochemistry and Biotechnology* (Elsevier, 2024).
75. Dave S., Das J., Sillanpää M. (Eds.) *Bio-Waste-Derived Carbon Materials and Their Applications Especially as Sensors* (Elsevier, 2025).
76. Yang R.T. *Adsorbents: Fundamentals and Applications* (Wiley: New York, 2003).
77. Moreno–Piraján J. C., Giraldo–Gutierrez L., Gómez–Granados F. *Porous Materials. Theory and Its Application for Environmental Remediation* (Springer Nature: Cham, 2021).

78. Ahmad A., Kumar R., Jawaid M. (Eds.) *Emerging Techniques for Treatment of Toxic Metals from Wastewater* (Elsevier: Amsterdam 2022).
79. Tagayev I. A., Muratova M. N., Andriyko L. S., Boykhonova M. Characteristics of new perspective bentonite coal sorbents modified by different compounds. *Sci. Innov.* 2021. **17**(3): 87.
80. Andriyko L., Tagayev I., Siora I., Petrik I., Goncharuk O. Novel granular bentonite-carbon sorbents: textural characterization adsorption-desorption isotherm kinetics and cost estimation. *Environ. Sci. Pollut. Res*. 2024. **31**: 42230.
81. Wandelt K., Bussetti G. (Eds.) *Encyclopedia of Solid-Liquid Interfaces.* Elsevier, 2023.
82. Tomaszewski W., Gun'ko V.M. Evaluation of adsorption and desorption steps in solid–phase extraction of explosives using carbon/silica gel nanocomposites. *J. Separ. Sci*. 2015. **38**: 2488.
83. Tomaszewski W., Gun'ko V. M., Leboda R., Skubiszewska-Zięba J. Structural characteristics of modified activated carbons and adsorption of explosives. *J. Colloid Interface Sci.* 2003. **266**: 388.
84. Tomaszewski W., Gun'ko V. M., Leboda R., Skubiszewska-Zięba J. Interaction of amphetamine and its N-alkyl-substituted derivatives with micro- and mesoporous adsorbents in polar liquids. *J. Colloid Interface Sci*. 2005. **282**: 261.
85. Tomaszewski W., Gun'ko V. M., Leboda R., Skubiszewska-Zięba J. Interaction of methoxy- and methylenedioxyamphetamines with carbon and polymeric adsorbents in polar liquids. *Cent. Eur. J. Chem.* 2010. **8**: 750.
86. Tomaszewski W., Gun'ko V. M. Evaluation of adsorption and desorption steps in the solid-phase extraction of explosives using carbon/silica gel nanocomposites. *J. Separation Sci*. 2015. **38**: 2488.
87. Tomaszewski W., Gun'ko V. M., Skubiszewska-Zięba J. Solid phase extraction of explosive nitramines on macroreticular polymers modified by freezing with water or acetone. *J. Separation Sci.* 2016. **39**: 1524.
88. Gun'ko V.M. Features of the morphology and texture of silica and carbon sorbents. Surface 2021. **13**(28): 127.
89. Gun'ko V. M., Turov V. V., Schur D. V., Zarko V. I., Prykhod'ko G. P., Krupska T. V., Golovan A. P., Skubiszewska–Zięba J., Charmas B., Kartel M. T. Unusual interfacial phenomena at a surface of fullerite and carbon nanotubes. *Chem. Phys.* 2015. **459**: 172.
90. Tóth A., Voitko K. V., Bakalinska O. N., Prykhod'ko G. P., Bertóti I., Martínez–Alonso A., Tascón J. M. D. Gun'ko V. M., László K. Morphology and adsorption activity of chemically modified MWCNT probed by nitrogen n–propane and water vapor. *Carbon* 2012. **50**: 577.
91. Gun'ko V. M., Sementsov Yu. I., Andriyko L. S., Nychyporuk Yu. M., Oranska O. I., Matkovsky O. K., Grebel'na Yu. V., Charmas B., Skubiszewska–Zięba J., Kartel M. T. 2D–nanostructured carbons: effects of oxidation and packing disordering. *Chemistry Physics and Technology of Surface* 2023. **14**(3): 275.
92. Voitko K. V., Whitby R. L. D., Gun'ko V. M., Bakalinska O. M., Kartel M. T., Laszlo K., Cundy A. B., Mikhalovsky S. V. Morphological and chemical features of nano and macroscale carbons affecting hydrogen peroxide decomposition in aqueous media. *J. Colloid Interface Sci.* 2011. **361**(1): 129.
93. Whitby R. L. D., Gun'ko V. M., Korobeinyk A., Busquets R., Cundy A. B., László K., Skubiszewska–Zięba J., Leboda R., Tombácz E., Toth I. Y., Kovacs K., Mikhalovsky S. V. Driving forces of conformational changes in single–layer graphene oxide. *ACS Nano* 2012. **6**(5): 3967.
94. Whitby R. L. D., A. Korobeinyk, Gun'ko V. M., R. Busquets, A. B. Cundy, K. Laszlo Skubiszewska–Zięba J., Leboda R., E. Tombacz I. Toth K. Kovacs Mikhalovsky S.V., pH

driven–physicochemical conformational changes of single–layer graphene oxide. *Chemical Communications* 2011. **47**: 9645.
95. Whitby R. L. D., Korobeinyk A. V., Gun'ko V. M., Wright D. B., Dichello G., Smith L. C., Fukuda T., Maekawa T., Mikhalovsky S. V., Thorpe J. R. Single–Layer Graphenes Functionalized with Polyurea: Architectural Control and Biomolecule Reactivity. *J. Phys. Chem. C.* 2013. **117**(22): 11829.
96. Gun'ko V. M., Turov V. V., Whitby R. L. D., Prykhod'ko G. P., Turov A. V., Mikhalovsky S. V. Interactions of single and multi–layer graphene oxides with water methane organic solvents and HCl studied by ^{1}H NMR. *Carbon* 2013. **57**: 191.
97. Gun'ko V. M., Turov V. V., Zarko V. I., Goncharuk O. V. Matkovsky A. K., Prykhod'ko G. P., Nychiporuk Yu. M., Pakhlov E. M., Krupska T. V., Balakin D. Yu., Charmas B., Andriyko L. S., Skubiszewska–Zięba J., Marynin A. I., Ukrainets A. I., Kartel M. T. Multi–layer graphene oxide alone and in a composite with nanosilica: preparation and interactions with polar and nonpolar adsorbates. *Applied Surface Science* 2016. **387**: 736.
98. Platzer B., Maurer G. Application of a generalized Bender equation of state to the description of vapour-liquid in binary systems. *Fluid Phase Equilib.* 1993. **84**: 79.
99. Provencher S. W. A constrained regularization method for inverting data represented by linear algebraic or integral equations. *Comp. Phys. Comm.* 1982. **27**: 213.
100. Ravikovitch P. I., Neimark A. V. Density functional theory model of adsorption on amorphous and microporous silica materials. *Langmuir* 2006. **22**: 11171.
101. Neimark A. V., Lin Y., Ravikovitch P. I., Thommes M. Quenched solid density functional theory and pore size analysis of micro-mesoporous carbons. *Carbon.* 2009. **47**: 1617.
102. Do D.D., Nguyen C., Do H. D. Characterization of micro–mesoporous carbon media. *Colloids Surf. A: Physicochem. Eng. Aspects.* 2001. **187–188**: 51.
103. Nguyen C., Do D. D. A new method for the characterization of porous materials. *Langmuir*. 1999. **15**(10) 3608.
104. Nguyen C., Do D. D. Effects of probing vapors and temperature on the characterization of micro–mesopore size distribution of carbonaceous materials. *Langmuir.* 2000. **16**(18): 7218.
105. Gun'ko V. M., Do D. D. Characterization of pore structure of carbon sorbents using regularization procedure. *Colloids Surf. A: Physicochem. Eng. Aspects.* 2001. **193**(1–3): 71.
106. Gor G. Y., Thommes M., Cychosz K. A., Neimark A. V. Quenched solid density functional theory method for characterization of mesoporous carbons by nitrogen adsorption. *Carbon*. 2012. **50**(4): 1583.
107. Pujari P.K., Sen D., Amarendra G., Abhaya S., Pandey A. K., Dutta D., Mazubder S. Study of pore structure in grafted polymer membranes using slow positron beam and small–angle X–ray scattering techniques. Nuclear. *Instr. Method Phys. Res. B.* 2007. **254**: 278.
108. Sakurai S. *SAXS evaluation of size distribution for nanoparticles* (Chapter 5 In A.E. Ares (ed.) X–ray Scattering InTech Croatia, 2017).
109. H. Brumberger (Ed.) *Small Angle X–ray Scattering* (Gordon & Breach: New York Syracuse, 1965).
110. Gun'ko V. M. Morphological and textural features of various materials composed of porous or nonporous nanoparticles differently packed in secondary structures. *Appl. Surf. Sci*. 2021. **569**: 151117.
111. Ph. Dieudonné A.A. Hafidi P. Delord J. Phalippou Transformation of nanostructure of silica gels during drying. *J. Non–Crystal. Solid*. 2000. **262**: 155.
112. Fairén–Jiménez D., Carrasco–Marín F., Djurado D., Bley F., Ehrburger–Dolle F., Moreno–Castilla C. Surface area and microporosity of carbon aerogels from gas adsorption and small– and wide–angle X–ray scattering measurements. *J. Phys. Chem. B*. 2006. **110**: 8681.

113. Strange J. H., Rahman M., Smith E. G. Characterization of porous solids by NMR. *Phys. Rev. Lett.* 1993. **71**: 3589.
114. Mitchell J., Webber J. B. W., Strange J. H. Nuclear magnetic resonance cryoporometry. *Phys. Rep.* 2008. **461**: 1.
115. Kimmich R. *NMR Tomography Diffusometry Relaxometry* Springer: Heidelberg, 1997.
116. Franke J. P., de Zeeuw R. A. Solid-phase extraction procedures in systematic toxicological analysis. *J. Chromatogr. B.* 1998. **713**: 51.
117. De Martinis B. S., Barnes A. J., Scheidweiler K. B., Huestis M. A. Development and validation of a disk solid phase extraction and gas chromatography-mass spectrometry method for MDMA MDA HMMA HMA MDEA methamphetamine and amphetamine in sweat. *J. Chromatogr. B.* 2007. **852**: 450.
118. Namera A., Nakamoto A., Nishida M., Saito T., Kishiyama I., Miyazaki S., Yahata M., Yashiki M., Nagao M. *J. Chromatogr. A.* 2008. **1208**(12): 71.
119. Brettell T. A., Butler J. M., Almirall J. R. Forensic science. *Anal. Chem*. 2009. **81**: 4695.
120. Ahmad S. M., Gonçalves O. C., Oliveira M. N., Neng N. R., Nogueira J. M. F. Application of microextraction-based techniques for screening-controlled drugs in forensic context - A review. *Molecules.* 2021. **26**(8): 2168.
121. Frisch M. J., Trucks G. W., Schlegel H. B., Scuseria G. E., Robb M. A., Cheeseman J. R., Scalmani G., Barone V., Petersson G. A., Nakatsuji H., Li X., Caricato M., Marenich A. V., Bloino J., Janesko B. G., Gomperts R., Mennucci B., Hratchian H. P., Ortiz J. V., Izmaylov A. F., Sonnenberg J. L., Williams–Young D., Ding F., Lipparini F., Egidi F., Goings J., Peng B., Petrone A., Henderson T., Ranasinghe D., Zakrzewski V. G., Gao J., Rega N., Zheng G., Liang W., Hada M., Ehara M., Toyota K., Fukuda R., Hasegawa J., Ishida M., Nakajima T., Honda Y., Kitao O., Nakai H., Vreven T., Throssell K., Montgomery J. A. Jr., Peralta J. E., Ogliaro F., Bearpark M. J., Heyd J. J., Brothers E. N., Kudin K. N., Staroverov V. N., Keith T. A., Kobayashi R., Normand J., Raghavachari K., Rendell A. P., Burant J. C., Iyengar S. S., Tomasi J., Cossi M., Millam J. M., Klene M., Adamo C., Cammi R., Ochterski J. W., Martin R. L., Morokuma K., Farkas O., Foresman J. B., Fox D. J. Gaussian 16 Revision C.02. Gaussian Inc., Wallingford CT, 2019.
122. Barca G. M. J., Bertoni C., Carrington L., Datta D., De Silva N., Deustua J. E., Fedorov D. G., Gour J. R., Gunina A. O., Guidez E., Harville T., Irle S., Ivanic J., Kowalski K., Leang S. S., Li H., Li W., Lutz J. J., Magoulas I., Mato J., Mironov V., Nakata H., Pham B. Q., Piecuch P., Poole D., Pruitt S. R., Rendell A. P., Roskop L. B., Ruedenberg K. Recent developments in the general atomic and molecular electronic structure system. *J. Chem. Phys*. 2020. **152**: 154102.
123. Rüger R., Franchini M., Trnka T., Yakovlev A., van Lenthe E., Philipsen P., van Vuren T., Klumpers B., Soini T. AMS 2025.1 SCM Theoretical Chemistry Vrije Universiteit Amsterdam The Netherlands http://www.scm.com.
124. Marenich A. V., Cramer C. J., Truhlar D. G. Universal solvation model based on solute electron density and on a continuum model of the solvent defined by the bulk dielectric constant and atomic surface tensions. *J. Phys. Chem. B.* 2009. **113**: 6378.
125. Gun'ko V. M. Interfacial phenomena: effects of confined space and structure of sorbents on the behavior of polar and nonpolar adsorbates at low temperatures. *Current Physical Chemistry*. 2015. **5**: 137.
126. Gun'ko V. M. Effects of methods and basis sets on calculation results using various solvation models. *Chemistry Physics and Technology of Surface*. 2018. **9**: 3.
127. Gun'ko V. M. Charge distribution functions for characterization of complex systems. *Chem. Phys. Technol. Surf*. 2021. **12**: 3.
128. Stewart J. J. P. MOPAC2023. Stewart Computational Chemistry. web: HTTP://OpenMOPAC.net. 2025. (accessed on 13.09.2025, Ver. 23.2).

129. Pettersen E. F., Goddard T. D., Huang C. C., Meng E. C., Couch G. S., Croll T. I., Morris J. H., Ferrin T. E. UCSF ChimeraX: Structure visualization for researchers educators and developers. *Protein Sci*. 2021. **30**: 70.
130. Avogadro 2. https://two.avogadro.cc/. Ver. 1.100. 2025.
131. Pedretti A., Mazzolari A., Gervasoni S., Fumagalli L., Vistoli G. The VEGA suite of programs: a versatile platform for cheminformatics and drug design projects. *Bioinformatics* 2021. **37**: 1174.
132. Jmol: an open–source Java viewer for chemical structures in 3D (Ver. 16.3.33). http://www.jmol.org/.
133. Gun'ko V. M. Features of BET method application to various adsorbents. *Chem. Phys. Tech. Surf*. 2022. **13**: 249.
134. Boehm H. P. Some aspects of the surface chemistry of carbon blacks and other carbons *Carbon*. 1994. **32**: 759.
135. Blitz J. P., Gun'ko V. (Eds.) *Surface Chemistry in Biomedical and Environmental Science* NATO Science Series II: Mathematics Physics and Chemistry Vol. 228 (Springer: Dordrecht, 2006).
136. Leboda R., Gun'ko V. M., Tomaszewski W., Trznadel B. J. Relationship between structural characteristics of activated carbons and their concentrating efficiency with respect to nitroorganics. *J. Colloid Interface Sci.* 2001. **238**: 489.
137. Leboda R., Turov V. V., Tomaszewski W., Gun'ko V. M., Skubiszewska–Zięba J. Effect of adsorption of nitro aromatic compounds on characteristics of bound water layers in aqueous suspensions of activated carbons. *Carbon.* 2002. **40**: 389.
138. Melillo M., Gun'ko V. M., Tennison S. R., Mikhalovska L. I., Phillips G. J., Davies J. G., Lloyd A. W., Kozynchenko O. P., Malik D. J., Streat M., Mikhalovsky S. V. Structural Characteristics of Activated Carbons and Ibuprofen Adsorption Affected by Bovine Serum Albumin. *Langmuir* 2004. **20**: 2837.
139. Ivanov A. E., Kozynchenko O. P., Mikhalovska L. I., Tennisson S. R., Jungvid H., Gun'ko V. M., Mikhalovsky S. V. Activated carbons and carbon–containing poly(vinyl alcohol) cryogels: characterization protein adsorption and possibility of myoglobin clearance. *Phys. Chem. Chem. Phys*. 2012. **14**: 16267.
140. Gun'ko V. M., Betz W. R., Patel S., Murphy M. C., Mikhalovsky S. V. Adsorption of lipopolysaccharide on carbon sieves. *Carbon* 2006. **44**(7): 1258.

PACS: 61.43.Gt; 68.03.-g; 68.43.-h; 81.40.Ef *DOI:10.15407/Surface.2025.17.169*

ЯВИЩА НА МЕЖАХ ПОДІЛУ ПІД ВПЛИВОМ МОРФОЛОГІЇ ТА ТЕХТУРИ ВУГЛЕЦЕВИХ МАТЕРІАЛІВ ТА ЇНІХ КОМПОЗИТІВ

В. М. Гунько[1,*], В. В. Туров[1], Л. С. Андрійко[1], І. А. Тагаєв[2]

[1]Інститут хімії поверхні ім. О. О. Чуйка Національної академії наук України, вул. Олега Мудрака, 17, Київ, 03164, Україна, e-пошта: vlad_gunko@ukr.net
[2]Навойський Іноваційний Університет, вул. Ташкентська, 39, Навої 210100, Узбекистан, e-пошта: andriykolyuda@gmail.com

Вуглецеві матеріали (ВМ) можуть характеризуватися різною морфологією твердих частинок, текстурою, структурою поверхні (наприклад, ступенем окислення/відновлення) та іншими характеристиками. Тому пошук закономірностей численних ВМ, що стосуються міжфазних явищ, включаючи сорбцію з різних фаз, може бути складним завданням. Для з'ясування сутнісних аспектів явищ можуть бути використані різні експериментальні (наприклад, електронна мікроскопія, сорбція, спектроскопія, рентгенівська дифракція, термогравіметрія тощо) та теоретичні (наприклад, квантова хімія) методи з використанням розроблених обчислювальних методів. Тут були проаналізовані десятки ВМ і композитів щодо (і) морфології твердих частинок, текстурних і поверхневих характеристик; (іі) сорбції органічних і неорганічних сполук, розчинених речовин/елюатів у різних середовищах; та (ііі) ефектів обмеженого простору та кріоскопічних ефект для окремих та змішаних розчинників залежно від температури (при $T < T_f$) та концентрацій. Отримані результати становлять інтерес як з теоретичної, так і з практичної точок зору, оскільки показують різні аспекти міжфазних явищ, що відбуваються в поровому просторі різних ВМ і композитів, що характеризуються різною морфологією, текстурою і структурою поверхні. Це важливо для оптимізації характеристик ВМ для ефективного використання їх у практичних застосуваннях.

Ключові слова: *3D-0D вуглецеві матеріали, активоване вугілля, графітизовані вуглеці, текстурні характеристики, сорбція, розчини, міжфазні явища, ефект обмеженого простору, кріоскопічний ефект.*